Stony Brook University

Structure Characterization of Cellulose Nanofibers/Microfibrils

A Dissertation Presented

by

Ying Su

to

The Graduate School

in Partial Fulfillment of the

Requirements

for the Degree of

Doctor of Philosophy

in

Chemistry

Stony Brook University

December 2014

Stony Brook University

The Graduate School

Ying Su

We, the dissertation committee for the above candidate for the

Doctor of Philosophy degree, hereby recommend

acceptance of this dissertation.

Benjamin S. Hsiao – Dissertation Advisor
Professor, Department of Chemistry

Benjamin Chu – Dissertation Advisor
SUNY Distinguished Professor, Department of Chemistry

David M. Hanson – Chairperson of Defense
SUNY Distinguished Service Professor, Department of Chemistry

Joseph W. Lauher – Third Member
SUNY Distinguished Teaching Professor, Department of Chemistry

Devinder Mahajan – Outside Member
Professor, Department of Materials Science & Engineering

This dissertation is accepted by the Graduate School

Charles Taber
Dean of the Graduate School

Abstract of the Dissertation

Structure Characterization of Cellulose Nanofibers/Microfibrils

by

Ying Su

Doctor of Philosophy

in

Chemistry

Stony Brook University

2014

Cellulose nascent crystals or cellulose microfibrils, extracted from biomass through TEMPO-mediated oxidation, are low cost, biocompatible and high performance materials that have found wide applications in various fields, including water purification, polymer nanocomposites, biosensors, and tissue engineering. However, several fundamental aspects of the structure characterization of these cellulose nascent crystals and microfibrils have still been ambiguous. The current study uses synchrotron small-angle X-ray scattering (SAXS) to characterize the structure of cellulose nanofibers (and their aggregates) and corresponding dispersed microfibrils from various sources (e.g. wood, bamboo, cotton, jute, etc.) in aqueous suspensions. It was revealed that typical cellulose nanofibers extracted from the dried wood pulp were of the ribbon shape with lengths in the 1 μm range and cross-section sizes from 3 nm × 8 nm to 9 nm × 20 nm, depending on the source. In contrast, microfibril fractions extracted from never-dried dilignified Spruce wood were in the form of “nanostrips” with widths and thicknesses of around 4 nm and 0.5 nm, respectively. The thickness determination indicated that

these nanostrips were comprised of only a monolayer of cellulose molecules. The molecular arrangement in these two-dimensional crystals was determined from wide-angle X-ray diffraction (WAXD). The structural results acquired from the X-ray scattering/diffraction techniques were consistent with other characterization results, including transmission electron microscopy (TEM), atomic force microscopy (AFM) and nuclear magnetic resonance (NMR).

Table of Contents

List of Figures

List of Tables

Acknowledgments

I would like to take this opportunity to express my deepest gratitude to my advisors Prof. Benjamin Chu and Prof. Benjamin S. Hsiao for their continuous support, intellectual guidance, invaluable advice and warm encouragement in the last four years. Thanks to them for providing me with an excellent atmosphere for doing research. I would also like to thank Prof. David M. Hanson and Prof. Joseph W. Lauher, who have been serving as the chair and the third member, respectively, in my research committee over the past four years, giving helpful comments and advice. Thanks to Prof. Devinder Mahajan for participating in my defense committee as the outside member.

I would like to thank Dr. Christian Burger for helping me develop my background in X-ray scattering and for providing numerous instructional suggestions on my research. Especially, thanks to him for his significant contributions on the development of SAXS models presented in this work.

I would like to thank Dr. Lin Yang, Dr. Mark Allaire, Dr. Vito Graziano and Dr. Maya Endoh at BNL for their assistance on the equipment setting up for my synchrotron X-ray scattering experiments. Thanks to Dr. Yan Li at BNL for her insightful suggestions on the cellulose project during our collaboration. Thanks to Dr. Tong Wang at BNL for his kind help in TEM analysis. In addition, I would like to thank Prof. Robert F. Schneider, Dr. Mohammad Akhtar, Dr. Bradford Tooker, Dr. Susan Oatis and Dr. Eric Patterson for their help and instructions when I worked as a Teaching Assistant.

I would like to thank all my lab mates and chemistry department graduate students for their research advice and discussions. Thanks to Dr. Hongyang Ma, Dr. Dufei Fang, Dr. Yimin

Mao, Dr. Hongwen Zhou, Dr. Yang Liu, Dr. Ran Wang, Dr. Tsung-Ming Yeh, Dr. Xiao Wang, Dr. Justin Che, Dr. Zhe Wang, Dr. Rui Yang, Dr. Yueming Xu, Dr. Bingfei Cao and Hao Zhou, Sihui Guan, Zhirui Mo, Hui Gao, Kai Liu, Jue Liu, Ye Tian, Weixuan Yu, Tianyuan Wu, Bingyin Jiang, Zhe Sun. My research would not have been possible without their help.

Thanks to my parents, my family and all my friends for all their love and support.

Finally, I would like to thank my husband, Rui Liang, for lots of his helpful comments on my research, and more importantly, for his constant company in my life through the good times and bad.

Publications

1. Su, Y.; Burger, C.; Hsiao, B. S.; Chu, B. Characterization of TEMPO-oxidized cellulose nanofibers in aqueous suspension by small-angle X-ray scattering. *Journal of Applied Crystallography* **2014**, 47: 788−798 (Chapter 2 of this dissertation)

2. Su, Y.; Burger, C.; Ma, H.; Saito, T.; Isogai, A.; Hsiao, B. S.; Chu, B. Cellulose nanostrips: exploring the nature of cellulose microfibrils (manuscript to be submitted) (Chapter 3 of this dissertation)

3. Su, Y.; Burger, C.; Ma, H.; Hsiao, B. S.; Chu, B. Structure characterization of cellulose nanofibers extracted from various biomass species (manuscript under preparation) (Chapter 2 of this dissertation)

4. Su, Y.; Burger, C.; Ma, H.; Hsiao, B. S.; Chu, B. Structure characterization of silver-ion decorated cellulose nanofibers (manuscript under preparation) (Chapter 4 of this dissertation)

5. Su, Y.; Burger, C.; Ma, H.; Hsiao, B. S.; Chu, B. Structure characterization of jute cellulose by X-ray scattering techniques (manuscript under preparation) (Chapter 2 and 5 of this dissertation)

Chapter 1 Introduction

1.1 Cellulose

1.1.1 Cellulose in Biomass

Cellulose is the most abundant organic molecule on earth[1]. Its crystalline entity is the most basic structural component of the cell wall in all green plants and some types of algae[2,3]. In addition to plants, cellulose is also found in biofilms, synthesized by some bacteria[2,3]. Chemically, a cellulose molecule is a glucan chain consisting of repeating β-1,4-linked anhydro-D-glucose units with each unit corkscrewed 180° relative to its neighbors[2,4]. Cellulose exists in several crystalline polymorphs, such as I_α, I_β, II, III_1, III_2, IV_1 and IV_2, with the difference being mainly the location of hydrogen bonds between and within cellulose chains[5]. However, the native cellulose crystalline structure is only found in two phases, i.e. I_α and I_β, with the I_α cellulose being normally seen in bacteria and algae and the I_β cellulose mainly in higher order plants. The lattice parameters of I_α and I_β cellulose determined from X-ray structure refinement[6,7] are shown in Table 1.1. The lattice parameters can fluctuate around these results for 0.2-2% depending on different experimental conditions[8,9].

Table 1.1 Lattice parameter of I_α and I_β cellulose[6,7,9]

	I_α	I_β
Cell Setting	Triclinic	Monoclinic
Space Group	P1	$P2_1$
a (Å)	6.717(7)	7.76(1)
b (Å)	5.962(6)	8.20(1)
c (Å)	10.400(6)	10.37(1)
α (°)	118.08(5)	90
β (°)	114.80(5)	90
γ (°)	80.37(5)	96.62(5)

Crystalline cellulose microfibrils, composed of orderly arranged glucan chains (Figure 1.1), function as the principle building blocks for the cell wall in the hierarchical structure of

plants[10]. As shown in Figure 1.1, cellulose molecular chains firstly assemble into microfibrils (nascent crystals) in an ordered fashion, and multiple microfibrils would form aggregates of larger dimensions, which are termed cellulose nanofibers in this study. The nanofibers further bundle together and form even larger fibers and to support the structure of cell wall. In this study, it was found that cellulose microfibrils can be delaminated into thin layers composed of monomolecular chains, and these layers are called "nanostrips" in this study.

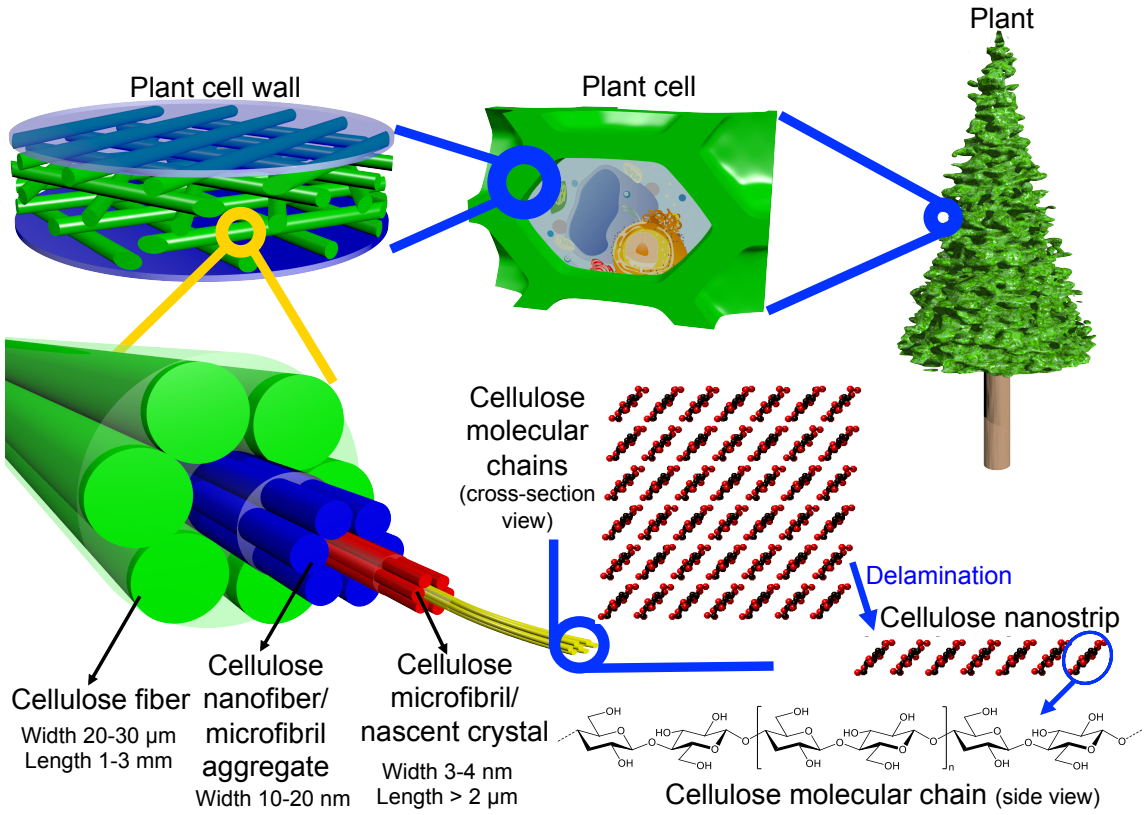

Figure 1.1 Hierarchical structures of green plants. Figure courtesy of Dr. Christian Burger.

In the cell wall, cellulose microfibrils are embedded in a matrix of polysaccharides incldluing hemicelluloses and pectins[11]. While the lengths of microbrifils usually reach a few microns, the diameters of the cross-sections only vary from 2 to 20 nm, depending on their biological origins[12,13]. It has been revealed that cellulose microfibrils are synthesized and extruded from the synthase complexes in the plasma membrane in the cell wall[11,14], and

microfibrils are tethered together through hemicellulose molecules (e.g. xylan, xyloglucan, etc.) that both bind to the surface of microfibrils and penetrate into the crystalline structure of microfibrils[11,15]. The spaces between the microfibrils are filled up by lignin, which is covalently linked to hemicellulose[16,17], and the weight percentage of lignin in wood cell walls can reach 40%. The binding and tethering between the polysaccharides and lignin integrate the cell wall as a whole and reinforce the mechanical strength of the plant[11].

Regarding the specific biosynthesis and assembly mechanism of cellulose microfibrils, there are diverse speculative models proposed. Among these models, the multi-step model (Figure 1.2[18]), based on molecular mechanical calculation carried out by Brown et al., is the most commonly accepted one, although it has not been experimentally demonstrated so far. In the multi-step model, the nascent cellulose molecular chains produced by the cellulose synthases first associate with each other and form a monolayer by van der Waals forces in the terminal complex (TC). Subsequently, those monolayers are extruded from the rosette aperture and assemble via hydrogen bonding to form the crystalline cellulose microfibril[14,18].

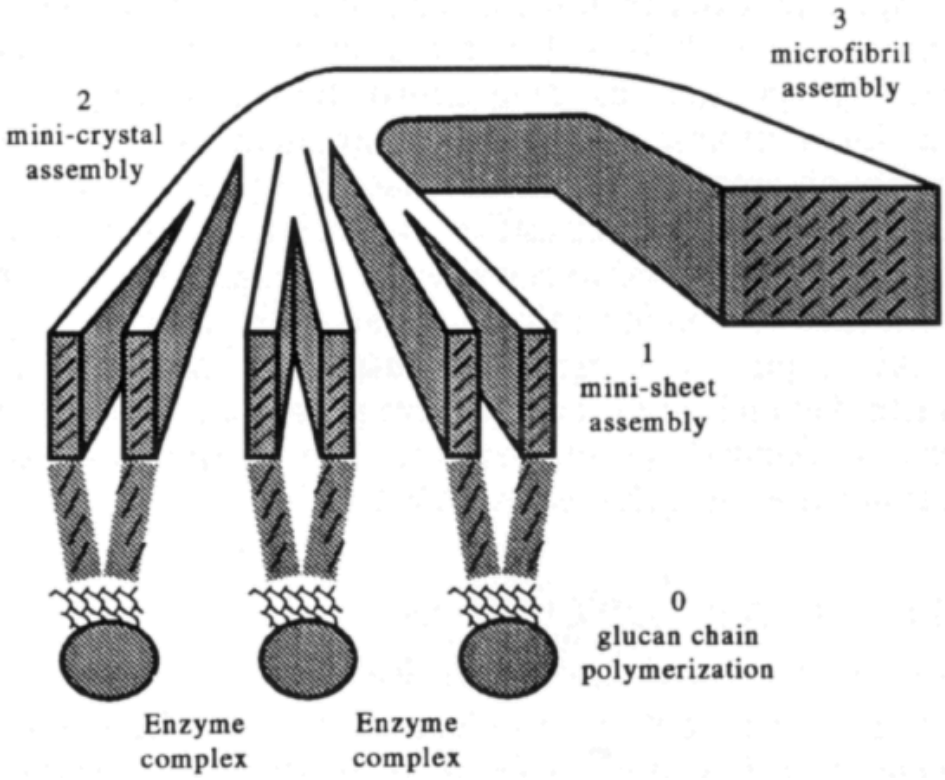

Figure 1.2 A proposed model for the stages of microfibril formation: (0) glucose monomers are polymerized enzymatically from catalytic sites in the enzyme complex subunits to form glucan chains; (1) the glucan chains associate via van der Waals forces to form mini-sheets; (2) mini-sheets associate via hydrogen bond to form mini-crystals; (3) several mini-crystals then associate to form a crystalline microfibril.[18]

1.1.2 Isolation of Cellulose Microfibrils/Nanofibers from Biomass

In recent years, cellulose crystalline microfibrils or nanofibers (small bundles of microfibrils) isolated from the biomass of plants or some marine animals (like tunicate) have attracted close attention because of their biodegradability, high aspect ratio and large specific surface area[19], excellent mechanical properties[20,21] and outstanding chemical and thermal stabilities[22,23]. The application of cellulose nanofibers and their derivatives includes but not limited to the following: reinforcing phase in nanocomposites[22,24], scaffold for biological cell constructions[25], diffusion-limiting membranes in biosensors[26], hemodialysis membranes[27], and water filtration membranes[23].

Various methods, including mechanical treatments (e.g. homogenization by Waring blender[28,29], high-pressure homogenization[30,31], grinding and milling[32,33], etc.), chemical treatments (e.g. H_2SO_4 hydrolysis[34-37] and HCl hydrolysis[38,39]) and chemical together with successive mechanical treatments (e.g. acid hydrolysis followed by mechanical disintegration[40-42] and TEMPO-mediated oxidation followed by homogenization[12,43,44]), have been reported to extract cellulose nanofibers from plant biomass.

Depending on the raw materials and fibrillation method adopted, the degree of polymerization, morphology and surface properties of the product nanofibers can be very different[45]. For example, individual cellulose microfibrils extracted from never-dried soft wood pulp through 2,2,6,6-tetrame-thylpiperidine-1-oxyl (TEMPO)-mediated oxidation method exhibit a regular width of 3-4 nm[46], while cellulose nanofibers extracted from dried soft wood pulp with the same technique are microfibrillar bundles with an average width of 12 nm[10]. The reason is believed to be that the drying process irreversibly eliminated the accessibility and reactivity of cellulose microfibrils[12]. With respect to the effects of different treatments on the properties of cellulose nanofibers, it has been found that nanofibers obtained through pure mechanical treatment tend to aggregate due to the lack of surface charges to separate them, and nanofibers generated using acid hydrolysis followed by mechanical fibrillation usually have short fiber lengths (50−200 nm). In contrast, the TEMPO-mediated oxidation is able to regioselectively convert the hydroxyl groups at C6 positions into carboxylic groups (Figure 1.3), which introduces a higher density of negative charges onto the fibril surfaces. This method will not only significantly improve the dispersibility of oxidized nanofibers in water[47,48], but also provide potential sites for further grafting of other groups onto cellulose surfaces.

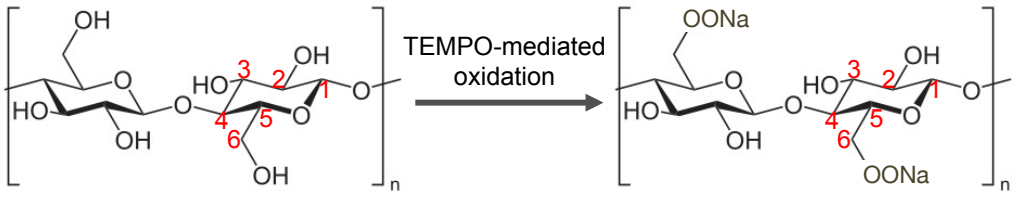

Figure 1.3 Diagram of the cellulose structural formulae before and after the TEMPO-mediated oxidation.

1.1.3 Structure Characterization of Cellulose Microfibrils

The fine structure of cellulose microfibrils has been investigated by various characterization methods. For microfibrils extracted from algae[49,50] and tunicate[51] with relatively large cross-sectional dimensions and high degrees of crystallinity, the microfibril cross-section dimensions could be directly observed and measured on negatively stained microfibrils using TEM. The crystalline information of microfibrils could also be obtained by taking the lattice images of the fiber cross-section as well as by analyzing electron diffraction patterns from a single microfibril[49-51]. However, cellulose microfibrils from higher plants have much smaller cross-sectional sizes and many microfibrils tend to bind together among themselves. Thus, it becomes more difficult to reveal the morphology of such microfibrils when compared with those highly crystalline cellulose microfibrils[13].

The isolation of cellulose microfibrils from biomass offers significant opportunity to take a closer look at the morphology of microfibrils. SEM/TEM images and the Scherer dimensions calculated from X-ray diffraction of cellulose microfibrils from different plants in previous reports determined the approximate width of 2–4 nm for herbaceous plant and wood cellulose[52], 3–11 nm for ramie cellulose[53], and 5–7 nm for flax and cotton linter cellulose[54-56]. With the assistance of AFM, the fractions of cellulose microfibrils with thickness below 1 nm were observed by Renneckar et al., and it was suggested that the thin fractions were single layers of cellulose molecular chains as a result of the delamination of cellulose microfibrils[57].

Small-angle X-ray scattering (SAXS) is a powerful technique to study the nanostructures of both ordered and disordered systems and to provide a direct way to investigate the shape and size of cellulose microfibrils/nanofibers. SAXS of slices of Norway spruce wood stem without any chemical or physical treatment indicated a circular cross section with diameter of 2.5 nm for the microfibril[17] and is consistent with the result in another report using the same materials and similar experimental method[54]. For cellulose nanofibers obtained through TEMPO-mediated oxidation, the nanofibers, individually and randomly dispersed in aqueous suspension as a result of the repulsive anionic charges on the surfaces, offer an idea scenario to study the morphology of nanofibers without considering the inter-fiber interferences by SAXS. In this work, the analysis of SAXS patterns of cellulose nanofibers in suspension will be particularly addressed and discussed.

1.2 Principles of X-ray Scattering/Diffraction Techniques

1.2.1 SAXS and WAXD

X-ray is an electromagnetic radiation with wavelength ranging from 0.01 to 10 nm, which is of similar length scale as the crystal lattice constants or the distance between molecules in nanometer scales. In practice, however, the adsorption of "soft" X-rays with wavelength larger than 1 nm is too strong and, usually, only "hard" X-rays is used for structural analysis.

When the X-ray beam of a given wavelength impinges on the electrons in an atom, the X-rays would be scattered (Figure 1.3) with the phase difference of the scattered X-rays being determined by the electron density distribution in the object. Therefore, the scattered X-ray intensity collected by a detector should contain the structural information of the object. Mathematically, the scattered X-ray intensity distribution in reciprocal space is the Fourier transform of the electron density distribution of the system in real space.

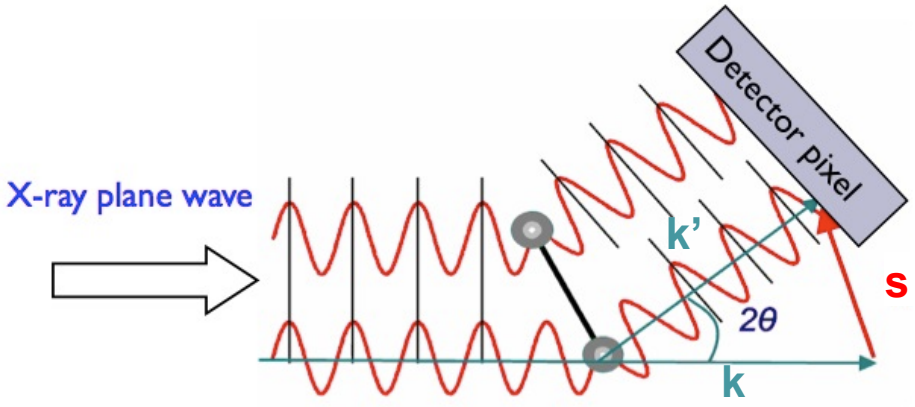

Figure 1.4 Diagram of X-ray scattering mechanism.[58]

As shown in Figure 1.4, assuming **k** and **k'** are the wave vectors of the incident and the scattered wave, respectively, the scattering vector is **s** with $s = |\mathbf{s}| = \frac{2\sin\theta}{\lambda}$, where 2θ is the scattering angle and λ is the wavelength of the X-ray beam. For a crystalline lattice, if the angle between the incident beam and a specific lattice plane is θ, according to Bragg's law $2d\sin\theta = n\lambda$, the inter-plane distance d is actually $\frac{1}{s}$.

Depending on the scales of the real space structures that one is interested, X-ray scattering is usually divided into two categories: small-angle X-ray scattering (SAXS) and wide-angle X-ray diffraction (WAXD). Although the working mechanisms of SAXS and WAXD are identical, SAXS provides information of "larger" structures with $d >> 10\lambda$, such as the shape and size of macromolecules and particles in nanometer scales, no matter whether they are crystalline or non-crystalline, while WAXD decodes "smaller" structures with $d << 10\lambda$, such as the crystal lattice parameters in atomic scale. Experimentally, SAXS requires a long sample-to-detector distance (e.g. couple of meters) and WAXD requires a short sample-to-detector distance (e.g. several centimeters to dozens of centimeters).

In recent decades, SAXS in solution or suspension has attracted more interests because it can be used to obtain low-resolution structural information, including shape, size, and size distribution, of macromolecules in solution and nanoparticles in suspension. To better study the morphology of individual macromolecules or particles, the concentration of the system of interest in either solution or suspension should be low enough to avoid inter-particle interference that will complicate the analysis. The development of synchrotron X-rays has made the solution SAXS technology much more useful and well suited to our experiments.

1.2.2 Data Analysis of X-ray Scattering/Diffraction

For typical 1D X-ray diffraction (XRD) pattern generated from a powder diffractometer, the routine method to solve the crystalline structure of the sample is to perform the line profile analysis (LPA) to analyze the shape of the peaks that are characteristic of the state of the material[59]. Simply put, since the peak broadening can be the integral effect of the instrumental broadening, the size broadening and the strain/disorder broadening, the purpose of the LPA is to separate the three broadenings and to solve the crystal size and the extent of distortion from the size broadening and the strain/disorder broadening, respectively. In practice, there are many approaches that can be used to perform the LPA. Generally, the integral breadth method[60] and the peak fitting method (e.g. Rietveld refinement)[61] are frequently used.

For 2D WAXS patterns collected by using a CCD area detector, one can convert the 2D image into 1D profile for a powder sample and perform the LPA as described above. When the sample has preferred orientations or is of fiber symmetry, the simulation of the 2D diffraction pattern using the orientation distribution function (ODF) is sometimes necessary and useful to quantitatively determine the degree of preferred orientation of the ensemble[62].

For the SAXS pattern, the scattered intensity is the product of the form factor, which comes from the shape and size information of the macromolecules or particles, and the interference function representing the inter-particle or inter-macromolecule relationship.

In dilute solution or completely disordered system, the interference function tends to be one and the intensity is entirely determined by the form factor. In this case, if the particles or macromolecules are monodisperse, the radius of gyration can be calculated simply by using the Guinier approximation[63]. For detailed information (e.g. shape and exact dimensions), the calculated intensities from models of different shapes and dimensions can be compared with the experimental data to determine which model will be able to provide a better fit. Or if the system is polydisperse and the shape of the particle is known, different kinds of size distributions can be adopted to fit the experimental data. On the other hand, if the particles in solution or suspension are totally or partially ordered, which usually happens in semi-dilute or concentrated solution/suspension, the structure factor (i.e. inter-particle interference) has to be taken into account during analysis. Since the structure factor is related to the probability distribution function of inter-particle distances, the pair correlation function of the system in real space is needed to solve the structure factor[64-66]. In this case, there are many structure factor models available, such as the hard-sphere potential, cylinders, solution of flexible polymers, and solution of semi-flexible polymers[64-66]. However, it should be noted that, for the SAXS simulation, a model that fits the experimental data very well might not be the unique solution, especially for polydisperse systems with no obvious minimum on the pattern. Then, more structural information about the material obtained from other characterization methods (e.g. electron microscope) is necessary to assist the SAXS analysis.

References

(1) Campbell, N. A. *Biology*; 4th ed.; Benjamin Cummings: NY, 1996.

(2) Habibi, Y.; Lucia, L. A.; Rojas, O. J. *Chem Rev* **2010**, *110*, 3479.

(3) Klemm, D.; Heublein, B.; Fink, H. P.; Bohn, A. *Angew Chem Int Edit* **2005**, *44*, 3358.

(4) Sjostrom, E. *Wood chemistry, fundamentals and applications*; 2nd ed.; Academic Press: San Diego, 1993.

(5) Zugenmaier, P. *Prog Polym Sci* **2001**, *26*, 1341.

(6) Nishiyama, Y.; Sugiyama, J.; Chanzy, H.; Langan, P. *J Am Chem Soc* **2003**, *125*, 14300.

(7) Nishiyama, Y.; Langan, P.; Chanzy, H. *J Am Chem Soc* **2002**, *124*, 9074.

(8) Bucko, T.; Tunega, D.; Angyan, J. G.; Hafner, J. *J Phys Chem A* **2011**, *115*, 10097.

(9) Nishiyama, Y.; Johnson, G. P.; French, A. D.; Forsyth, V. T.; Langan, P. *Biomacromolecules* **2008**, *9*, 3133.

(10) Su, Y.; Burger, C.; Hsiao, B. S.; Chu, B. *J Appl Crystallogr* **2014**, *47*, 788.

(11) Cosgrove, D. J. *Nature reviews. Molecular cell biology* **2005**, *6*, 850.

(12) Saito, T.; Nishiyama, Y.; Putaux, J. L.; Vignon, M.; Isogai, A. *Biomacromolecules* **2006**, *7*, 1687.

(13) Nishiyama, Y. *J Wood Sci* **2009**, *55*, 241.

(14) Saxena, I. M.; Brown, R. M. *Ann Bot-London* **2005**, *96*, 9.

(15) Hayashi, T. *Annu Rev Plant Phys* **1989**, *40*, 139.

(16) Chabannes, M.; Ruel, K.; Yoshinaga, A.; Chabbert, B.; Jauneau, A.; Joseleau, J. P.; Boudet, A. M. *Plant J* **2001**, *28*, 271.

(17) Jakob, H. F.; Fratzl, P.; Tschegg, S. E. *J Struct Biol* **1994**, *113*, 13.

(18) Cousins, S. K.; Brown, R. M. *Polymer* **1995**, *36*, 3885.

(19) Terech, P.; Chazeau, L.; Cavaille, J. Y. *Macromolecules* **1999**, *32*, 1872.

(20) Khan, R. A.; Salmieri, S.; Dussault, D.; Uribe-Calderon, J.; Kamal, M. R.; Safrany, A.; Lacroix, M. *J Agr Food Chem* **2010**, *58*, 7878.

(21) Azeredo, H. M. C.; Mattoso, L. H. C.; Avena-Bustillos, R. J.; Ceotto, G.; Munford, M. L.; Wood, D.; McHugh, T. H. *J Food Sci* **2010**, *75*, N1.

(22) Samir, M. A. S. A.; Alloin, F.; Dufresne, A. *Biomacromolecules* **2005**, *6*, 612.

(23) Ma, H. Y.; Burger, C.; Hsiao, B. S.; Chu, B. *Biomacromolecules* **2011**, *12*, 970.

(24) Yang, Q. L.; Wu, C. N.; Saito, T.; Isogai, A. *Carbohyd Polym* **2014**, *100*, 179.

(25) Entcheva, E.; Bien, H.; Yin, L. H.; Chung, C. Y.; Farrell, M.; Kostov, Y. *Biomaterials* **2004**, *25*, 5753.

(26) Zhang, T. J.; Wang, W.; Zhang, D. Y.; Zhang, X. X.; Ma, Y. R.; Zhou, Y. L.; Qi, L. M. *Adv Funct Mater* **2010**, *20*, 1152.

(27) Sevillano, G.; Rodriguezpuyol, M.; Martos, R.; Duque, I.; Lamas, S.; Diezmarques, M. L.; Lucio, J.; Rodriguezpuyol, D. *Nephrol Dial Transpl* **1990**, *5*, 497.

(28) Malainine, M. E.; Mahrouz, M.; Dufresne, A. *Compos Sci Technol* **2005**, *65*, 1520.

(29) Habibi, Y.; Mahrouz, M.; Vignon, M. R. *Food Chem* **2009**, *115*, 423.

(30) Leitner, J.; Hinterstoisser, B.; Wastyn, M.; Keckes, J.; Gindl, W. *Cellulose* **2007**, *14*, 419.

(31) Iwamoto, S.; Nakagaito, A. N.; Yano, H. *Appl Phys a-Mater* **2007**, *89*, 461.

(32) Wang, B.; Sain, M. *Compos Sci Technol* **2007**, *67*, 2521.

(33) Taniguchi, T.; Okamura, K. *Polym Int* **1998**, *47*, 291.

(34) Pandey, J. K.; Lee, J. W.; Chu, W. S.; Kim, C. S.; Ahn, S. H. *Macromol Res* **2008**, *16*, 396.

(35) Habibi, Y.; Goffin, A. L.; Schiltz, N.; Duquesne, E.; Dubois, P.; Dufresne, A. *J Mater Chem* **2008**, *18*, 5002.

(36) Grunert, M.; Winter, W. T. *J Polym Environ* **2002**, *10*, 27.

(37) Bondeson, D.; Mathew, A.; Oksman, K. *Cellulose* **2006**, *13*, 171.

(38) Braun, B.; Dorgan, J. R.; Chandler, J. P. *Biomacromolecules* **2008**, *9*, 1255.

(39) Araki, J.; Wada, M.; Kuga, S. *Langmuir* **2001**, *17*, 21.

(40) van den Berg, O.; Capadona, J. R.; Weder, C. *Biomacromolecules* **2007**, *8*, 1353.

(41) Dong, X. M.; Revol, J. F.; Gray, D. G. *Cellulose* **1998**, *5*, 19.

(42) Beck-Candanedo, S.; Roman, M.; Gray, D. G. *Biomacromolecules* **2005**, *6*, 1048.

(43) Saito, T.; Kimura, S.; Nishiyama, Y.; Isogai, A. *Biomacromolecules* **2007**, *8*, 2485.

(44) Saito, T.; Hirota, M.; Tamura, N.; Kimura, S.; Fukuzumi, H.; Heux, L.; Isogai, A. *Biomacromolecules* **2009**, *10*, 1992.

(45) Siro, I.; Plackett, D. *Cellulose* **2010**, *17*, 459.

(46) Isogai, A.; Saito, T.; Fukuzumi, H. *Nanoscale* **2011**, *3*, 71.

(47) Montanari, S.; Rountani, M.; Heux, L.; Vignon, M. R. *Macromolecules* **2005**, *38*, 1665.

(48) Habibi, Y.; Chanzy, H.; Vignon, M. R. *Cellulose* **2006**, *13*, 679.

(49) Sugiyama, J.; Vuong, R.; Chanzy, H. *Macromolecules* **1991**, *24*, 4168.

(50) Sugiyama, J.; Harada, H.; Fujiyoshi, Y.; Uyeda, N. *Planta* **1985**, *166*, 161.

(51) Helbert, W.; Nishiyama, Y.; Okano, T.; Sugiyama, J. *J Struct Biol* **1998**, *124*, 42.

(52) OSullivan, A. C. *Cellulose* **1997**, *4*, 173.

(53) Kuga, S.; Brown, R. M. *Polym Commun* **1987**, *28*, 311.

(54) Leppanen, K.; Andersson, S.; Torkkeli, M.; Knaapila, M.; Kotelnikova, N.; Serimaa, R. *Cellulose* **2009**, *16*, 999.

(55) Ioelovich, M.; Leykin, A. *Bioresources* **2008**, *3*, 170.

(56) Fink, H. P.; Hofmann, D.; Philipp, B. *Cellulose* **1995**, *2*, 51.

(57) Li, Q. Q.; Renneckar, S. *Biomacromolecules* **2011**, *12*, 650.

(58) Zuo, X.; Grishaev, A. *Solution Small Angle X-ray Scattering: Basic Principles and Experimental Aspects*, 2009.

(59) Kapoor, K.; Lahiri, D.; Rao, S. V. R.; Sanyal, T.; Kashyap, B. P. *B Mater Sci* **2004**, *27*, 59.

(60) Scardi, P.; Leoni, M.; Delhez, R. *J Appl Crystallogr* **2004**, *37*, 381.

(61) Sarkar, A.; Mukherjee, P.; Barat, P. *Z Kristallogr* **2007**, 543.

(62) Burger, C.; Hsiao, B. S.; Chu, B. *Polym Rev* **2010**, *50*, 91.

(63) Svergun, D. I.; Koch, M. H. J. *Rep Prog Phys* **2003**, *66*, 1735.

(64) Pedersen, J. S. *Adv Colloid Interfac* **1997**, *70*, 171.

(65) Pedersen, J. S. In *Neutrons, X-Rays and Light*; Zemb, T., Lindner, P., Eds.; Elsevier Science: Amsterdam, 2002.

(66) Klein, R. In *Neutrons, X-Rays and Light*; Zemb, T., Lindner, P., Eds.; Elsevier Science: Amsterdam, 2002.

Chapter 2 Cellulose Nanofibers Extracted from Dried Pulps

2.1 Introduction

As introduced in Chapter 1, lignin takes up to 40% by weight in plant cell wall. In paper industry, the removal of lignin is an important step to improve the whiteness and strength of the paper, and the separation of cellulose fibers from lignin usually happens in the pulping process. Generally, two types of chemical pulping processes, namely the Kraft process (alkaline method) and the sulfite process (acidic method), can be used to remove most of the lignin in the wood.

The Kraft process adopts a mixture solution of sodium hydroxide (NaOH) and sodium sulfide (Na_2S) to dissolve lignin and to break the bonds between cellulose/hemicellulose and lignin, while the sulfite process uses a mixture of sulfurous acid (H_2SO_3) and bisulfide ions (HSO_3^-) to remove lignin from cellulose[1]. Both methods can effectively remove most of the lignin and some of the hemicellulose between cellulose microfibrils. The difference relies on the condition that the acidic environment in the sulfite process can cause hydrolysis of cellulose during the process, and consequently, the degradation of cellulose will decrease the fiber strength[2]. In addition, the Kraft process works for both soft wood and hard wood, while the sulfite pulping process is only suitable for those species with low extractive (e.g. polyphenol, pigments, fat, etc.) content[3].

To remove the residual lignin (<5%) and improve the brightness of the pulp, the chemical pulping process is usually followed by a bleaching process[3], which is a continuation of the delignification process. In the bleaching process, caustic chemicals (e.g. chlorine gas, hypochlorite, chlorine dioxide, oxygen or hydrogen peroxide) are used to further dissolve the remaining lignin[3]. After washing with water and drying, the pulp consists of almost pure cellulose fibers.

In dried wood pulp, cellulose microfibrils, which were originally separated by the lignin, now adhere to each other and form thick bundles. With the purpose of dispersing the cellulose microfibrils into aqueous suspension, the TEMPO-mediated oxidation followed by mechanical homogenization was performed to the dried pulp of different species (i.e. soft wood, cotton and bamboo), and the structural information of the extracted cellulose nanofibers was revealed through the analysis of solution SAXS data and TEM images.

2.2 Materials and Methods

2.2.1 Materials

Biofloc-96 pulp (fully bleached sulfite maritime pine wood pulp with I_α cellulose content of 96%) was provided by Tembec Tartas factory in France; Cotton-7350 pulp (dried pulp with viscosity average degree of polymerization of 7350) were provided by Buckeye Technologies, Inc. in USA; Kraft-processed bamboo pulp was provided by Crown Marina Co. Ltd., Thailand; vacuum dried raw jute fibers were provided by Redbud Textile Tech. Inc., Jiangsu, China; TEMALFA-95 (fully bleached sulfite spruce wood pulp with I_α cellulose content of 95%) was provided by Tembec Inc., Canada. 2,2,6,6-tetramethyl-1- piperidinyloxy (TEMPO), sodium hypochlorite (NaClO), sodium bromide (NaBr) were purchased from Sigma-Aldrich.

2.2.2 Extraction of Cellulose Nanofiber from Dried Pulp

For Biofloc-96, Cotton-7350, bamboo and jute samples, cellulose nanofibers were prepared by using the TEMPO-mediated oxidation approach with the following procedures. Pulps (1 g) were first broken down into small pieces and then soaked in water (about 30 mL) overnight. Both sodium bromide (0.1 g) and TEMPO agent (0.02 g) were dissolved in the suspension. A desired amount of sodium hypochlorite solution (12 mmol per gram of cellulose)

was subsequently added to initiate the oxidization process, where the reaction was under mechanical stirring in a sealed bottle for 24 hours. The pH value of the suspension was kept between 10.0 and 11.0 during the reaction (monitored with a pH meter) by addition of sodium hydroxide aqueous solution (1 mol/L). The oxidized cellulose fibrous samples were collected by centrifuging the reaction mixture at ~2350 g, followed by washing with deionized water for several times until the pH value reached ~8. Afterward, all fibrous samples were dispersed in 100 mL of water and disintegrated with a homogenizer (Cole Parmer, VCX-400) at 79% rate (60 Hz, 115 W) for 10 min. The suspension was centrifuged again at ~4700 g for 30 min, where the supernatant containing finely dispersed cellulose nanofibers was collected for X-ray measurements. The concentration of the cellulose nanofiber suspension was determined by Total Organic Carbon (TOC) analyzer (TOC-V CPN, SHIMADZU Corporation, Japan).

For the TEMALFA-95 sample, different experimental parameter combinations (i.e. the amount of NaClO used, the reaction time, and the length of homogenization time) were used to prepare nanofiber suspensions with the purpose of studying how each parameter effect on the morphology and degree of oxidation of nanofibers. The preparation of these samples followed the same procedure as described above, and the specific experimental parameters are listed in Table 2.1.

Table 2.1 Experimental parameters for the preparation of TEMALFA-95 series cellulose nanofiber samples

	Dose of NaClO (mmol per gram of cellulose)	Reaction Time (hour)	Homogenization Time (min)
TEMALFA-RO0.8	**0.8**	24	10
TEMALFA-RO1.7	**1.7**	24	10
TEMALFA-RO2.5	**2.5**	24	10
TEMALFA-RO5	**5**	24	10
TEMALFA-RO9	**9**	24	10
TEMALFA-RO12	**12**	24	10
TEMALFA-TM2	12	**2**	10
TEMALFA-TM4	12	**4**	10
TEMALFA-TM7	12	**7**	10
TEMALFA-TM24	12	**24**	10
TEMALFA-TM48	12	**48**	10
TEMALFA-HM2	9	24	**2**
TEMALFA-HM10	9	24	**10**
TEMALFA-HM15	9	24	**15**

Note: the bold numbers in the table indicate the changing parameters of the experiment, while other experimental conditions remained the same. The homogenization was always performed at 60 Hz, 115 W.

2.2.3 Determination of Degree of Oxidation (DO)

The ratio between the amount of oxidized and the total hydroxymethyl groups in oxidized cellulose was determined through the conductometric titration method[4]. Briefly, 0.1 mol/L of hydrochloric acid aqueous solution were dropped to 24 mL of cellulose nanostrip suspension at a cellelose concentration of 0.05 wt% until the pH reached to 2.8. The suspension was titrated with 0.005 mol/L NaOH solution, and the suspension was kept under stirring at rate of 450 rpm using a magnetic stirrer . The conductivity of the suspension was monitored using a conductivity meter throughout the titration process. The titration performance was terminated when the pH reached

10.7. The curve of conductivity versus volume of NaOH solution used was plotted, and the volume of NaOH aqueous solutions used to neutralize the carboxyl groups, V, was determined from the curve. The amount of oxidized hydroxymethyl groups was calculated by multiplying V with the concentration, C, of the NaOH solution, while the amount of cellulose was directly measured from the TOC analyzer. A example curve of conductivity vs. volume of NaOH solution added to the typical cellulose suspension is shown in Figure 2.1. From the figure, the degree of oxidation (DO) for the studied cellulose nanofiber sample could be calculated as: $162\text{g/mol} \times 0.04\text{M} \times (V_2 - V_1) \times 10^{-3} / (100\text{g} \times 0.1\text{wt}\%) = 0.198$ (where 162 is the molecular weight of the glucose unit, V_1 and V_2 are the amount of NaOH solution at the two inflection points of the curve).

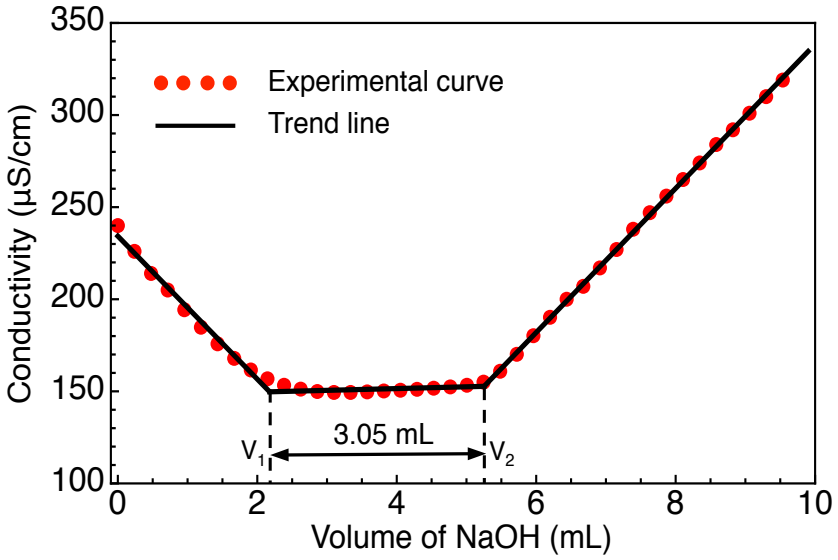

Figure 2.1 Conductometric curve of the oxidized B86 cellulose nanofibers

2.2.4 Solution SAXS/WAXD Characterization

Simultaneous solution SAXS/WAXS (wide-angle X-ray scattering) measurements of cellulose nanofiber suspensions at different concentrations were carried out at the X9 Beamline in the National Synchrotron Light Source (NSLS), Brookhaven National Laboratory (BNL).

During the scan, a 20-μL suspension sample was automatically pumped into a glass capillary with a diameter of 1 mm, sealed across the vacuum path. The sample continuously flowed through the capillary during data collection in order to minimize radiation damage.[5] The X-ray wavelength was set at 0.0918 nm. The PILATUS 300k detector (20 Hz noise-free 2D X-ray detector, DECTRIS Ltd., Switzerland) located at 3.2 m away from the sample was used to collect the SAXS data. A custom-designed Photonic Science (Photonic Science Ltd., France) CCD detector, which was 463 mm away from the sample, worked as the WAXS detector. For each sample, three scans were taken with each scan period of 30 seconds. The average of these three scans was used as the scattering pattern of the sample. Silver behenate standard was used to calibrate the parameters that define the scattering geometry (i.e., beam center and sample-to-detector distance). Preliminary data processing was accomplished using a Python-based package developed at the X9 Beamline to convert the 2D images into one-dimensional scattering profiles, block off dead pixels and pixels behind the beam stop, merge SAXS and WAXS scans, and subtract the buffer and capillary background from the scattering profile.

2.2.5 Transmission Electron Microscopy (TEM)

Drops (about 10 μL) of cellulose nanofiber suspension with concentration around 0.1 wt% were deposited onto a carbon film coated copper grid (300 mesh). The suspension was allowed to stay on the grid for 3 min and then the excess liquid was drawn off the grid using filter paper. Before drying, 5 μL 1.5 wt% phosphotungstic acid (PTA) solution was dropped on top of the grid and kept for about 30 seconds before absorbed by filter paper. The staining step was repeated once. The negatively stained sample was left in air until completely dry and then stored in desiccator until use. The TEM observation was performed at the Center for Functional Nanomaterials (CFN) in BNL using JEOL JEM-1400 microscope (JEOL, Tokyo, Japan)

equipped with a CCD camera (ORIUS SC200, Gatan, Inc., US) operated at 100 kV.

2.3 Model Development for Solution SAXS Analysis

2.3.1 Theoretical Basis

According to the SAXS theory, the scattering intensity *I(s)* of a particle system is determined by two factors, the form factor containing the shape and size information of particles and the structure factor, which is related to the ordered mutual arrangement between particles[6]. The relationship can be written as:

$$I(s) = |F(s)|^2 S(s) \qquad \text{Eq. 2.1}$$

where s is the modulus of scattering vector ($s = 2\sin\theta/\lambda$), $|F(s)|^2$ is the form factor and $S(s)$ is the structure factor. For dilute solution or disordered system, the structure factor $S(s)$ is considered to be 1, and the intensity is only dominated by the structure factor $|F(s)|^2$, which holds true for all calculations in this chapter. $F(s)$ is the amplitude of the scattering, which is the Fourier transform of the electron density distribution in the particle.

2.3.2 Cylinder Model

Instinctively, it is easier to consider cellulose microfibrils as having a cylindrical shape[7]. Some papers also supported the cylinder morphology for cellulose microfibrils experimentally[8-10]. Therefore, a cylinder model with circular cross-sections was first developed and used to fit the experimental data. The average intensity distribution for cylinders having cross-sectional radius R and length L is[11]:

$$I(s) = (\pi R^2 L)^2 \int_0^{\pi/2} \left[\frac{J_1(2\pi Rs\sin\phi)}{\pi Rs\sin\phi} \right]^2 \left[\frac{\sin(\pi Ls\cos\phi)}{\pi Ls\cos\phi} \right]^2 \sin\phi d\phi \qquad \text{Eq. 2.2}$$

where J_1 is the Bessel function of the first kind, and ϕ is the polar angle. For wood cellulose nanofibers prepared through TEMPO-mediated oxidation, the lengths are around 1 μm, which are much larger than the cross-section diameters (5–10 nm)[12] and far exceed the size range (0.5–100 nm) for SAXS. Thus, the length L can be taken as infinitely long and the intensity distribution function can be reduced to[13]:

$$\frac{I(s)}{L} = \frac{1}{2s}(\pi R^2)^2 \left[\frac{J_1(2\pi sR)}{\pi sR}\right]^2 \quad \text{Eq. 2.3}$$

where the expression in the square brackets reaches the value 1 for $s = 0$.

Due to the polydispersity (in cross section) of cellulose nanofibers, the developed model must possess a size distribution on the cross-section diameter. For this purpose, the expressions of the cylinder model having Gaussian distribution and Gamma distribution are shown in Eqs. 2.4 and 2.5, respectively:

$$\frac{I(s)}{L} = \frac{1}{2s}\int_0^\infty (\pi R^2)^2 \left[\frac{J_1(2\pi sR)}{\pi sR}\right]^2 \frac{1}{\sqrt{2\pi}\sigma}\exp\left[-\frac{(R-R_0)^2}{2\sigma^2}\right]dR \quad \text{Eq. 2.4}$$

$$\frac{I(s)}{L} = \frac{1}{2s}\int_0^\infty (\pi R^2)^2 \left[\frac{J_1(2\pi sR)}{\pi sR}\right]^2 \frac{1}{\Gamma\left[\left(\frac{R_0}{\sigma}\right)^2\right]} \frac{\left(\frac{RR_0}{\sigma^2}\right)^{\left(\frac{R_0}{\sigma}\right)^2}}{R}\exp\left[-\frac{RR_0}{\sigma^2}\right]dR \quad \text{Eq. 2.5}$$

where R_0 is the number average radius of cross-section, σ is the standard deviation of the corresponding distribution.

2.3.3 Ribbon Model

The ribbon model assumes a rectangular cross-section, which is originated from the parallelepiped model developed by Mittelbach and Porod [6]:

$$I(s)=\frac{(abc)^2}{4\pi}\int_0^{2\pi}\int_0^{\pi}\left[\frac{\sin(\pi sa\sin\phi\cos\psi)}{\pi sa\sin\phi\cos\psi}\frac{\sin(\pi sb\sin\phi\sin\psi)}{\pi sb\sin\phi\sin\psi}\frac{\sin(\pi sc\cos\phi)}{\pi sc\cos\phi}\right]^2\sin\phi d\phi d\psi \qquad \text{Eq. 2.6}$$

where a, b and c are the side lengths of the parallelepiped, ϕ and ψ are the polar angle and azimuthal angle, respectively. Given that the axis of cellulose nanofiber is along the c direction of the rectangular parallelepiped and the cross-section is in the a-b plane, c can be treated as infinitely long compared to a and b. Equation 2.6 gives the average of the intensity of an oriented particle over all possible orientations in reciprocal space. In order to learn about the scattering geometry, one has to study the intensity distribution of the infinitely long rod along $\mathbf{s_1}$, $\mathbf{s_2}$ and $\mathbf{s_3}$, which are the Cartesian coordinate axes in reciprocal space and superimposed with the a, b and c axes in real space. As c is very large, the $\left[\frac{\sin(\pi sc\cos\phi)}{\pi sc\cos\phi}\right]^2$ in Equation 2.6 denoting the intensity distribution along $\mathbf{s_3}$ resembles a delta function of $\cos\phi$, which has its maximum when $\cos\phi = 0$ and drops to zero rapidly as $\cos\phi$ extends. This behavior indicates that the infinitely long rod contributes to the scattering intensity when the scattering vector $\mathbf{s}$ is almost perpendicular to c ($\phi \approx 90°$). Consequently, $\sin\phi$ can be treated as 1 in the other two parts of the Eq. 2.6, which results in:

$$I(s)=\frac{(abc)^2}{4\pi}\int_0^{2\pi}\left[\frac{\sin(\pi sa\cos\psi)}{\pi sa\cos\psi}\frac{\sin(\pi sb\sin\psi)}{\pi sb\sin\psi}\right]^2 d\psi\int_0^{\pi}\left[\frac{\sin(\pi sc\cos\phi)}{\pi sc\cos\phi}\right]^2\sin\phi d\phi \qquad \text{Eq. 2.7}$$

With $\cos\phi$ substituted by x, the integral of ϕ can be written as $\int_{-1}^{1}\left[\frac{\sin(\pi scx)}{\pi scx}\right]^2 dx$, while:

$$\int_{-1}^{1}\left[\frac{\sin(\pi scx)}{\pi scx}\right]^2 dx \approx \int_{-\infty}^{\infty}\left[\frac{\sin(\pi scx)}{\pi scx}\right]^2 dx = \frac{1}{cs} \qquad \text{Eq. 2.8}$$

Therefore the Equation 2.6 can be simplified into:

$$\frac{I(s)}{c}=\frac{(ab)^2}{4\pi s}\int_0^{2\pi}\left[\frac{\sin(\pi sa\cos\psi)}{\pi sa\cos\psi}\frac{\sin(\pi sb\sin\psi)}{\pi sb\sin\psi}\right]^2 d\psi \qquad \text{Eq. 2.9}$$

As there is no analytical solution for the integral in Equation 2.9, although it could be functionally used in model fitting, the computational cost is very high because the numerical integration of the above expression is extremely slow, let alone the calculation with further consideration of the size distributions of *a* and *b*. With the purpose of improving the computational efficiency, we are going to implement a series of simplifications to Equation 2.9.

Let us first consider the intensity distribution in the $\mathbf{s_1}$-$\mathbf{s_2}$ plane. We assume that the side length *a* of the rectangular cross-section is much less than the side length *b*. Under this assumption, the 2D Fourier Transform of the rectangle in reciprocal space has much wider intensity distribution along $\mathbf{s_1}$ compared to that along $\mathbf{s_2}$. In this case, the polar angle ψ remains small, resulting in $\cos\phi \approx 1$. As a result, Equation 2.9 can be rewritten into:

$$\frac{I(s)}{c} = \frac{(ab)^2}{4\pi s}\left[\frac{\sin(\pi sa)}{\pi sa}\right]^2 \int_0^{2\pi}\left[\frac{\sin(\pi sb\sin\psi)}{\pi sb\sin\psi}\right]^2 d\psi \qquad \text{Eq. 2.10}$$

Since the integral part in Equation 2.10 approximates to 2π timing a hypergeometric function ${}_1\mathrm{F}_2\left(\frac{1}{2};\frac{3}{2},2;-\pi^2 s^2 b^2\right)$, the scattering intensity $I(s)$ of the ribbon-like fibers can be expressed as:

$$\frac{I(s)}{c} = \frac{(ab)^2}{2s}\left[\frac{\sin(\pi sa)}{\pi sa}\right]^2 {}_1\mathrm{F}_2\left(\frac{1}{2};\frac{3}{2},2;-\pi^2 s^2 b^2\right) \qquad \text{Eq. 2.11}$$

From Equaiton 2.9 to Equation 2.11, the shape of the cross-section changes slightly from the regular rectangle with thickness of *a* and width of *b* into the one with two ends rounded (Figure 2.2).

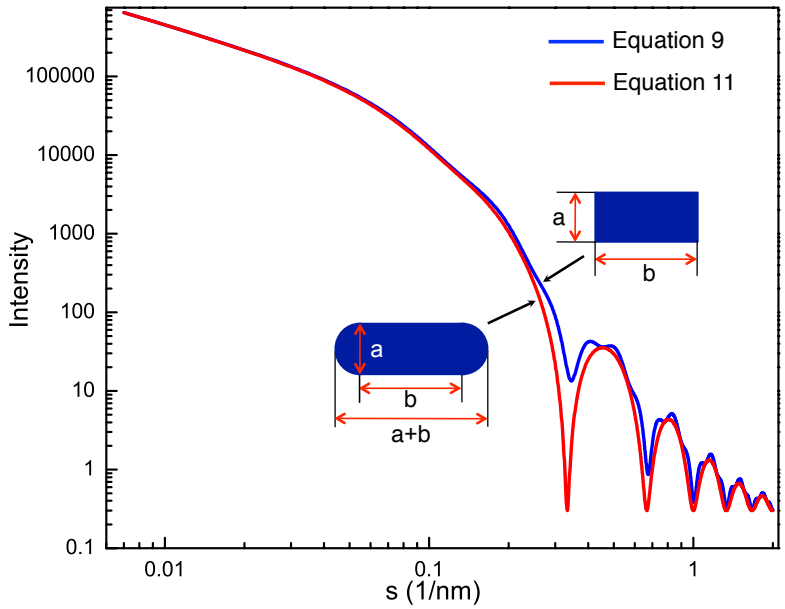

Figure 2.2 Scattering profiles calculated by Equations 2.9 and 2.11 with a = 3 nm, and b = 9 nm.

Besides the mathematical approximation described above, the relationships in Equation 2.11 can be derived in a more intuitive way. For the rectangle with two rounded ends, it can be considered as the convolution of a circle with diameter *a* and the electron density decreasing from the edge to the center along a line with length *b*, which produces the final shape with uniform electron density inside the rectangle. Since the Fourier transform of a convolution equals to the inner product of the Fourier transforms of each functions involved in the convolution ($\mathcal{F}\{f*g\}=\mathcal{F}\{f\}\cdot\mathcal{F}\{g\}$), the amplitude of scattering from the cross-section is, therefore, the product of the Fourier transforms of the electron density distribution within the circle and the line segment, respectively. Assuming the electron density distribution function in the circle is:

$$f(r)=\begin{cases}\dfrac{2}{\pi\sqrt{a^2-4r^2}}, & 0<r<\dfrac{1}{2}a\\ 0, & r\geq\dfrac{1}{2}a\end{cases} \qquad \text{Eq. 2.12}$$

where r is the radius of the circle in the ribbon model, the amplitude F_a is the two-dimensional Fourier transform of $f(r)$:

$$F_a(s) = \mathcal{F}_2\{f(r)\} = \int_0^{a/2} 2\pi \, \mathrm{J}_0(2\pi sr) \frac{2}{\pi\sqrt{a^2 - 4r^2}} rdr = a\frac{\sin(\pi sa)}{\pi sa} \qquad \text{Eq. 2.13}$$

We can further define the normalized square-well function as follows:

$$\Pi(r) = \begin{cases} 0, \ |r| > \dfrac{1}{2} \\ 1, \ |r| \le \dfrac{1}{2} \end{cases} \qquad \text{Eq. 2.14}$$

Then the electron density distribution of the line segment with length b can be expressed as $\Pi(r/b)$. The amplitude is then the 1D Fourier transform:

$$F_b(s) = \mathcal{F}_1\left\{\Pi\left(\frac{r}{b}\right)\right\} = \int_{-b/2}^{b/2} \exp(-2\pi irs\sin\psi) dr = b\frac{\sin(\pi bs\sin\psi)}{\pi bs\sin\psi} \qquad \text{Eq. 2.15}$$

where ψ is the azimuthal angle.

Since the amplitude above counts only one fixed direction, to obtain the intensity $I(s)$, the form factor $F_b^2(s)$ needs to be averaged over all possible orientations in the cross-section plane:

$$\left\langle F_b^2(s)\right\rangle_\psi = \frac{b^2}{2\pi}\int_0^{2\pi}\left[\frac{\sin(\pi sb\sin\psi)}{\pi sb\sin\psi}\right]^2 d\psi \approx b^2 \, {}_1\mathrm{F}_2\left(\frac{1}{2};\frac{3}{2},2;-\pi^2 s^2 b^2\right) \qquad \text{Eq. 2.16}$$

Accordingly, the intensity from the cross-section $I_{ab}(s)$ is:

$$I_{ab}(s) = F_a^2(s)\left\langle F_b^2(s)\right\rangle_\psi = (ab)^2\left[\frac{\sin(\pi sa)}{\pi sa}\right]^2 {}_1\mathrm{F}_2\left(\frac{1}{2};\frac{3}{2},2;-\pi^2 s^2 b^2\right) \qquad \text{Eq. 2.17}$$

Taking the contribution from the c direction ($\frac{c}{2s}$) into account, the total intensity $I(s)$ would exactly be Equaiton 2.11. With the small difference in the shape of the cross-section, there is a

minor discrepancy between the profiles of the two curves before and after the approximation (as seen in Figure 2).

Considering the polydispersity of cellulose nanofibers, Gamma distributions can be applied to *a* and *b*, respectively:

$$\frac{I(s)}{c} = \frac{1}{2s}\int_0^\infty a^2 \left[\frac{\sin(\pi as)}{\pi as}\right]^2 f_\Gamma(a;a_0,\sigma_a)da \int_0^\infty b^2 \, {}_1\mathrm{F}_2\left(\frac{1}{2};\frac{3}{2},2;-\pi^2 s^2 b^2\right) f_\Gamma(b;b_0,\sigma_b)db \qquad \text{Eq. 2.18}$$

$$f_\Gamma(a;a_0,\sigma_a) = \frac{\exp\left(-\frac{a_0 a}{\sigma_a^2}\right)\left(\frac{a_0 a}{\sigma_a^2}\right)^{\frac{a_0^2}{\sigma_a^2}}}{a\Gamma\left(\frac{a_0^2}{\sigma_a^2}\right)} \qquad \text{Eq. 2.19}$$

$$f_\Gamma(b;b_0,\sigma_b) = \frac{\exp\left(-\frac{b_0 b}{\sigma_b^2}\right)\left(\frac{b_0 b}{\sigma_b^2}\right)^{\frac{b_0^2}{\sigma_b^2}}}{b\Gamma\left(\frac{b_0^2}{\sigma_b^2}\right)} \qquad \text{Eq. 2.20}$$

where a_0, b_0, σ_a and σ_b are the number averages and standard deviations of the thickness *a* and width *b* of the cross-section, respectively. In addition, the size-weighted average of each parameter (i.e. a_w, b_w, σ_{aw} and σ_{bw}) can be calculated through the following formulae:

$$a_w = \frac{a_0^2 + \sigma_a^2}{a_0} \qquad \text{Eq. 2.21}$$

$$b_w = \frac{b_0^2 + \sigma_b^2}{b_0} \qquad \text{Eq. 2.22}$$

$$\sigma_{aw}^2 = \int_0^\infty f_\Gamma(a;a_0,\sigma_a)(a-a_w)^2 da \qquad \text{Eq. 2.23}$$

$$\sigma_{bw}^2 = \int_0^\infty f_\Gamma(b;b_0,\sigma_b)(b-b_w)^2 db \qquad \text{Eq. 2.24}$$

Substituting the analytical solutions of the integrals in Equation 2.18, we get:

$$\frac{I(s)}{c}=\frac{1}{4\pi^2 s^3}\left\{1-\mathrm{Re}\left[(1+2i\pi s\frac{\sigma_a^2}{a_0})^{-\left(\frac{a_0}{\sigma_a}\right)^2}\right]\right\}(b_0^2+\sigma_b^2)_3\mathrm{F}_2\left(\frac{1}{2},1+\frac{b_0^2}{2\sigma_b^2},\frac{3}{2}+\frac{b_0^2}{2\sigma_b^2};\frac{3}{2},2;-\frac{4\pi^2 s^2\sigma_b^4}{b_0^2}\right) \quad \text{Eq. 2.25}$$

Equaiton 2.25 is going to be used as the final model in nonlinear least square fitting to best fit the experimental intensity patterns. Although complicated as it appears, the model contains only four essential parameters, including the two size parameters of the cross-section and their standard distributions. Furthermore, since it is an analytical expression, the process of the model fitting can be performed with high computing efficiency.

2.4 Results and Discussion

2.4.1 Extracting Scattering Profiles from the Suspension of Cellulose Nanofibers

The as-measured scattering profile of the suspension sample possessed three contributions: the 'nanofiber sample', the buffer solution, and the capillary holder. The background intensity due to the buffer and capillary contributions could be subtracted from the experimental intensity using the following equation[5]:

$$I_{cor}=I_{sample}-I_{dark}-\frac{T_{sample}}{T_{buffer}}\left(I_{buffer}-I_{dark}\right)\times(1-F)-\frac{T_{sample}}{T_{empty}}\left(I_{empty}-I_{dark}\right)\times F \quad \text{Eq. 2.26}$$

where I_{cor}, I_{sample}, I_{buffer}, I_{empty} and I_{dark} are the background corrected scattering intensity, intensity from the suspension sample, intensity from the buffer, intensity from the empty capillary and detector background without the incident X-ray beam, respectively. T_{sample}, T_{buffer} and T_{empty} are the total transmitted intensities after the X-ray beam has passed through the sample, buffer and 'empty' capillary, respectively. F is the volume fraction of the nanoparticles. In this experiment, the buffer was deionized water. As the suspensions were very dilute (F less than 0.5 vol%) and all the measurements were performed with the same capillary, the capillary scattering was treated together with the buffer scattering as one background item in the calculation. The plot with error bars after background subtraction is shown in Figure 2.3.

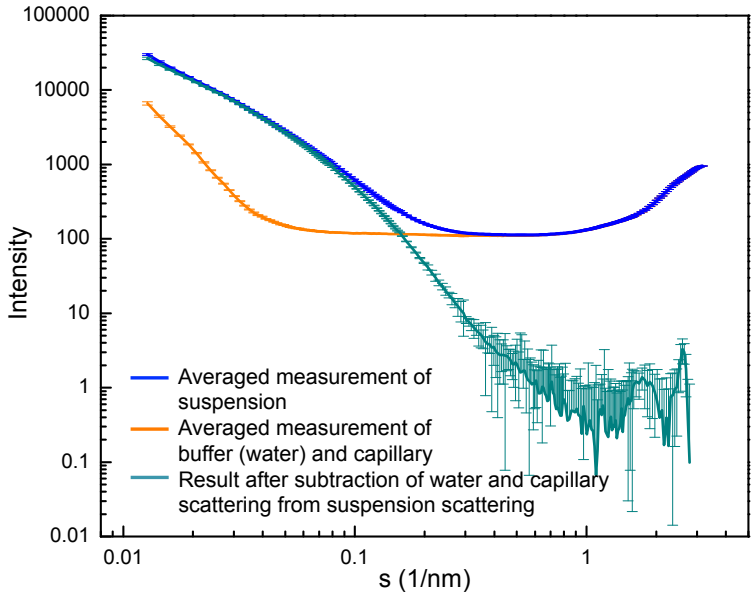

Figure 2.3 Extraction of scattering profile from TEMPO-oxidized cellulose nanofibers by subtracting the buffer (water) scattering from the as-measured suspension scattering profile

2.4.2 Fitting Scattering Profile with Cylinder Model

Taking the scattering patterns obtained from the sample Biofloc-96 for example, since the profiles did not show any discernible sharp peak in the small-angle region ($s \sim 0.01-1$ nm^{-1}), the observation clearly suggested a size polydispersity of the cellulose nanofiber system. Therefore, a distribution on the cross-section radius R needed to be integrated to the cylinder model. Two assumed distributions were proposed in this calculation: symmetric Gaussian distribution and skewed Gamma distribution (Figure 2.4). The Gaussian distribution was used as a first approximation because of its simplicity and generality, while the Gamma distribution was chosen to represent the asymmetrical case considering the convenience of obtaining an analytical solution of the integral when compared with other skewed distributions, e.g. the lognormal distribution. For both distributions, there were two parameters involved: the mean radius R_0 and the corresponding standard deviation σ, which measured the amount of dispersion of the radius, i.e. the smaller the standard deviation, the more uniform the sizes were.

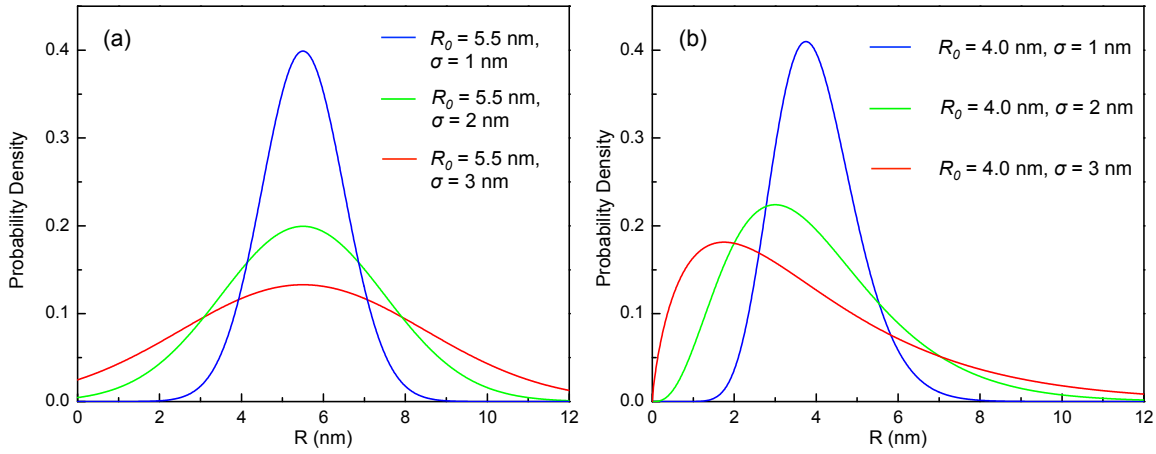

Figure 2.4 Probability density functions comparison of (a) Gaussian distribution and (b) Gamma distribution. R_0 and σ are the mean and standard deviation for each distribution, respectively.

The fitting of the cylinder model with either the Gaussian distribution or the Gamma distribution to the experimental data in the small-angle region was performed using the Nonlinear Model Fit in *Mathematica*[14]. The coefficients of determination, R^2 (a number evaluates how well the model fit the data, i.e. the closer to 1 the value, the better the model fits the data), for the models with Gaussian distribution and Gamma distribution were 0.987 and 0.997, respectively. Values of the Akaike information criterion[15] (AIC, the lower the value, the less information loss) for the two models were 1612 and 1237, respectively. Based on the R^2 and AIC values only, the cylinder model with the Gamma distribution indicated a better fit to the sample scattering profile. However, the discrepancy between both models and the experimental data (Figure 2.5) was obvious, especially in the high s range ($s > 0.1$ nm^{-1}).

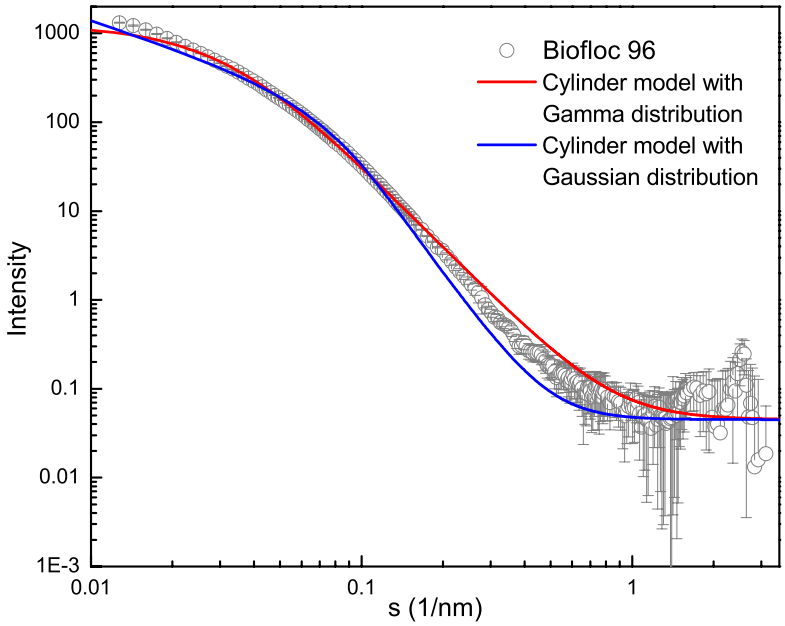

Figure 2.5 Comparison between scattering profile from Biofloc-96 cellulose nanofiber suspension at concentration 0.1 wt% and cylinder models with Gamma distribution (size-weighted average of cross-section radius R_w = 4.0 nm with standard deviation σ = 3.0 nm) and Gaussian distributions (size-weighted average radius R_w = 5.5 nm with standard deviation σ = 3.2 nm).

To exclude the possibility that a certain size distribution would qualify the cylinder model to fit the experimental pattern, an inverse method was used to derive the size distribution from an estimated equation that could fit the scattering profile and the known monodisperse cylinder model. It was observed from the scattering pattern that the intensity in the initial region (s ~ 0.01−0.03 nm^{-1}) followed s^{-1} trend and that in the Porod's region (s ~ 0.1−0.5 nm^{-1}) followed s^{-4}. Based on these trends, an equation (Equation 2.27) simulating the shape of the experimental curve was developed and fitted to the experimental data by adjusting the parameters f, p and bg (Figure 2.6(a)).

$$F(s) = f\frac{1}{2s(1+4p^2\pi^2s^2)^{3/2}} + bg \qquad \text{Eq. 2.27}$$

Assuming that Equation 2.27 was the integral of the monodisperse cylinder model $I(s,R)$ (Equation 2.3) and a radius distribution $\varphi(R)$ (i.e., $F(s)=\int_0^\infty I(s,R)\varphi(R)dR$), the latter could yield:

$$\varphi(R)=\frac{2\mathrm{K}_1(2R/p)}{p^5\pi^2} \qquad \text{Eq. 2.28}$$

where K_1 is the modified Bessel function of the second kind, R is the cylinder radius, and p is a parameter regulating the shape of the curve, the same to the p in Equation 2.27. The term $\varphi(R)$ tended toward infinity as R approached 0 (Figure 2.6(b)), implying that this function could not converge in the $R \geq 0$ region, which disqualified itself from being a distribution function. Hence, without a proper size distribution to fit the experimental data, the cylinder model was highly unlikely to be a satisfying model for the cellulose nanofiber system.

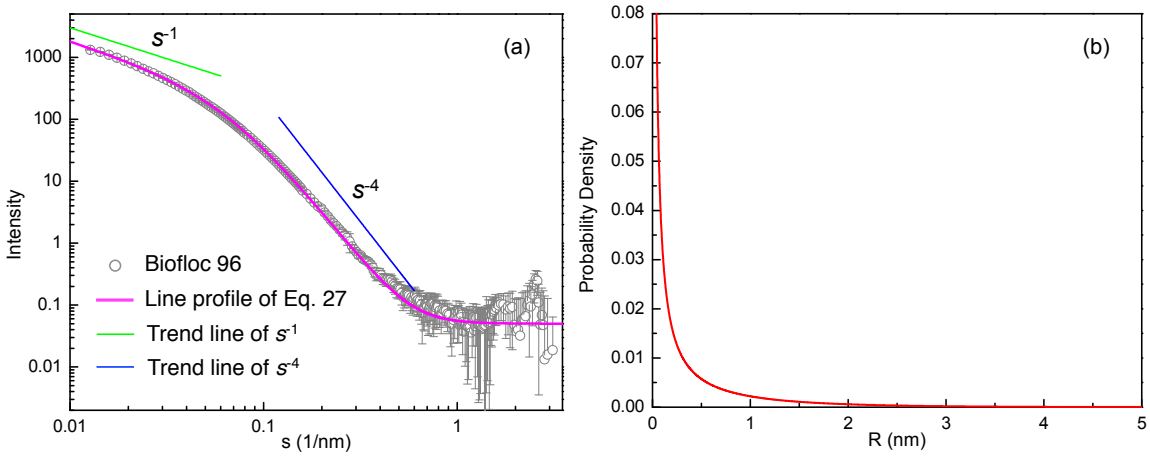

Figure 2.6 Comparison between the $F(s)$ (Equation 27) curve and the scattering profile from Biofloc96 sample. The parameters used in the equation were: $f = 37$, $p = 2.35$, and $bg = 0.05$, respectively. (b) The shape of $\varphi(R)$ (Equation 28) with $p = 2.35$, indicating that this function could not converge in the $R \geq 0$ region.

2.4.3 Fitting Scattering Profile with Ribbon Model

In contrast, the ribbon model containing a near rectangular cross-section was found to be able to fit the SAXS/WAXS profiles for cellulose nanofibers with great satisfaction. For example, Figure 2.7 illustrates the scattering profile of Biofloc-96 sample over a large angular range ($s \sim 0.01-1$ nm^{-1}) and the fitting results using the ribbon model with four parameters (the average thickness and width of cross-section a_0 and b_0, and their corresponding standard deviation σ_a and σ_b). The coefficient of determination R^2 for the nonlinear regression was larger than 0.9999, and the AIC was 509, which was much lower than those from using the cylinder models (e.g. AIC values were 1612 and 1237 for the cylinder models with Gaussian and Gamma distributions, respectively). This indicated that when compared with the cylinder model, the two additional parameters in the ribbon model did not increase the complexity. In contrary, the ribbon model led to better fitting results with less information loss.

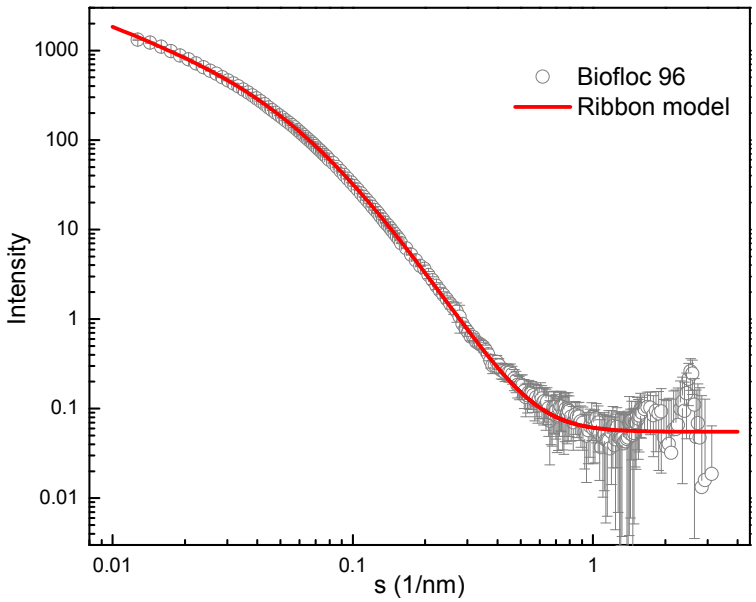

Figure 2.7 Experimental SAXS/WAXS profile from Biofloc96 cellulose nanofiber suspension at concentration of 0.1 wt% and the fitting result using the ribbon model. The size-weighted average parameters for the best fit were: $a_w = 3.2$ nm with standard deviation $\sigma_a = 2.2$ nm, $a_w + b_w = 12.7$ nm with standard deviation $\sigma_{a+b} = 5.5$ nm. The analysis to the wide-angle region (s larger than 1 nm^{-1}) was not displayed in this figure.

The ribbon model having size-weighted averages of thickness a_w = 3.2 nm with standard deviation σ_a = 2.2 nm and width $a_w + b_w$ = 12.7 nm with standard deviation σ_{a+b} = 5.5 nm was also found to best fit the scattering profiles from Biofloc-96 suspensions at four different concentrations (i.e., 0.05, 0.1, 0.3 and 0.6 wt%). The fitting results only differed each other in the scaling factor, which increased linearly with concentration (as seen in the inset of Figure 2.8). This again confirmed the validity of the ribbon model. It was interesting to note that even for the suspension at relatively high concentration (e.g. 0.6 wt%), the ribbon model could still fit the experimental data pretty well. This indicated that the aggregation of nanofibers in the suspension was rare because of the strong repulsive electrostatic force between nanofibers.

From the conductimetric titration, the DO was determined to be 0.198, which suggested that 19.8% of the hydroxymethyl groups were oxidized into carboxylate groups. Given that for I_β cellulose, the inter-plane distances of $(1\bar{1}0)$ and (110) are 0.61 and 0.54 nm, respectively[16], the nanofiber with 12.7 nm width and 3.2 nm thickness will contain $(12.7 \times 3.2)/(0.61 \times 0.54) = 124$ cellulose chains. The number of chains on the surface of the nanofiber is $2 \times (12.7/0.54) + 2 \times (3.2/0.61) = 58$. However, since only half of the hydroxymethyl groups are accessible during the oxidation, it can be calculated that the maximum DO is $58 \times 0.5/124 = 0.234$. As the DO in this experiment is very close to the DO_{max}, one can conclude that almost all the hydroxymethyl groups were carboxylated. As a result, the nanofibers kept excellent dispersion in the suspension even at high concentration.

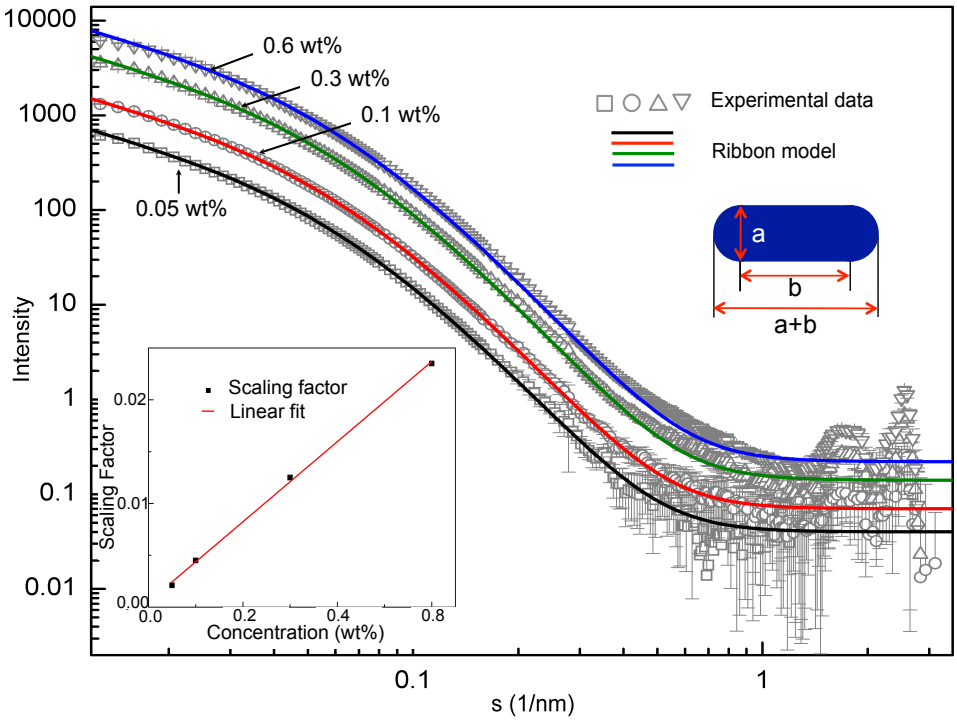

Figure 2.8 experimental patterns of Biofloc-96 cellulose nanofiber suspensions at four concentrations (0.05, 0.1, 0.3 and 0.6 wt%) and the fitting results using the ribbon model with size-weighted average parameters for the best fit were: $a_w = 3.2$ nm with standard deviation $\sigma_a = 2.2$ nm, $a_w + b_w = 12.7$ nm with standard deviation $\sigma_{a+b} = 5.5$ nm. The lower-left inset is the linear relation between the scaling factor of the model and the concentration of the suspension. The upper-right sketch shows the cross-section shape of the ribbon model.

Instead of number averages, the size-weighted averages of a, b and $(a+b)$ parameters derived from the ribbon model were adopted in the present study. In order to demonstrate the necessity of accepting this adoption, a comparison was made between the two sets of averages. The size-weighted average and number average a and b values of the same Gamma distribution that best fitted the scattering curve were substituted into the monodisperse ribbon model (Equation 2.11), respectively. The model with size-weighted average a and b was much closer to the best-fit polydisperse model and therefore fitted better to the experimental profile than the one using the number-average a and b (Figure 2.9).

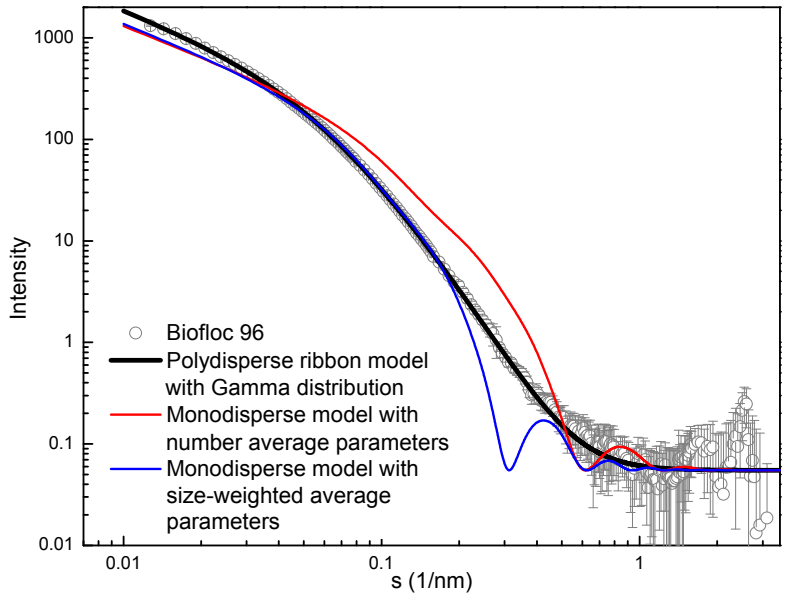

Figure 2.9 Comparison between the best fit polydisperse (Gamma distribution) model with size-weighted averages of a_w = 3.2 nm and b_w = 9.5 nm, and number averages of a_n = 1.6 nm and b_n = 6.9 nm, the monodisperse model with number average parameters (a = 1.6 nm and b = 6.9 nm), and the monodisperse model with size-weighted average parameters (a = 3.2 nm and b = 9.5 nm), respectively.

To be specific, in the low-s region (s ~ 0.01−0.04 nm^{-1}), the intensity profiles from the two monodisperse models overlapped each other. However, when s was larger than 0.04 nm^{-1}, the monodisperse ribbon model with size-weighted average parameters better fitted the experimental data, while the monodisperse ribbon model with number average parameters diverged notably from the experimental data as well as the polydisperse model. Furthermore, the tangents of the second and the third peak of the model with size-weighted average parameters coincided with the tangents of the polydisperse model at the contact points between the two curves, and the profile of the latter became an envelope to the peaks of the former. In contrast, for the model with number average parameters, the corresponding curve deviated from the polydisperse model in an erratic manner. The physical explanation to this phenomenon was that the scattering from a thicker fiber contributed more to the whole scattering than that from a

thinner one. Therefore, the size-weighted average parameters should be more appropriate to be taken in terms of the analysis to the scattering profile.

With the simplified ribbon model, the computational efficiency of the fitting using *Mathematica* was greatly improved compared to the original parallelepiped model. To be specific, the computing time needed to complete a Nonlinear Model Fit run by using a typical personal laptop computer (Apple MacBook Pro with 2.9 GHz Intel Core i7 processor and 8 GB 1600 MHz memory) was less than two minutes for the analytical expression of the polydisperse ribbon model, while it would take more than 20 hours to finish one run for the parallelepiped model with multiple integrals. The high calculation efficiency would promote the use of the ribbon model as a convenient tool in the analysis of scattering profiles for similar rod-like systems.

2.4.4 Comparison of SAXS Results and TEM Measurement

The dimensions of TEMPO-oxidized Biofloc-96 cellulose nanofibers determined from the SAXS analysis were also verified by the TEM study. Figure 2.10 illustrates the TEM images of TEMPO-oxidized cellulose nanofibers negatively stained by phosphotungstic acid (PTA). With the affinity to hydroxyl and carboxyl groups[17], the PTA was bound to the surface of the oxidized cellulose nanofibers, but left the crystalline core of the nanofibers unstained. The electron density difference between the stained region and the cellulose core resulted in the contrast of the TEM images, where cellulose nanofibers were white and the stained region was black.

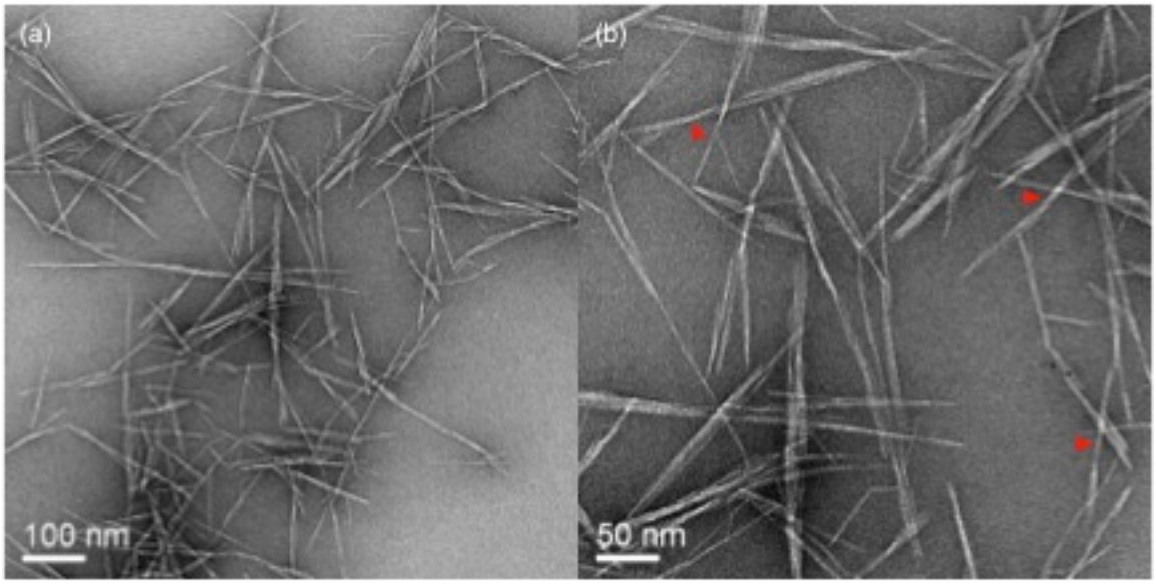

Figure 2.10 TEM images of Biofloc-96 cellulose nanofibers after TEMPO-mediated oxidation and disintegration treatments. The magnifications of (a) and (b) were 20,000× and 40,000×, respectively. The arrowheads in (b) marked the twisted nanofibers.

The widths of the cellulose nanofibers lying flat on the grid could be measured directly from the TEM images. For the twisting nanofibers (as marked in Figure 2.9(a)), the largest dimension perpendicular to the axis could also be measured as the width. With these two approaches, the width distribution based on a count of 227 cellulose nanofibers from 9 images is shown in Figure 2.11. The width results determined by the TEM method exhibited a remarkable similarity with the width results (i.e., $a+b$ in the ribbon model) extracted from the SAXS analysis using a Gamma distribution, where the comparison is illustrated in Figure 2.11. For further comparison, the number averages and size-weighted averages of the nanofiber widths determined from both the TEM measurements and the scattering analysis are listed in Table 2.2.

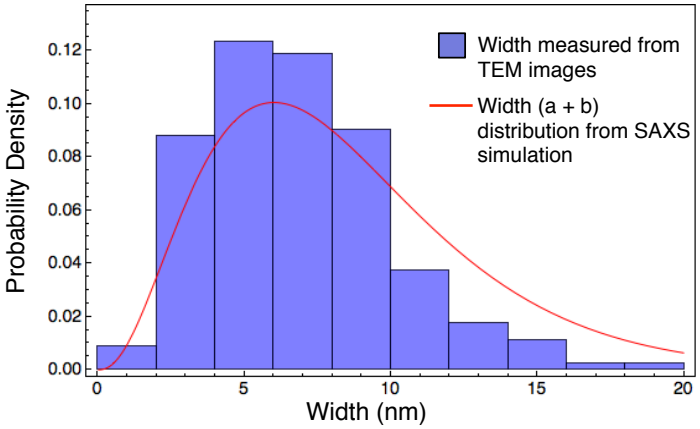

Figure 2.11 Width distributions from TEM image measurement (histogram) and SAXS analysis (red curve).

Table 2.2 Number average and size-weighted average widths of Biofloc96 cellulose nanofibers measured from TEM and SAXS.

	TEM	SAXS Analysis	
	Measurement (nm)	*b* (nm)	*a*+*b* (nm)
Number Average	6.8 ± 3.1	6.9 ± 4.3	8.6 ± 4.6
Size-weighted Average	8.2 ± 3.4	9.5 ± 5.0	12.7 ± 5.5

In Figure 2.11, the TEM histogram showed a positively skewed distribution with the largest probability locating in the range of 4−8 nm, coinciding with the profile of the Gamma distribution of (*a*+*b*) determined from the scattering analysis, except that the region larger than 10 nm where the TEM widths were significantly lower than the (*a*+*b*) distribution curve by SAXS. This resulted in the lower number average and size-weighted average of the measured TEM width than the corresponding average values of (*a*+*b*) obtained from SAXS (Table 2.2). Such a discrepancy could be explained by the distinguishing features of the two characterization methods: the electron microscopy provided direct visualization of nanostructures to a limited amount of particles, while X-ray scattering provided statistical analysis of the structural information from many particles in the system. In addition, since the molecular chains near the

surface of the nanofibers were not well ordered[18], they could be permeable to and positively stained by PTA[19]. In this case, the widths of the white nanofibers measured in the TEM images should actually be smaller than the true widths of cellulose nanofibers, which, to some extent, resulted in the difference between the TEM results and the SAXS results.

From the TEM images (Figure 2.10), it can be seen that most of the Biofloc-96 cellulose nanofibers were further composed of two to four microfibrils. In other words, the nanofibers prepared from the dried bleached pulp were small bundles of microfibrils instead of individual microfibrils. This is because during the pulping and bleaching processes, the lignin separating individual cellulose microfibrils in the cell wall was eliminated; during the followed drying process, the microfibrils directly connected to each other and formed side-by-side bundles through hydrogen bonds. Once formed, these bundles were hard to be broken into microfibrils during the oxidation and the homogenization treatments.

2.4.5 Comparison of Cellulose Nanofibers from Different Biological Species

Besides the Biofloc-96 sample from maritime pine wood pulp, the TEMPO-oxidized cellulose nanofiber samples prepared from other biological species, i.e. spruce wood pulp, cotton pulp, bamboo pulp and jute fibers, were also characterized by solution SAXS and TEM. It can be seen from Figure 2.12 that the polydisperse ribbon model developed for the Biofloc-96 sample can also fit the other four samples with different parameters in the model. The size-weighted average dimensions are shown in the inset of Figure 2.12, and the detailed parameters of the ribbon model used for the fitting of the four samples are listed in Table 2.3.

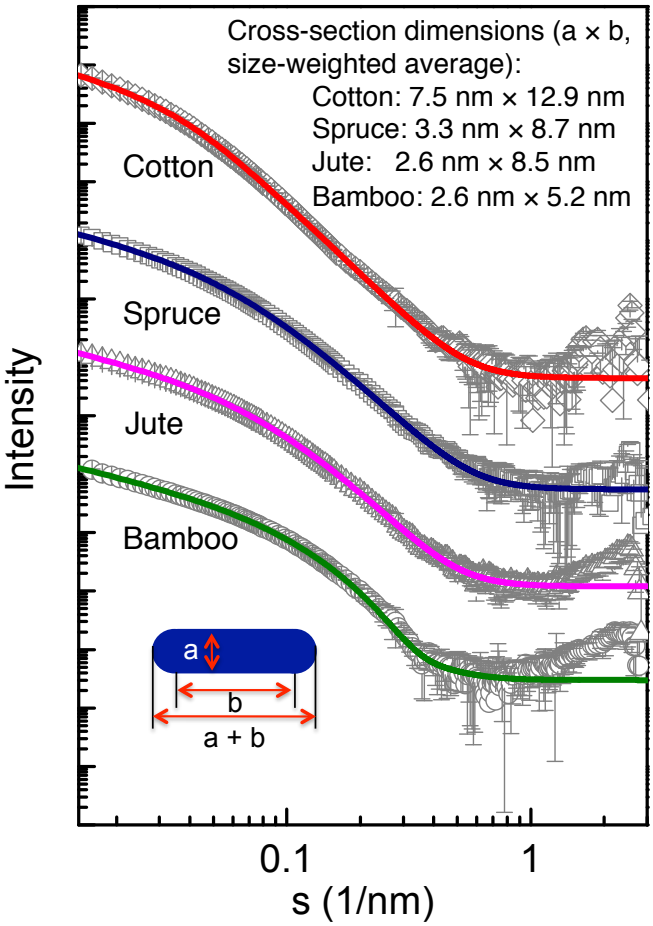

Figure 2.12 Comparison of the polydisperse ribbon model with simultaneous SAXS/WAXD patterns from bamboo, jute, spruce and cotton suspensions at concentration 0.1 wt%, respectively. The curves were manually shifted vertically for visual clarity. Only the small-angle region ($s \sim 0.01 - 1$ nm^{-1}) was simulated in this study, because the wide-angle region signal ($s > 1$ nm^{-1}) of the diluted suspension was too weak. The lower-left inset shows the cross-section dimensions of the ribbon model, and the upper-right insert lists the size-weighted average width and thickness of each sample calculated from the ribbon model.

As the experimental conditions of the TEMPO-mediated oxidation and the mechanical homogenization were remained the same for the treatments of the four samples, the cross-section dimensions calculated from the model fitting of SAXS patterns indicated that the cross-section sizes of bamboo cellulose nanofibers were the smallest and cotton cellulose nanofibers were the largest, which were about 2 times thicker and 1.5 times wider than the bamboo nanofibers. The cross-section dimensions of jute nanofibers and spruce nanofibers were similar to each other. The standard deviations of the dimensions were pretty large for all the four samples, accounting

for about 30−65 % of the average values, indicating that the nanofiber suspensions were heavily polydisperse systems.

Table 2.3 Size-weighted average parameters and corresponding standard deviations of the ribbon model fitting different samples

	Size-weighted averages (nm)	Standard deviations (nm)
Bamboo	$a_w = 2.6$ $b_w = 5.2$ $a_w + b_w = 7.8$	$\sigma_a = 0.8$ $\sigma_b = 2.4$ $\sigma_a + \sigma_b = 2.6$
Jute	$a_w = 2.6$ $b_w = 8.5$ $a_w + b_w = 11.1$	$\sigma_a = 1.6$ $\sigma_b = 4.0$ $\sigma_a + \sigma_b = 4.3$
Spruce	$a_w = 3.3$ $b_w = 8.7$ $a_w + b_w = 12.0$	$\sigma_a = 2.1$ $\sigma_b = 6.4$ $\sigma_a + \sigma_b = 7.6$
Cotton	$a_w = 7.5$ $b_w = 12.9$ $a_w + b_w = 20.4$	$\sigma_a = 4.9$ $\sigma_b = 4.2$ $\sigma_a + \sigma_b = 6.5$

The TEM images of bamboo, spruce and cotton cellulose nanofibers are shown in Figure 2.13, and the fiber widths of these three samples measured from the TEM images were comparable with the values calculated from the SAXS analysis. It is obvious that there are even finer structures inside each nanofiber, implying that those nanofibers were composed of even thinner fibrils, i.e. cellulose microfibrils. In addition, it could be seen from the images that the lengths of cotton naofibers were around or below 200 nm, while the length of both bamboo and spruce nanofibers were about 300−500 nm. Since it is known that cellulose microfibrils are composed of alternate crystalline and amorphous segments along the fiber length, and the longitudinal break of cellulose microfibrils tends to occur at the weak amorphous part in the homogenization process, it can be speculated that the length of the crystalline segments in cotton microfibrils should be shorter than that in wood or bamboo microfibrils.

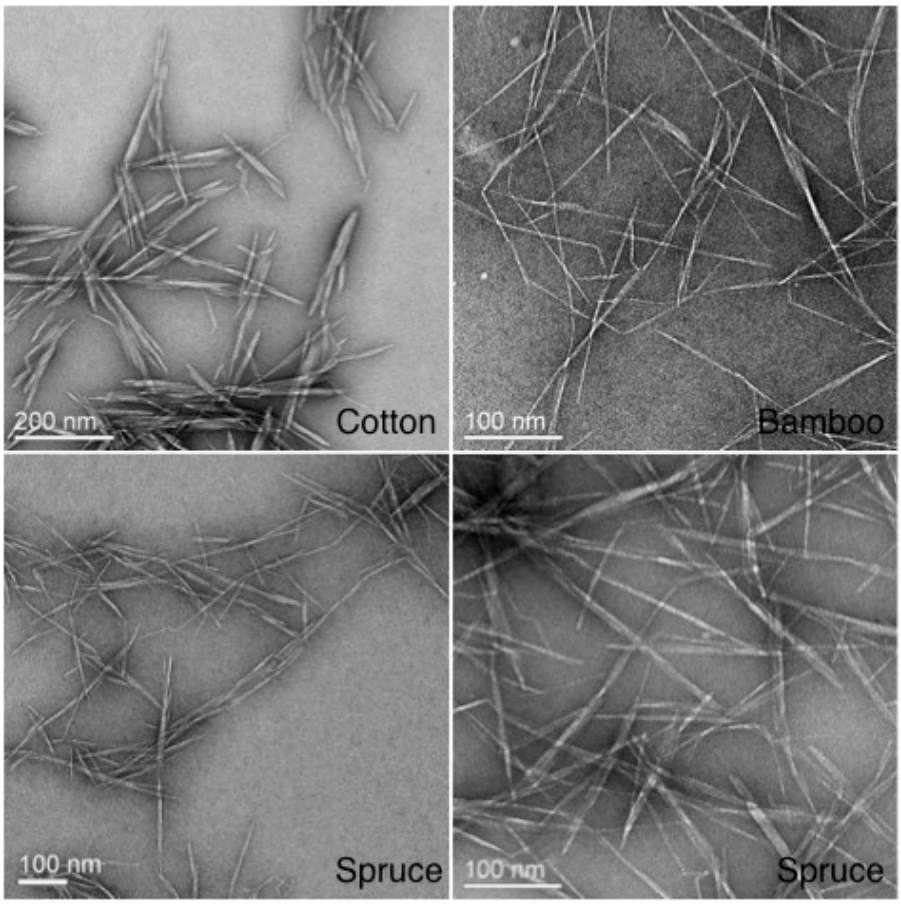

Figure 2.13n TEM images of cotton, bamboo and spruce cellulose nanofibers after TEMPO-mediated oxidation and disintegration treatments. Both the bottom two images were taken from the same spruce nanofiber sample but at different magnification.

2.4.6 Effect of Experimental Conditions on the Morphology of Nanofibers

Three experimental variables (i.e. dose of NaClO used for oxidation, oxidation time and homogenization time) were examined to study the influence of these experimental conditions on the morphology and degree of oxidation (DO) of cellulose nanofibers. The specific experimental parameters are listed in Table 2.1 in section 2.2.

Table 2.4 lists the SAXS-determined cross-section dimensions of the TEMALFA samples treated under different experimental conditions. It can be seen that by changing the ratios between NaClO and cellulose from 5 to 12 mmol/g, the thickness as well as its standard deviation increased along with the increasing ratio, while the width and its standard deviation

generally followed a decreasing trend along with the increase in the NaClO/cellulose ratio, indicating that the thickness range expanded with more NaClO used in the oxidation and the width tended to be more uniform.

Regarding the effect of the oxidation reaction time, comparing the dimensions of nanofiber samples with reaction time of 2, 4, 7, 24 and 48 hours, respectively, it can be concluded that similar to the NaClO/cellulose ratio effect, extended oxidation time led to a broader thickness range but a smaller width with anarrower width range. As for the effect of the homogenization time, it is obvious that both the width and the thickness averages decreased with longer homogenizing time, and both size ranges tended to get narrower.

Table 2.4 Size-weighted average parameters and corresponding standard deviations of the ribbon model fitting TEMALFA-spruce samples obtained under different experimental conditions

	Size-weighted averages (nm)	Standard deviations (nm)
TEMALFA-RO5	$a_w = 2.8$ $b_w = 9.1$ $a_w + b_w = 11.9$	$\sigma_a = 1.3$ $\sigma_b = 8.1$ $\sigma_a + \sigma_b = 8.7$
TEMALFA-RO9	$a_w = 3.1$ $b_w = 8.2$ $a_w + b_w = 11.3$	$\sigma_a = 1.6$ $\sigma_b = 6.4$ $\sigma_a + \sigma_b = 7.4$
TEMALFA-RO12	$a_w = 3.3$ $b_w = 8.7$ $a_w + b_w = 12.0$	$\sigma_a = 2.1$ $\sigma_b = 6.4$ $\sigma_a + \sigma_b = 7.6$
TEMALFA-TM2	$a_w = 3.2$ $b_w = 10.9$ $a_w + b_w = 14.1$	$\sigma_a = 1.8$ $\sigma_b = 7.7$ $\sigma_a + \sigma_b = 8.5$
TEMALFA-TM4	$a_w = 3.2$ $b_w = 10.9$ $a_w + b_w = 14.1$	$\sigma_a = 1.9$ $\sigma_b = 8.3$ $\sigma_a + \sigma_b = 9.4$
TEMALFA-TM7	$a_w = 3.2$ $b_w = 9.8$ $a_w + b_w = 13.0$	$\sigma_a = 2.0$ $\sigma_b = 7.3$ $\sigma_a + \sigma_b = 8.4$
TEMALFA-TM24	$a_w = 3.3$ $b_w = 8.7$ $a_w + b_w = 12.0$	$\sigma_a = 2.1$ $\sigma_b = 6.4$ $\sigma_a + \sigma_b = 7.6$
TEMALFA-TM48	$a_w = 3.4$ $b_w = 9.4$ $a_w + b_w = 12.8$	$\sigma_a = 2.2$ $\sigma_b = 6.7$ $\sigma_a + \sigma_b = 7.9$
TEMALFA-HM2	$a_w = 3.2$ $b_w = 10.4$ $a_w + b_w = 13.6$	$\sigma_a = 1.9$ $\sigma_b = 8.2$ $\sigma_a + \sigma_b = 9.2$
TEMALFA-HM10	$a_w = 3.1$ $b_w = 8.2$ $a_w + b_w = 11.3$	$\sigma_a = 1.6$ $\sigma_b = 6.4$ $\sigma_a + \sigma_b = 7.4$
TEMALFA-HM15	$a_w = 3.0$ $b_w = 8.6$ $a_w + b_w = 11.6$	$\sigma_a = 1.5$ $\sigma_b = 5.4$ $\sigma_a + \sigma_b = 6.0$

In addition to the dimension characterization, the effects of NaClO/cellulose ratio and reaction time on DO were also investigated. As shown in Figure 2.14, with other experimental parameters remaining the same, the DO increased from 6.2% (ratio of oxidized hydroxymethyl groups over total hydroxymethyl groups) at the NaClO/cellulose ratio of 0.83 mmol/g to 14.8% at the NaClO/cellulose ratio of 5 mmol/g, and then the DO remained at 16.3% when the NaClO/cellulose ratio increased to 9 and 12 mmol/g. Figure 2.15 shows the DO variation trends upon reaction time for the samples with NaClO/cellulose ratios of 5 and 12 mmol/g, respectively. For both samples, the DO could reach 14.8% within 2 hours after the initialization of the oxidation, and then the DO fluctuated between 14.8% and 16.3% along with extended oxidation time, which was up to 48 h.

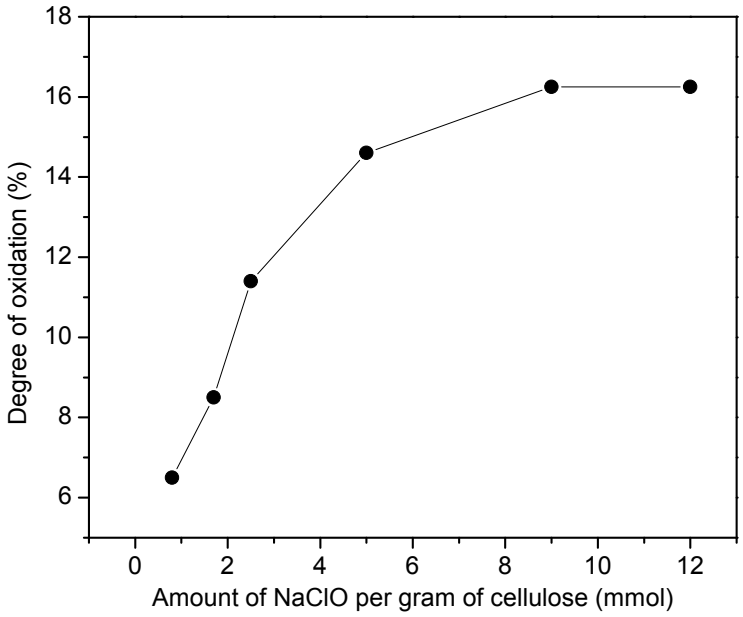

Figure 2.14 Relationship between DO and amount of NaClO used in the oxidation for TEMALFA-RO samples.

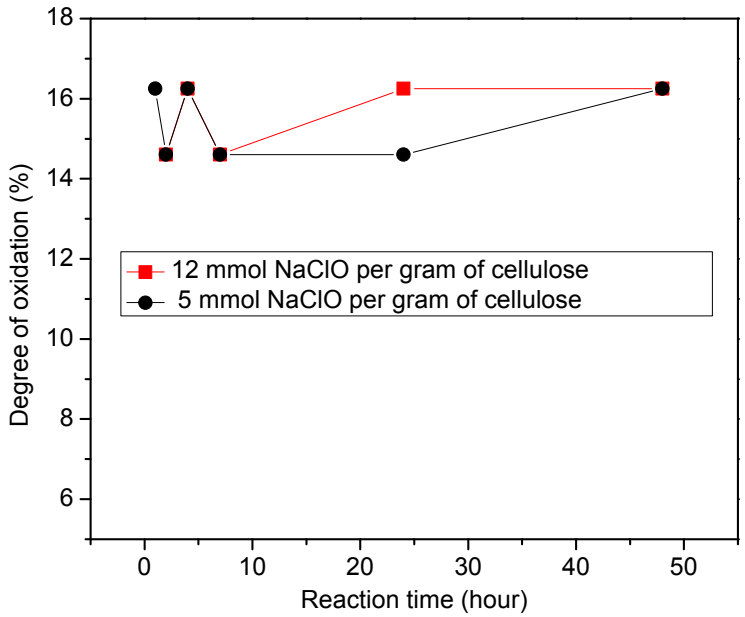

Figure 2.15 Relationship between DO and reaction time of the oxidation for TEMALFA samples, adopting 5 and 12 mmol NaClO per gram of cellulose, respectively.

Adding together the facts that extended oxidation time reduced the width of the nanofibers and confined the DO fluctuating between two fixed numbers, it can be speculated that when the oxidant attacked the surface molecular chains of the nanofibers, the outermost layer on the two small side surfaces could break up and get dissolved in water after long time oxidation, leaving the second outermost layer exposed in the oxidizing environment. Along with the cyclic exfoliation of the outermost layers, the width got smaller, and since the dissolved molecules or small fractions were washed out after the oxidation and before the homogenization process, the DO could be fluctuating depending on whether the outermost layer had already been oxidized when the reaction was terminated.

2.5 Conclusions

Cellulose nanofibers were extracted from dried wood/cotton/bamboo pulps and jute raw fibers through TEMPO-mediated oxidation followed by mechanical homogenization. The solution small-angle X-ray scattering (SAXS) method was used to investigate the size and size

distribution of cellulose nanofibers in suspension. A simplified ribbon model with Gamma distribution, superior to the cylinder model, was found to be able to fit the scattering profiles at multiple concentrations and over a large angular range with high quality and computing efficiency. For the chosen Biofloc-96 cellulose system, the nanofibers possessed a ribbon shape with the size-weighted average thickness and width of 3.2 nm and 12.7 nm, respectively. The Gamma distribution of the ribbon width determined by SAXS was in substantial agreement with the histogram of nanofiber width measured from the TEM images, demonstrating the validity and reliability of the simplified ribbon model.

Through studying the effects of NaClO/cellulose ratio, reaction time and homogenization time on the morphology and DO of cellulose nanofibers, it was found that higher NaClO/cellulose ratio or longer reaction time tended to reduce the average widths of nanofibers but also expand the size distribution of the thickness. The longer homogenization time attributed to smaller and more uniform sizes of nanofibers. When the NaClO/cellulose ratio was 5 mmol/g or above, the DO would reach a maximum of 16.3% and would not increase with the increasing NaClO/cellulose ratio. During the oxidation process, the DO could reach its maximum within 1 hour, after which the DO of nanofibers fluctuated within a small range (14.8–16.3%). It is believed that this phenomenon could be caused by the exfoliation of the oxidized outermost layer molecules on the side surfaces of nanofibers during oxidation.

References

(1) Pokhrel, D.; Viraraghavan, T. *Sci Total Environ* **2004**, *333*, 37.

(2) Biermann, C. J. *Essentials of pulping and papermaking*; Academic Press, 1993.

(3) Gibbons, J. H. *Technologies for reducing dioxin in the manufacture of bleached wood pulp*; DIANE Publishing: Washington, DC, 1989.

(4) Habibi, Y.; Chanzy, H.; Vignon, M. R. *Cellulose* **2006**, *13*, 679.

(5) Allaire, M.; Yang, L. *J Synchrotron Radiat* **2011**, *18*, 41.

(6) Pedersen, J. S. *Adv Colloid Interfac* **1997**, *70*, 171.

(7) Suzuki, H.; Kamiyama, T. *J Wood Sci* **2004**, *50*, 351.

(8) Jakob, H. F.; Fratzl, P.; Tschegg, S. E. *J Struct Biol* **1994**, *113*, 13.

(9) Leppanen, K.; Andersson, S.; Torkkeli, M.; Knaapila, M.; Kotelnikova, N.; Serimaa, R. *Cellulose* **2009**, *16*, 999.

(10) Jakob, H. F.; Fengel, D.; Tschegg, S. E.; Fratzl, P. *Macromolecules* **1995**, *28*, 8782.

(11) Guinier, A.; Fournet, G. *Small-angle Scattering of X-rays*; Jone Wiley & Sons, Inc.: New York, NY, 1955.

(12) Ma, H. Y.; Burger, C.; Hsiao, B. S.; Chu, B. *Biomacromolecules* **2011**, *12*, 970.

(13) Porod, G. In *Small Angle X-ray Scattering*; Glatter, O., Kratky, O., Eds.; Academic Press Inc.: London, UK, 1982, p 32.

(14) Wolfram Research Inc. *Mathematica Edition: Version 8.0*; Wolfram Research, Inc.: Champaign, Illinois, 2010.

(15) Akaike, H. *Ieee T Automat Contr* **1974**, *Ac19*, 716.

(16) Sugiyama, J.; Vuong, R.; Chanzy, H. *Macromolecules* **1991**, *24*, 4168.

(17) Sawyer, L. C.; Grubb, D. T.; Meyers, G. F. *Polymer Microscopy*; 3rd ed.; Springer Science+Business Media, LLC: New York, NY, 2008.

(18) Fernandes, A. N.; Thomas, L. H.; Altaner, C. M.; Callow, P.; Forsyth, V. T.; Apperley, D. C.; Kennedy, C. J.; Jarvis, M. C. *P Natl Acad Sci USA* **2011**, *108*, E1195.

(19) Colvin, J. R. *The Journal of Cell Biology* **1963**, *17*, 105.

Chapter 3 Cellulose Nanostrips Extracted from Raw Wood Powder

3.1 Introduction

As introduced in Chapter 2, cellulose microfibrils in dried wood pulps after the pulping and bleaching processes tend to aggregate into bundles, and it is difficult to separate the individual microfibrils from each other even under prolonged oxidation with high NaClO/cellulose ratio and high-power mechanical fibrillation treatments. This is believed to be caused by the loss of accessibility and reactivity of cellulose microfibrils[1] in the delignification process.

Cellulose nanofibers extracted from never-dried wood pulp through TEMPO-mediated oxidation method exhibited a regular width of 3-4 nm[2], which were considered as individual microfibrils. Cellulose microfibril fractions with thicknesses below 1 nm have also been reported, indicating the delamination of cellulose microfibrils through the TEMPO-mediated oxidation and sonication fibrillation[3].

The work elaborated in this chapter further explored the inner structure of cellulose microfibrils by studying their oxidation and delamination process. Specifically, thin cellulose "nanostrips" were prepared from raw spruce wood powder through TEMPO-mediated oxidation and successive mechanical homogenization treatments. The dimensions of individual nanostrips in aqueous suspension were characterized by solution small-angle X-ray scattering (SAXS). Moreover, wide-angle X-ray diffraction (WAXD), TEM, AFM and solid ^{13}C NMR were performed to confirm and supplement the structural information obtained from the SAXS analysis. A possible delamination mechanism of cellulose microfibrils has been proposed, which was consistent with the generally accepted biological synthesis and assembly hypothesis of cellulose microfibrils in plant cell wall.

3.2 Materials and Methods

3.2.1 Materials

The Jezo spruce (Picea jezoensis) wood powder with particle size larger than 80-mesh was provided as a gift from Professor. Isogai and Saito group. Sodium chlorite ($NaClO_2$), acetone, sodium hydroxide (NaOH), hydrochloric acid, 2,2,6,6-tetramethyl-1- piperidinyloxy (TEMPO), sodium hypochlorite (NaClO), sodium bromide (NaBr) were purchased from Sigma-Aldrich.

3.2.2 Delignification

The Jezo spruce wood powder with particle sizes larger than 80-mesh was soaked in 90% (v/v) acetone aqueous solution for 1 day under stirring condition using a magnetic stirrer at stirring rate of 600 rpm to remove extractives (such as triglycerides, resin acides, etc.). Then the wood powder was washed with acetone and separated by vacuum filtration. Subsequently, delignification was performed following the Wise method[4]. To be specific, the vacuum dried wood powder was repeatedly treated in 1% (w/v) $NaClO_2$ buffer solution (with acetic acid added to keep pH around 5) and heated at temperatures 60-70 °C for 1 h with stirring. The process was repeated for 8-12 times until the color of the wood powder became white. After soaking in HCl solution at pH = 2 for 1 hour to remove any metal ions, the wood powder was washed with deionized (DI) water for 5 times and stored in never-dried state for further use.

3.2.3 TEMPO-mediated Oxidation

Similar to the oxidation process described in section 2.2.2., the wood powder (1.0 g) was first suspended in water (90 mL), and then sodium bromide (0.10 g) and the TEMPO agent (0.02 g) were dissolved in the suspension. A desired amount of 1.5 mol/L of sodium hypochlorite

solution (8 mmol per gram of cellulose) was added to initiate the oxidation process and the reaction was stirred mechanically in a sealed bottle for 24 h. The pH of the suspension was maintained between 9.8 and 10.3 during the reaction (monitored with a pH meter) by adding sodium hydroxide aqueous solution (1 mol/L). The oxidized cellulose suspension was dialyzed with dialysis tubing (MWCO 10000 DA) in DI water until the pH reached 6.5.

10 mL of the oxidized cellulose suspension was diluted to 130 mL with DI water and disintegrated with a homogenizer (Cole Parmer, VCX-400) at the output power of 79 % (60 Hz, 115 W) in an ice bath for 10 min. After homogenization, the suspension was centrifuged at 4700 *g* for 20 min and the supernatant was collected. The final concentration of the cellulose nanostrip suspension was 0.077 wt%, which was determined by using a total organic carbon (TOC) analyzer.

3.2.4 Determination of Degree of Oxidation (DO)

Similar to the description in section 2.2.3., the ratio between the amount of oxidized and total hydroxymethyl groups in the oxidized cellulose was determined via the conductometric titration method[5]. Briefly, 0.1 mol/L of hydrochloric acid aqueous solution was dropped to 24 mL of cellulose nanostrip suspension at an initial concentration of 0.05 wt% until the pH value reached 2.8. The suspension was titrated with 0.005 mol/L NaOH solution under vigorous stirring (450 rpm). The conductivity of the suspension was monitored by using a conductivity meter throughout the titration process. The titration performance was terminated when the pH reached 10.7. The curve of conductivity versus volume of NaOH solution used was plotted, and the volume of NaOH aqueous solutions used to neutralize the carboxyl groups, V, was determined from the curve. The amount of oxidized hydroxymethyl groups was calculated by multiplying V with the concentration, C, of the NaOH solution, while the amount of cellulose

was directly measured from the TOC analyzer.

3.2.5 Synchrotron Solution SAXS/WAXD

As described in section 2.2.4, simultaneous SAXS/WAXD measurements of cellulose nanostrip suspensions were carried out at Beamline X9 of the National Synchrotron Light Source (NSLS), Brookhaven National Laboratory (BNL), USA. Two samples with concentrations, 0.077 wt% and 0.15 wt%, of the suspension were used for the investigation. In a scanning process, 20 μL suspension was pumped into a glass capillary (diameter of 1 mm) sealed across the vacuum path. The sample was allowed to flow continuously through the capillary during data collection in order to minimize radiation damage[6]. The X-ray wavelength at Beamline X9 was 0.0918 nm. A PILATUS 300 K detector located 3.2 m away from the sample was used to collect the SAXS data. A custom-designed Photonic Science CCD detector, 463 mm from the sample, took the 2D WAXD patterns. For each sample, three 30-second scans were taken. The average of these three scans was used as the scattering pattern of the sample. A silver behenate standard was used to calibrate the parameters of the scattering geometry (i.e. beam center and sample-to-detector distance). Preliminary data processing was done with a Python-based package developed at the X9 Beamline to convert the two-dimensional (2D) images into one-dimensional (1D) scattering profiles, block off dead pixels and pixels behind the beam-stop, merge SAXS and WAXD scans, and subtract the buffer and capillary background from the scattering profile. In this study, only the profile in small-angle region ($s < 1$ nm^{-1}) was simulated, and the analysis of the wide-angle part was not involved here. The model development and model fitting of the SAXS data was performed using the softwate *Mathematica*[7].

3.2.6 Synchrotron WAXD of Dry Samples

Three samples including freeze-dried spruce wood powder after delignification treatment

(WPDL), freeze-dried sample after TEMPO-mediated oxidation (WPTO) and freeze-dried sample after mechanical homogenization (WPMH) were measured, respectively, using WAXD at Beamline X27C of NSLS, BNL. The X-ray wavelength was 0.1371 nm, the exposure time for each sample was 60 s, and the 2D WAXD patterns were acquired using a MAR-CCD detector. The Al_2O_3 standard was used to calibrate the sample-to-detector distance. The diffraction data analysis, including background subtraction and conversion from 2D images to 1D profiles was performed using the software XPolar (Stonybrook Technology and Applied Research, Stony Brook, New York).

3.2.7 TEM & AFM

Similar to the TEM sample preparation described in section 2.2.5, the TEM samples were prepared by dropping the cellulose nanostrip suspension (~10 μL, 0.077 wt%) onto a carbon-film-coated copper grid (300 mesh). The suspension was allowed to stay on the grid for 3 min and then the excess liquid was drawn off the grid using a filter paper. Before drying, 5 μL of 1.5 wt% phosphotungstic acid (PTA) aqueous solution was dropped on the top of the grid and left for 30 s before being absorbed by filter paper. This staining step was repeated once more and the stained sample was kept in air until completely dry and then stored in a desiccator before use. The TEM observations were performed at the Center for Functional Nanomaterials (CFN) at BNL using a JEOL JEM-1400 microscope (JEOL, Tokyo, Japan) equipped with a CCD camera (ORIUS SC200, Gatan Inc., USA) operated at 100 kV.

For the AFM measurement, 0.0015 wt% cellulose nanostrip suspension was spin-coated onto a freshly cleaved mica substrate, and the measurement was performed at the Advanced Energy Research and Technology Center (AERTC), Stony Brook University, by using a Bruker

Dimension ICON scanning probe microscope (Bruker Corporation, USA) equipped with a Bruker OTESPA tip (radius 7 nm) in the tapping mode.

3.2.8 Solid-state CP-MASS ^{13}C NMR

Solid-state ^{13}C NMR spectra of four samples, i.e. original wood powder without any treatment (original), freeze-dried sample after delignification (WPDL), freeze-dried sample after TEMPO-mediated oxidation (WPTO) and freeze-dried sample after mechanical homogenization (WPMH), were obtained from a Bruker 600 MHz wide-bore solid-state NMR spectrometer with cross-polarization magic angle sample spinning. The spinning speed was 12 kHz, the pulse delay was 5 s and the contact time was 1 ms. Peak assignments were based on previous reports[8-10] and spectral fitting in the region between 40 and 200 ppm was performed based on the peak de-convolution method of cellulose samples[11].

3.3 Model Development for Solution SAXS Analysis

3.3.1 Derivation of Nanostrip Model

For diluted suspensions, it is assumed that the interaction between particles is very weak and can therefore be ignored. As a result, the scattering intensity is dominated by the form factor $|F(s)|^2$, where $F(s)$ is the amplitude of the scattering, and mathematically it is the Fourier transform of the electron density distribution in the particle.

Since the lengths of cellulose nanostrips are around 1 μm, which are much larger than the cross-section width (~4 nm) as well as the size range (0.5–100 nm) that SAXS investigates, the length L is considered to be infinitely long. As a result, the contribution of the length of the nanostrips to the scattering intensity distribution is $\frac{L}{2s}$, as explained in section 2.3.

In simulating the electron density distribution of a monolayer of glucan chains for the nanostrip model, based on the fact that the carbon and nitrogen atoms locate interiorly in the nanostrips compared to the hydrogen atoms, the electron density in the center of the nanostrip should be higher than that of the edge. Therefore, it is reasonable to assume a Gaussian distribution of the electron density across the thickness of the cross-section, while we assume the electron density along the width direction is uniform. Mathematically, such an electron density distribution of the cross-section can be considered as the convolution of a line segment with electron density increasing from both ends to the center following a Gaussian distribution with integral width *d* along another line segment perpendicular to the former one and with length *b*. Eventually, the cross-section is in rectangular shape with uniform electron density distribution along the width and a Gaussian distribution of electron density across the thickness.

As the Fourier transform of a convolution is equivalent to the product of the Fourier transforms of each function involved in the convolution ($\mathcal{F}\{f * g\} = \mathcal{F}\{f\} \cdot \mathcal{F}\{g\}$), the amplitude of scattering from the nanostrip cross-section is therefore the product of the Fourier transforms of the electron density distributions along width and thickness, respectively. The Gaussian distribution of electron density across the thickness can be expressed as:

$$f(x) = \frac{1}{d}\exp\left(-\frac{\pi x^2}{d^2}\right) \qquad \text{Eq. 3.1}$$

where *x* is the distance from any point on the segment to the middle point, and *d* is the integral width of the Gaussian distribution. The 1D Fourier transform of *f*(*x*) is:

$$F_d(s) = \mathcal{F}_1\{f(x)\} = \int_{-\infty}^{+\infty} \frac{1}{d}\exp\left(-\frac{\pi x^2}{d^2}\right)\exp(-2\pi \mathrm{i} x s)dx = \exp(-\pi d^2 s^2) \qquad \text{Eq. 3.2}$$

For the width direction, the segment with length *b* can be expressed with a square-well function:

$$\Pi(y)=\begin{cases} 0, |y|>\dfrac{b}{2} \\ 1, |y|\le\dfrac{b}{2} \end{cases} \qquad \text{Eq. 3.3}$$

where y is the distance between any point on the segment along width to the middle of the segment, and b is the length of the segment. The 1D Fourier transform of Equation 3.3 is:

$$F_b(s)=\mathcal{F}_1\{\Pi(y)\}=\int_{-b/2}^{+b/2}\exp(-2\pi isy)dy=b\frac{\sin(\pi bs)}{\pi bs} \qquad \text{Eq. 3.4}$$

Since the direction of the segment is random in the cross-section plane, the form factor $F_b^2(s)$ needs to be averaged over all possible orientations in the plane:

$$\left\langle F_b^2(s)\right\rangle_\psi=\frac{b^2}{2\pi}\int_0^{2\pi}\left[\frac{\sin(\pi sb\sin\psi)}{\pi sb\sin\psi}\right]^2 d\psi=b^2\,{}_1\mathrm{F}_2\left(\frac{1}{2};\frac{3}{2},2;-\pi^2s^2b^2\right) \qquad \text{Eq. 3.5}$$

where ψ is the azimuthal angle. Therefore, the form factor of the cross-section is:

$$F_d^2(s)\left\langle F_b^2(s)\right\rangle_\psi=b^2\exp(-2\pi d^2s^2)\,{}_1\mathrm{F}_2\left(\frac{1}{2};\frac{3}{2},2;-\pi^2s^2b^2\right) \qquad \text{Eq. 3.6}$$

Finally, by taking the scattering contribution from the length of the nanostrips into consideration, the intensity distribution function of the nanostrip model should be:

$$I(s)=\frac{b^2L}{2s}\exp(-2\pi d^2s^2)\,{}_1\mathrm{F}_2\left(\frac{1}{2};\frac{3}{2},2;-\pi^2s^2b^2\right) \qquad \text{Eq. 3.7}$$

3.3.2 Derivation of "1D Paracrystalline" Model

The "1D paracrystalline" model describes a scenario that nanostrips stack up to form a multilayer structure with one's top surface facing another's bottom surface. For the system with interactions between particles, the scattering intensity is related to both the structure factor and the form factor of each building block:

$$I(s)=\left|F(s)\right|^2S(s) \qquad \text{Eq. 3.8}$$

Since the form factor has been solved in the nanostrip model, now we just need to determine the structure factor, which comes from the stacking of nanostrips.

For the "1D paracrystalline" model, it is assumed that n nanostrips are parallel placed at n points distributed in a line with inter-position distance r, which is polydisperse, and the height of the stack is finite. Then the autocorrelation function ($g(r)$) of the n lattice points is:

$$g(r) = n\delta(p) + \sum_{m=1}^{n-1} ih^{n-m}(r) + \sum_{m=1}^{n-1} ih^{n-m}(-r) \qquad \text{Eq. 3.9}$$

where r is the interlayer distance between any two adjacent layers, p is the position at any point in the system relative to the origin, n is the number of layers in the stack, $\delta(p)$ is the delta function with the expression of $\delta(p) = \begin{cases} 1, p = p_m \\ 0, p \neq p_m \end{cases}$; p_m is the position where a layer is located, $h(r)$ is the probability distribution function of the interlayer distance r. In this model, $h(r)$ is a Gaussian distribution with average a_0 and standard deviation σ_a.

Since the scattering intensity is the Fourier transform of the correlation function, the following equation is derived:

$$\mathcal{F}_1\{g(r)\} = n + 2\,\mathrm{Re}\left[\sum_{m=1}^{n-1} ih^{n-m}(s)\right] \qquad \text{Eq. 3.10}$$

where n is the number of layers in the stack, and $h(s)$ is a Gaussian distribution in reciprocal space with the expression of $h(s) = \exp\left(-2\pi i a_0 s - 2\pi^2 \sigma_a^2 s^2\right)$, because the Fourier transform of a Gaussian distribution is still a Gaussian distribution. Normalizing the intensity to a single layer, we have:

$$S(s) = 1 + 2\,\mathrm{Re}\left[\sum_{m=1}^{n-1} \frac{i}{n} h^{n-m}(s)\right] = -1 + 2\,\mathrm{Re}\left[\sum_{k=0}^{n-1} \left(1 - \frac{k}{n}\right) h^{k}(s)\right] \qquad \text{Eq. 3.11}$$

Furthermore, we assume that the number of layers in each stack is polydisperse and follows an exponential distribution with average n_0, and at this point, the structure factor of the "1D paracrystalline" model can be expressed as:

$$S(s) = -1 + 2\,\mathrm{Re}\left[\sum_{k=0}^{n-1}\left(1-\frac{k}{n}\right)h^k(s)\right] \approx -1 + 2\,\mathrm{Re}\left[\sum_{k=0}^{\infty}\exp\left(-\frac{k}{n_0}\right)h^k(s)\right] \quad \text{Eq. 3.12}$$

Mathematically, Equation 3.12 can be further simplified into:

$$S(s) = -1 + 2\,\mathrm{Re}\left[\frac{1}{1-h(s)\exp\left(-\frac{2}{n_0}\right)}\right] = -1 + 2\,\mathrm{Re}\left[\frac{1}{1-\exp\left(-2\pi i a_0 s - 2\pi^2\sigma_a^2 s^2 - \frac{2}{n_0}\right)}\right] \quad \text{Eq. 3.13}$$

To calculate the scattering intensity, we need to include the form factor of the nanostrip derived from the nanostrip model into the function:

$$I(s) = \frac{L}{2s}\exp(-2\pi d^2 s^2)\left(b\frac{\sin(\pi bs)}{\pi bs}\right)^2\left(-1 + 2\,\mathrm{Re}\left[\frac{1}{1-\exp\left(-2\pi i a_0 s - 2\pi^2\sigma_a^2 s^2 - \frac{2}{n_0}\right)}\right]\right) \quad \text{Eq. 3.14}$$

The above function is the scattering intensity attributed from a single nanostrip in the stacking structure, and it counts only one fixed direction. The final intensity should be the average intensity over all possible orientations in the cross-section plane:

$$I(s) = \frac{L}{2s}\exp(-2\pi d^2 s^2)\int_0^{\pi/2}\left(b\frac{\sin(\pi bs\sin\psi)}{\pi bs\sin\psi}\right)^2\left(-1 + 2\,\mathrm{Re}\left[\frac{1}{1-\exp\left(-2\pi i a_0 s\cos\psi - 2\pi^2\sigma_a^2 s^2\cos^2\psi - \frac{2}{n_0}\right)}\right]\right)d\psi \quad \text{Eq. 3.15}$$

which can be further simplified into:

$$I(s) = f\frac{\exp(-2\pi d^2 s^2)}{s}\int_0^{\pi/2}\frac{3b^2}{3+\pi^2 b^2 s^2\sin^2\psi}\left(-1 + 2\,\mathrm{Re}\left[\frac{1}{1-\exp\left(-2\pi i a_0 s\cos\psi - 2\pi^2\sigma_a^2 s^2\cos^2\psi - \frac{2}{n_0}\right)}\right]\right)d\psi \quad \text{Eq. 3.16}$$

where f is the constant scaling factor, b is the width of each nanostrips in the stacking structure, d is the integral width of Gaussian distribution of the electron density across the thickness of nanostrip, a_0 is the average interlayer distance, σ_a is the standard deviation of the interlayer

distance, n_0 is the average number of nanostrips in each stack following the exponential distribution.

3.4 Results and Discussion

3.4.1 Dimensions of Cellulose Nanostrips

In chapter 2, it was demonstrated that a simplified polydisperse ribbon model can efficiently fit the scattering patterns of cellulose nanofibers extracted from dried wood pulp with the TEMPO-oxidation method. Based on the model fitting, the structural information including cross-section size and cross sectional size distribution of cellulose nanofibers could be obtained, while the fiber length was assumed to be infinitely long in the model because lengths of around 1 μm far exceed the size range (0.5−100 nm) that SAXS can measure.

For cellulose nanostrip suspensions with concentrations of 0.077 and 0.15 wt%, the polydisperse ribbon model was used to fit both patterns. However, it can be seen from Figure 3.1 that this model fits the 0.077 wt% curve with high confidence (the coefficient of determination $R^2 = 0.9987$), but the discrepancy between the model and the 0.15 wt% curve is obvious because of the presence of a shoulder at $s = 0.3$ nm^{-1} on the experimental curve. The difference between the scattering profiles at low-concentration and high-concentration samples implied that the increase in concentration led to aggregation of nanostrips in the suspension.

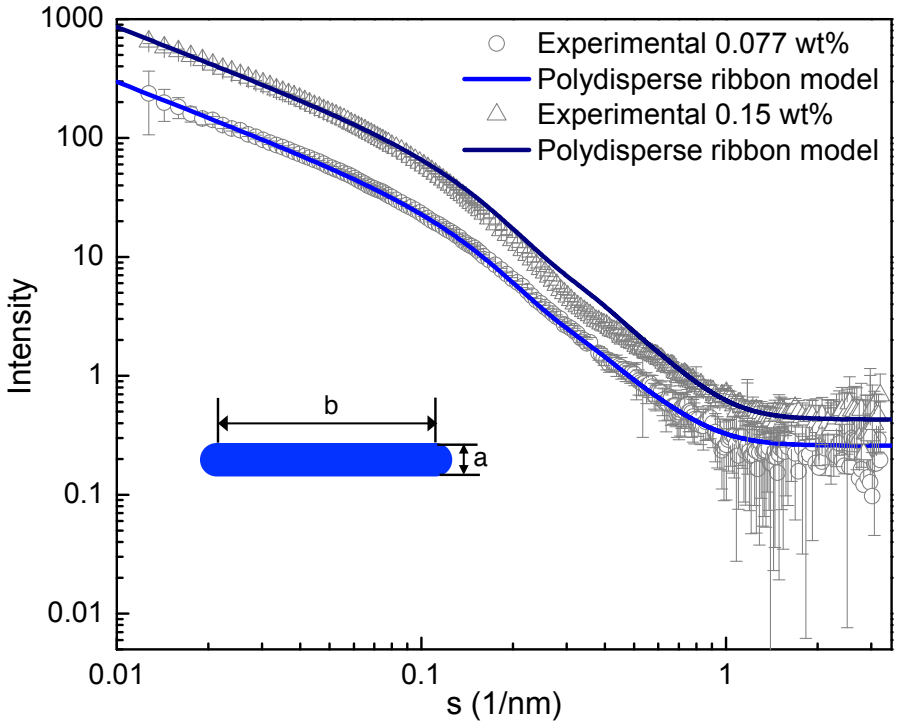

Figure 3.1 Experimental patterns of cellulose nanostrip suspensions at concentrations 0.077 and 0.15 wt%, respectively. The fitting results using the polydisperse ribbon model with average thickness a = 0.48 nm and standard deviation σ_a = 0.19 nm, and average width b = 3.94 nm and standard deviation σ_b = 0.5 nm. The inset shows the cross-section shape of the ribbon model.

For the 0.077 wt% sample, the average width b = 3.94 nm with a standard distribution σ_b = 0.5 nm derived from the polydisperse ribbon model was consistent with the width range 3.25−5.25 nm measured from the TEM images (Figure 3.2) as well as the reported widths of spruce cellulose microfibrils in previous literatures[2,12]. The average thickness a = 0.48 nm with a standard distribution σ_a = 0.19 nm of the ribbon model indicated that these cellulose nanostrips probably were microfibril fractions composed of single layer of cellulose chains. The AFM measurements have demonstrated that the thickness of a single nanostrip was around 0.5 nm (Figure 3.3). Meanwhile, fibers with thicknesses larger than 1 nm can also been seen in the AFM images, and these thicker fibers could possibly be stacks of the thin nanostrips formed in the evaporation process of the suspension. In addition, the bending and twisting of nanostrips on the mica substrate could also result in the apparent value of large thicknesses.

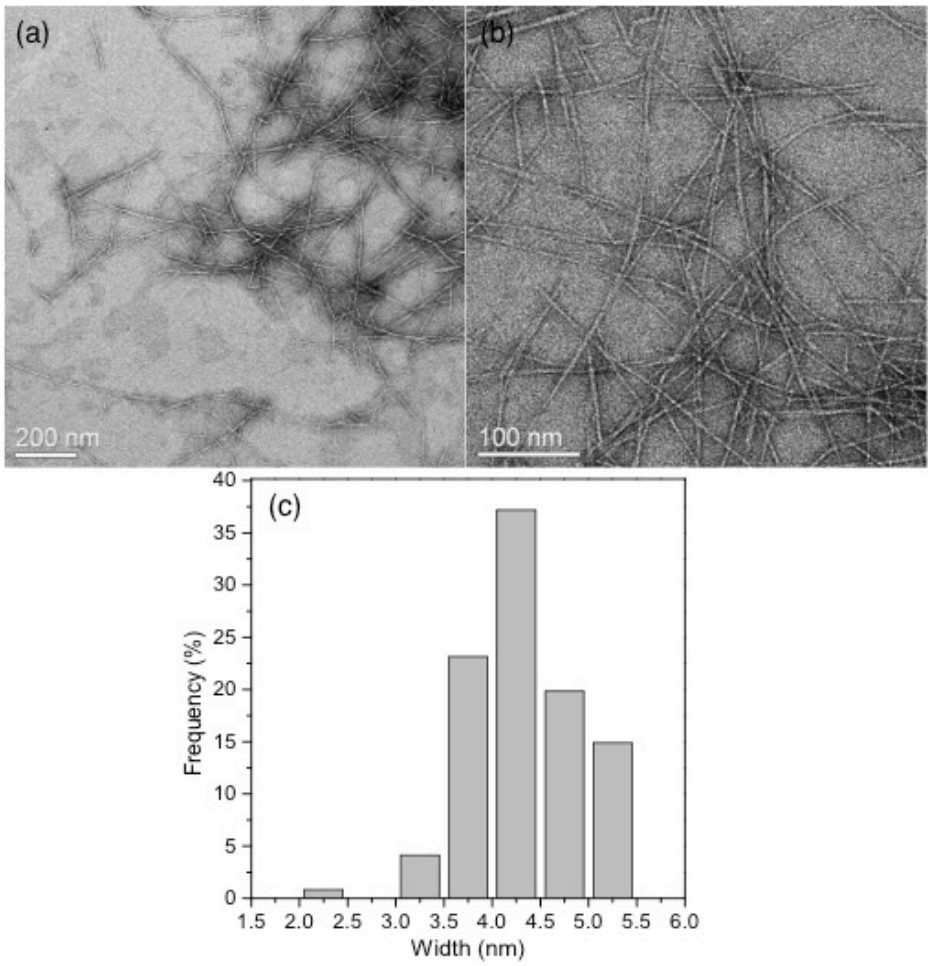

Figure 3.2 (a) and (b) are TEM images of cellulose nanostrips at different magnifications. (c) is the width distribution of nanostrips measured from TEM images based on a count of 124 nanostrips from 5 images.

For the 0.15 wt% sample, it was hypothesized that the very thin cellulose microfibril fractions aggregated during the water evaporation process and could form the stacking structures. To prove this hypothesis, a "1D paracrystalline" model was advanced to fit the 0.15 wt% curve, where the thin microfibril fractions were first simplified as monodisperse nanostrips with rectangular cross-sections. In the monodisperse nanostrip model, the width of the cross-section is uniform with no size distribution. Meanwhile, the thickness is also monodisperse and it is implemented with a Gaussian distribution of electron density across the thickness. This assumption was made mainly for the efficient calculation purpose; however, it also somehow simulated the electron density distributions of a single layer of cellulose molecules. The

expression of the monodisperse nanostrip model is shown in Equation 3.17 and the derivation of this model from the monodisperse parallelepiped model is illustrated in section 3.3.1.

$$I(s) = f\frac{1}{s}\exp(-2\pi s^2 d^2)\,{}_1\mathrm{F}_2(\frac{1}{2};\frac{3}{2},2;-\pi^2 s^2 b^2) + I_B \qquad \text{Eq. 3.17}$$

Where, *I(s)* is the scattering intensity, *s* is the modulus of scattering vector ($s = 2\sin\theta/\lambda$), *b* is the width of the cross-section of the nanostrip, *d* is the integral width of the Gaussian distribution of the electron density across the thickness, I_B is the constant background intensity, and *f* is the scaling factor of the intensity. In addition, ${}_1\mathrm{F}_2(\frac{1}{2};\frac{3}{2},2;-\pi^2 s^2 b^2)$ is a hypergeometric function and $\exp(-2\pi s^2 d^2)$ is an exponential function.

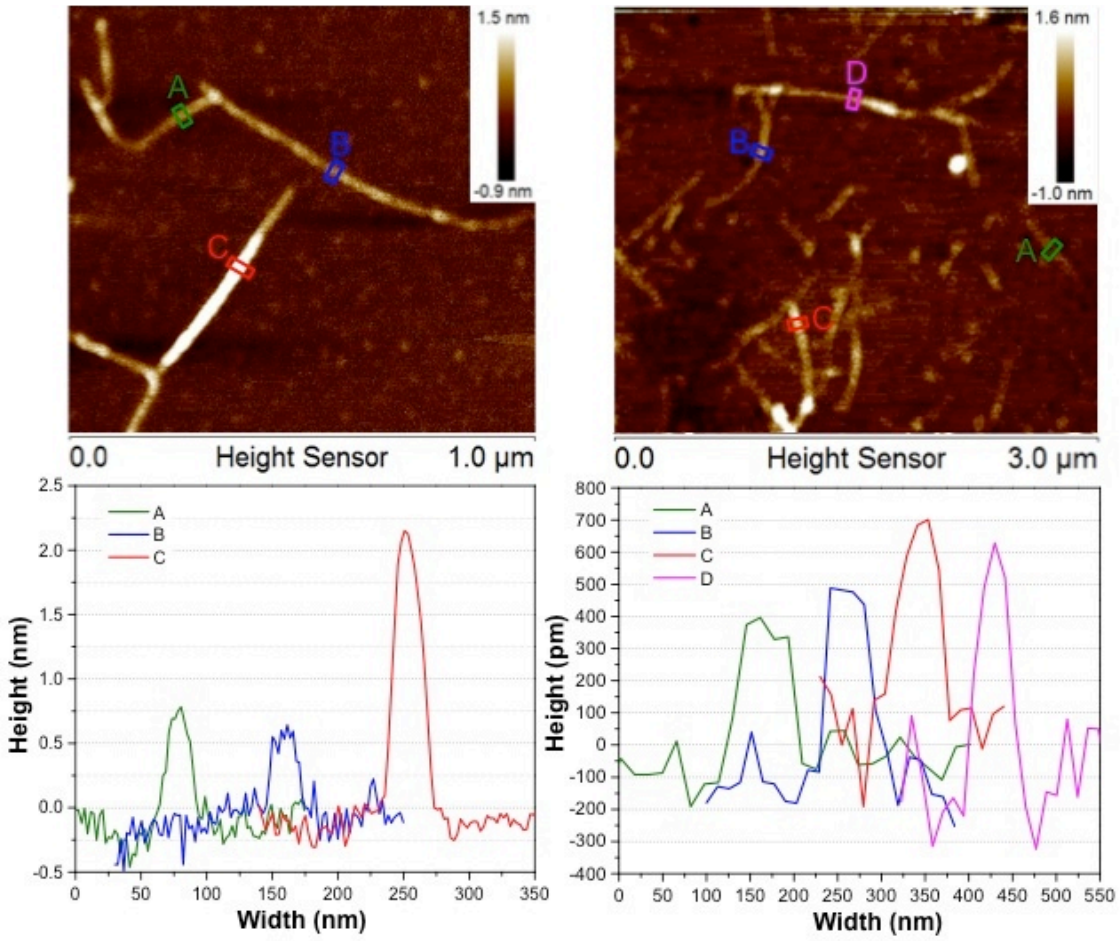

Figure 3.3 AFM height images of cellulose nanostrips. The height profiles of the fibers marked on the images are shown below the images.

To demonstrate the validity of this nanostrip model, Equation 3.17 was used to fit the 0.077 wt% sample using nonlinear least-squares fitting, and it turned out that with width $b = 3.93$ nm and integral width of the thickness $d = 0.40$ nm, the nanostrip model could fit the experimental curve with satisfying confidence (coefficients of determination $R^2 = 0.9996$) (Figure 3.4).

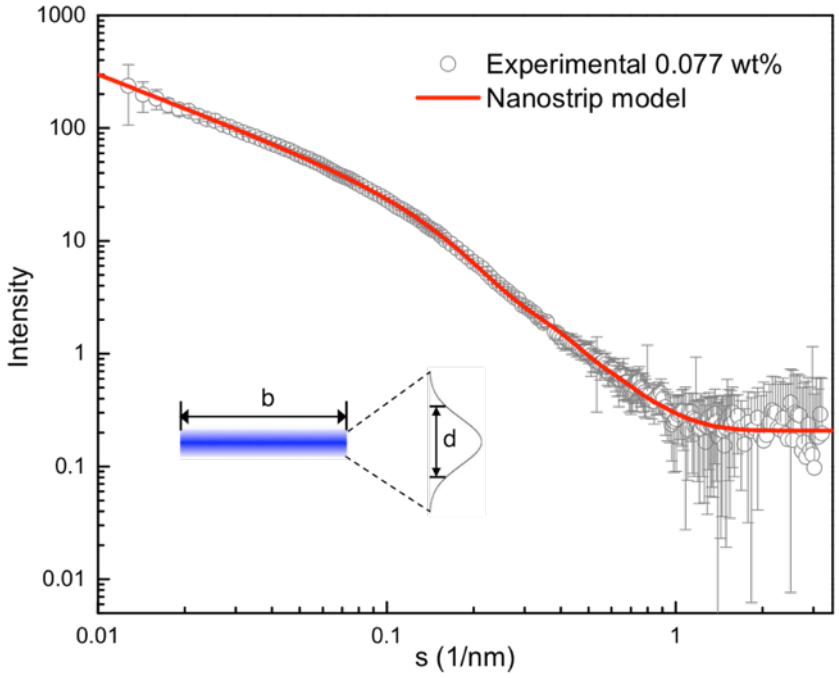

Figure 3.4 Experimental pattern for cellulose nanostrip suspensions at concentration 0.077 wt% and the fitting result of the nanostrip model with width b = 3.93 nm and integral width of the thickness d = 0.40 nm. The inset sketch shows the cross-section dimensions of the nanostrip model.

Using the nanostrips as building blocks, a "1D paracrystalline" model was developed to simulate the aggregation of cellulose microfibril fractions in aqueous suspension at high concentrations. Specifically, it was assumed that the cellulose nanostrips with thickness of 0.5 nm stacked up with their large surfaces facing each other. As there was no obvious peak on the curve, it was assumed that the distances between two adjacent nanostrips were not monodisperse, and it was further assumed to be of Gaussian distribution for the sake of the simplicity and computing efficiency of the model. With respect to the number of nanostrips in each stack, although we expected the aggregation of nanostrips in the suspension with higher concentration, we believed that most of the particles in the suspension should still be single nanostrips at the concentration of 0.15 wt%, as it was still very diluted suspension. Therefore we it was assumed that the number of nanostrips in each stack followed an exponential distribution. The expression of the "1D paracrystalline" model is shown in Equation 3.18:

$$I(s) = f\frac{\exp(-2\pi d^2 s^2)}{s}\int_0^{\frac{\pi}{2}} \frac{3b^2}{3+\pi^2 b^2 s^2 \sin^2\psi}\left[-1+2\,\mathrm{Re}\left[\frac{1}{1-\exp\left(-2\pi i a_0 s\cos\psi - 2\pi^2\sigma_a^2 s^2\cos^2\psi - \frac{2}{n_0}\right)}\right]\right]d\psi + I_B \quad \text{Eq. 3.18}$$

where f is the scaling factor, b is the width of each nanostrips, d is the integral width of Gaussian distribution of the electron density across thickness, a_0 is the average interlayer distance, σ_a is the standard deviation of the interlayer distance, n_0 is the average number of nanostrips in each stack following an exponential distribution, I_B is the background constant, and ψ is the azimuthal angle. The detailed derivation of the "1D paracrystalline" model is illustrated in section 3.3.2. The results showed that with b = 3.93 nm, d = 0.5 nm, a_0 = 1.4 nm, σ_a = 0.5 nm and n_0 = 1.6, the 0.15 wt% curve could be fitted very well with the "1D paracrystalline" model (Figure 3.5). It should be noted that, n_0 is statistically a decimal because it is the average number of the continuous exponential distribution ($f(n) = \frac{1}{n_0}\exp\left(-\frac{n}{n_0}\right)$) of the number of nanostrips n in each stack. The probability density curve (Figure 3.5) indicated that with n_0 = 1.6, the aggregates could be composed of more than two nanostrips, but the single nanostrips still dominated the suspension system.

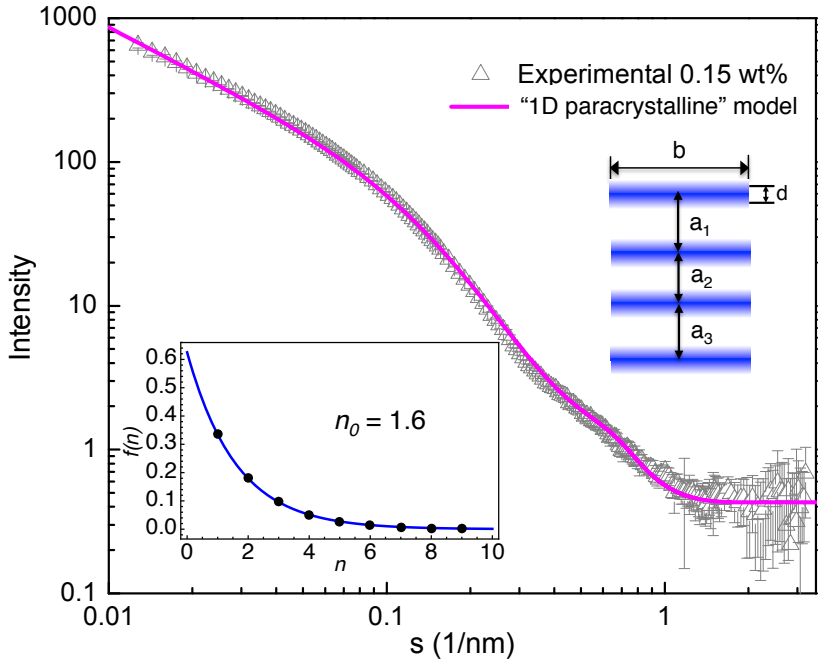

Figure 3.5 Experimental pattern for cellulose nanostrip suspensions at concentration 0.15 wt% and the fitting result of the "1D paracrystalline" model with width b = 3.93 nm, integral width of the electron density distribution across the thickness of each nanostrip d = 0.5 nm, average distance between adjacent nanostrips a_0 = 1.4 nm, standard deviation of the interlayer distance σ_a = 0.5 nm and average number of nanostrips in each stack n_0 = 1.6. The sketch in the upper-right corner shows the layered structure of the "1D paracrystalline" model; the inset in the bottom-left corner shows the exponential distribution curve of the number of layers in each stack.

3.4.2 Formation of Cellulose Nanostrip

Based on the fact that cellulose microfibrils could be delaminated into monomolecular sheets, now the question is when and how the delamination happened. To explore the possible mechanisms of the delamination, we studied the structure of the samples collected on different fabrication stages including delignification, TEMPO-mediated oxidation and successive mechanical homogenization.

The WAXD characterization was used to track the changes of crystalline structure of the abovementioned samples. From the comparison of the diffraction curves (Figure 3.6) of those samples, it can be seen that the $(1\,\bar{1}0)$ reflection disappeared gradually with the oxidation and homogenization proceedings, indicating that the cellulose crystallites might exfoliate along the

$(1\,\bar{1}0)$ planes. For the sample after the mechanical homogenization treatment, both (110) and (200) reflections shifted toward the amorphous halo (s ~ 2.1 nm^{-1}), suggesting the degradation of the crystalline structure, which could be explained by the fact of the appearance of a large amount of disordered cellulose chains on the surface of the nanostrips.

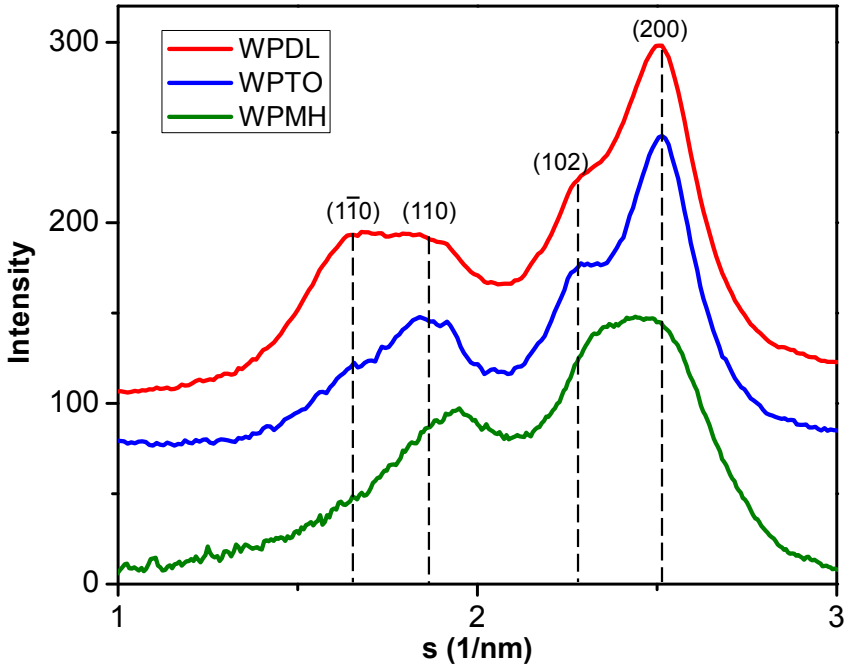

Figure 3.6 Comparison of WAXD patterns from samples after the delignification (WPDL), after the TEMPO-mediated oxidation (WPTO) and after the mechanical homogenizaiton (WPMH).

For native cellulose from specific biological sources (e.g. tunicate and *Valonia*), the microfibrils usually show planar orientation before fibrillation, which would influence the relative reflection intensities of the diffraction patterns[13,14]. However, for spruce cellulose, it has been known that the cellulose microfibrils only show uniaxial orientation in the cell wall before fibrillation, and no planar orientation could be observed[14]. Also the freeze-dry process of the samples generated a 3-dimensional structure with a random distribution of cellulose fibers, which prevented the orientation effect in the diffraction. Therefore, the intensity decrease of the $(1\,\bar{1}0)$ reflection with the oxidation and mechanical fibrillation treatment should be attributed to

the variation of the crystalline structure of the microfibril itself rather than the orientation effect.

Solid-state^{13} C-NMR spectra from the four samples (i.e. original spruce wood powder, WPDL, WPTO and WPMH) are shown in Figure 3.7. It is obvious that the lignin signals at 56 ppm and between 110 and 155 ppm[15] in the spectrum of the original wood powder disappeared completely after the delignification treatment. Meanwhile, some other polysaccharide components (e.g. hemicellulose and pectin) were also dissolved during the delignification, which was evidenced by the signal decrease at peak 62 ppm (pectin)[16] and the region of 81−82 ppm (hemicellulose)[17] in the spectrum of WPDL.

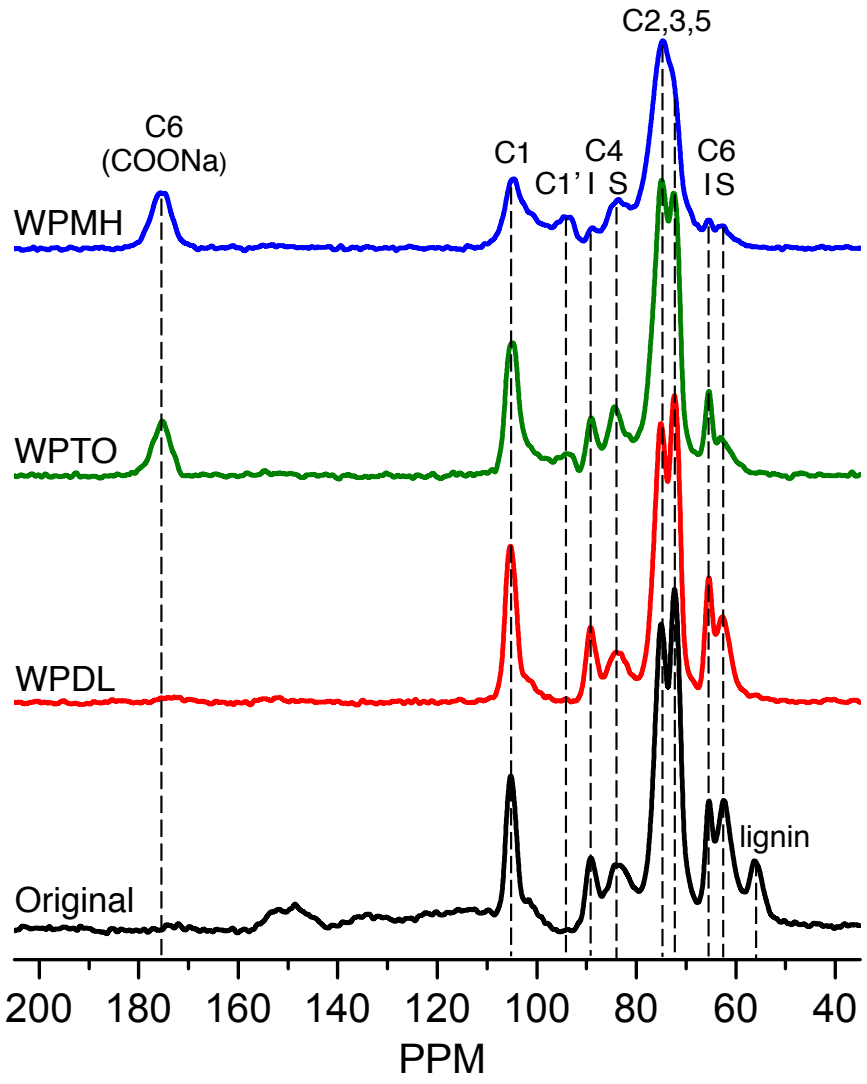

Figure 3.7 Solid-state CP-MASS ^{13}C-NMR spectra of original spruce wood powder, WPDL, WPTO and WPMH. For the peak assignment, "I" denotes inner/crystalline signal, "S" denotes surface/non-crystalline signal. C1' represents the reducing end of cellulose chain.

Comparing the spectra of WPDL and WPTO, it is clear that the peak assigned to carboxylate (COONa) at 175 ppm appeared after the oxidation reaction, and the intensity of the peak at 60−69 ppm corresponding to C6 decreased gradually. Also, the intensity of both the non-crystalline C6 (~63 ppm) and the crystalline C6 (~66 ppm) signals decreased after the oxidation, with crystalline C6 peak area falling from 12.7% to 7.3% and the non-crystalline C6 peak area from 4.6% to 3.4%, respectively. This indicated that not only the surface cellulose chains but also some of the inner chains were oxidized during the harsh oxidation process. The total peak

area at 81−92 ppm assigned to C4 remained unchanged (~12%). However, about 10% of crystalline C4 (at 87−92 ppm) turned into non-crystalline C4 (at 81−87 ppm) based on the difference of the peak areas before and after oxidation. Moreover, the decrease of C1 peak area from 16.5% to 14.3%, and the appearance of a shoulder at 94 ppm could be attributed to the formation of C1 reducing ends after the breaking of (1, 4) glycosidic bonds[18], implying that certain amount of cellulose chains were hydrolyzed during the oxidation process.

For the WPMH sample, the broadening of all the peaks in the region of 50−110 ppm on the spectrum was obvious, indicating that the whole system became more disordered after the mechanical homogenization. The peak area of crystalline C4 (87−92 ppm) dropped from 4.4% to 0.7% after homogenization, and the crystalline C6 (~66 ppm) decreased from 3.4% to 1.0%, which indicated that the delamination of cellulose microfibrils mainly occurred in the homogenization process, when cellulose microfibrils were cleaved into nanostrip-shape fractions.

The degree of oxidation (DO) determined from the conductometric titration is 0.50, which means that about 50% of the hydroxymethyl groups on cellulose have been oxidized into carboxylate groups during the TEMPO-mediated oxidation. It is well known that the inter-plane distances of $(1\bar{1}0)$ and (110) for I_β cellulose are 0.61 and 0.54 nm, respectively[19,20]. Assuming the $(1\bar{1}0)$ and (110) crystal planes are the exposed surfaces of the cellulose microfibrils[21], and assuming the cross-section of softwood cellulose microfibril is of near-square shape with width 4.1 nm and thickness 3.5 nm[12], there are $4.1/0.54 \approx 7$ chains in the $(1\bar{1}0)$ plane and $3.5/0.61 \approx 6$ chains in the (110) plane, respectively, and 22 out of the total 42 chains are on the surface of the microfibril. Assuming only the hydroxymethyl groups exposed on the surface could be oxidized, the maximum DO is $(20 \times 0.5 + 2)/42 = 0.29$. However, the actual DO 0.50 is much higher than

this maximum value, suggesting that besides the exposed hydroxymethyl groups, some "inner" hydroxymethyl groups also participated in the oxidation.

3.4.3 Proposed Delamination Mechanism

As hypothesized in previous literatures[22-25] talking about the biosynthesis and assembly of cellulose microfibrils, it takes multiple steps for cellulose crystallization in plant cell wall. Generally, it is believed that the van der Waals-associated $(1\,\bar{1}0)$ plane for I_β cellulose forms in the terminal complex (TC), and after extruded from the TC, these monolayers assemble through hydrogen bonding to form the crystalline microfibril. Meanwhile, it is known that hemicellulose plays a role of tethering adjacent cellulose microfibrils in the cell wall. In fact, hemicellulose not only binds to the surface of the cellulose microfibrils, but also is woven into the ordered cellulose microfibrils[26,27] (Figure 3.8(a)). Since each glucan chain monolayer is synthesized inside of the TC, where hemicellulose could not reach, the hemicellulose could not be trapped in the single sheet; while during the assembly of the sheets into crystalline microfibrils outside of the TC, it is very possible that the hemicellulose is trapped between the sheets, as shown in Figure 3.8(a).

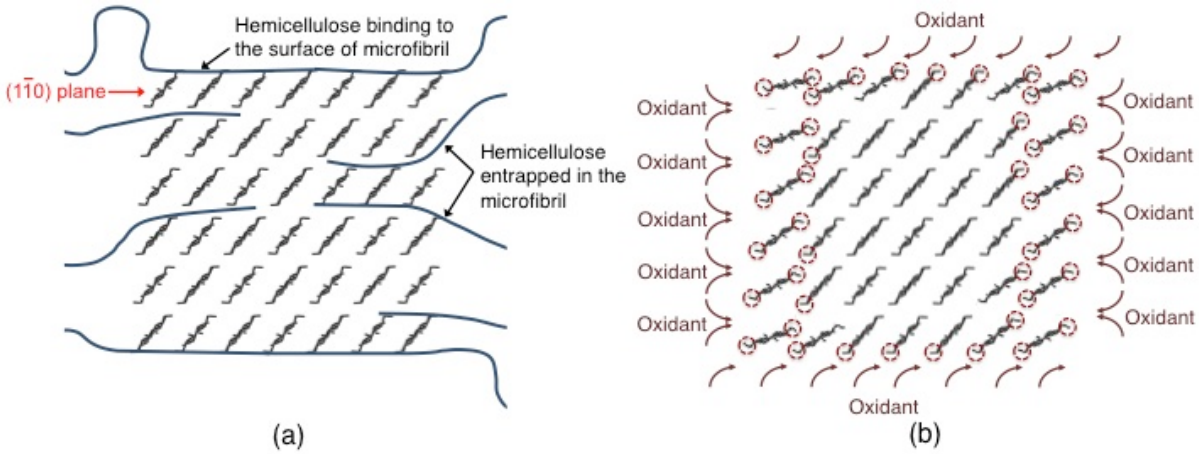

Figure 3.8 (a) Schematic diagram of the relationship between cellulose microfibril and hemicellulose; (b) schematic model of the oxidation process. Red circles represent the oxidized hydroxymethyl groups both on the surface of the microfibril and partially inside the microfibril.

During the delignification and TEMPO-mediated oxidation, the hemicellulose between the sheets is degraded and dissolves in the reaction system[28,29], leaving cracks for the oxidants to penetrate into the microfibrils, which results in the partial oxidation of inner molecules (Figure 8(b)). Eventually, the glucan chain sheets ($(1\bar{1}0)$ plane for I_β cellulose) delaminate along the cracks by the high power mechanical homogenization, and cellulose nanostrips were obtained consequently. These monomolecular sheets could disperse well in water at relatively low concentrations because of the negative charges introduced by the TEMPO-mediated oxidation. However, since the oxidation mainly occurred on the surface of microfibril and only partially occurred inside of the microfibril, the electrostatic repulsion among the monomolecular sheets would be weak and the aggregation of the sheets could occur in a concentrated suspension. Therefore, there was a thickness distribution of cellulose nanostrips in the suspension as confirmed by the SAXS analysis.

3.5 Conclusions

Cellulose nanostrips with width of ~4 nm and thickness of ~0.5 nm were fabricated by

delignification, oxidation and mechanical homogenization of spruce wood powder, and characterized comprehensively. The SAXS simulation confirmed that cellulose microfibril fractions after the TEMPO-mediated oxidation and successive mechanical homogenization formed nanostrips in an aqueous suspension (0.077 wt%), while the nanostrips turned to stack up to form multi-layer structures at a higher concentration. The TEM images verified the widths of cellulose nanostrips and the AFM measurements confirmed the thicknesses of nanostrips. The WAXD analysis suggested the formation mechanism of the cellulose nanostrips that the delamination of microfibril occurred along the $(1\bar{1}0)$ plane for I_β cellulose. This is consistent with the hypothesis of cellulose biosynthesis in plant cell wall, i.e. the monomolecular plane held by van der Waals forces formed inside the TC, multiple such planes assembled into the crystalline microfibril through hydrogen bonding outside the TC, and hemicellulose was trapped between planes, which would provide channels for oxidants to penetrate into the microfibril once the hemicellulose was removed (e.g., by chemical treatment). This was also confirmed by the fact that the actual DO of cellulose nanostrips was higher than the supposed DO considering only the surface molecular chains were oxidized. In addition, the solid-state ^{13}C NMR analysis also showed that some of the inner chains were oxidized during the harsh oxidation process, while the delamination of microfibrils mainly occurred during the intensive homogenization process.

References

(1) Saito, T.; Nishiyama, Y.; Putaux, J. L.; Vignon, M.; Isogai, A. *Biomacromolecules* **2006**, *7*, 1687.

(2) Isogai, A.; Saito, T.; Fukuzumi, H. *Nanoscale* **2011**, *3*, 71.

(3) Li, Q. Q.; Renneckar, S. *Biomacromolecules* **2011**, *12*, 650.

(4) Saito, T.; Kuramae, R.; Wohlert, J.; Berglund, L. A.; Isogai, A. *Biomacromolecules* **2013**, *14*, 248.

(5) Habibi, Y.; Chanzy, H.; Vignon, M. R. *Cellulose* **2006**, *13*, 679.

(6) Allaire, M.; Yang, L. *J Synchrotron Radiat* **2011**, *18*, 41.

(7) Wolfram Research, I. *Mathematica*; Version 8.0 ed.; Wolfram Research, Inc.: Champaign, Illinois, 2010.

(8) Saito, T.; Shibata, I.; Isogai, A.; Suguri, N.; Sumikawa, N. *Carbohyd Polym* **2005**, *61*, 414.

(9) Wickholm, K.; Larsson, P. T.; Iversen, T. *Carbohyd Res* **1998**, *312*, 123.

(10) Vietor, R. J.; Newman, R. H.; Ha, M. A.; Apperley, D. C.; Jarvis, M. C. *Plant J* **2002**, *30*, 721.

(11) Kato, Y.; Matsuo, R.; Isogai, A. *Carbohyd Polym* **2003**, *51*, 69.

(12) Okita, Y.; Saito, T.; Isogai, A. *Biomacromolecules* **2010**, *11*, 1696.

(13) Sugiyama, J.; Chanzy, H.; Revol, J. F. *Planta* **1994**, *193*, 260.

(14) Horikawa, Y.; Itoh, T.; Sugiyama, J. *Cellulose* **2006**, *13*, 309.

(15) Maciel, G. E.; Odonnell, D. J.; Ackerman, J. J. H.; Hawkins, B. H.; Bartuska, V. J. *Makromol Chem* **1981**, *182*, 2297.

(16) Ha, M. A.; Apperley, D. C.; Jarvis, M. C. *Plant Physiol* **1997**, *115*, 593.

(17) Hult, E. L.; Larsson, P. T.; Iversen, T. *Cellulose* **2000**, *7*, 35.

(18) Whitney, S. E. C.; Brigham, J. E.; Darke, A. H.; Reid, J. S. G.; Gidley, M. J. *Plant J* **1995**, *8*, 491.

(19) Sugiyama, J.; Vuong, R.; Chanzy, H. *Macromolecules* **1991**, *24*, 4168.

(20) Nishiyama, Y.; Langan, P.; Chanzy, H. *J Am Chem Soc* **2002**, *124*, 9074.

(21) Sugiyama, J.; Harada, H.; Fujiyoshi, Y.; Uyeda, N. *Planta* **1985**, *166*, 161.

(22) Moon, R. J.; Martini, A.; Nairn, J.; Simonsen, J.; Youngblood, J. *Chem Soc Rev* **2011**, *40*, 3941.

(23) Cousins, S. K.; Brown, R. M. *Polymer* **1995**, *36*, 3885.

(24) Saxena, I. M.; Brown, R. M. *Ann Bot-London* **2005**, *96*, 9.

(25) Delmer, D. P. *Annu Rev Plant Phys* **1999**, *50*, 245.

(26) Cosgrove, D. J. *Nature reviews. Molecular cell biology* **2005**, *6*, 850.

(27) Hayashi, T. *Annu Rev Plant Phys* **1989**, *40*, 139.

(28) Kumar, R.; Hu, F.; Hubbell, C. A.; Ragauskas, A. J.; Wyman, C. E. *Bioresource Technol* **2013**, *130*, 372.

(29) Okita, Y.; Saito, T.; Isogai, A. *Holzforschung* **2009**, *63*, 529.

Chapter 4 SAXS Characterization of Silver Ion Decorated Cellulose Nanofibers

4.1 Introduction

Silver compounds and silver ions have been historically used for bactericidal purpose over a wide range of applications, such as disinfecting medical devices, wound dressings, textile fabrics, water treatments and so on[1,2]. The mechanism of the antimicrobial activity of silver is believed to be that the silver ions could break into the cell of bacteria, bond to the cellular enzymes through the –SH groups, eliminate the enzymatic activity, and eventually inhibit the cell growth and cause cell death[3,4].

Silver nanoparticles have attracted a great deal of attentions in both academic and industrial research on antimicrobial effects because of their large specific surface area and high reactivity[1]. However, the separation and recycling of the used silver nanoparticles is very difficult due to their extremely small size. Therefore, the immobilization of silver nanoparticles onto a substrate has become important for the applications of silver nanoparticles. It has been reported that silver nanoparticles could be embedded in various polymers (e.g. polyamides, poly (allylamine hydrochloride) and poly (acrylic acid), poly (4-vinyl-N-hexylpyridinium bromide), etc.) to form polymer-silver composite films[5-7], but one problem with such immobilization is that only the nanoparticles on the surface of the film are effective while those embedded inside the matrix can hardly release Ag^+ to the environment.

Depositing silver nanoparticles onto a porous structure constituted by nanofibers with large surface areas can significantly increase the dose of active nanoparticles. Recently, a great deal of research has been carried out for the preparation of antimicrobial silver nanoparticle-

cellulose nanofiber composite systems through in situ synthesis of silver nanoparticles using cellulose nanofibers as nanoreactors[8,9]. For natural cellulose, most of the groups on the fiber surfaces are hydroxyl groups, and the electrostatic interactions between hydroxyl groups and silver ions are usually weak. In contrast, cellulose nanofibers after TEMPO-mediated oxidation have a large amount of surface C6 hydroxyl groups oxidized into carboxylate groups, which can provide stronger adsorption to metal ions. Once the silver ions are anchored onto the cellulose surfaces as counter ions of carboxylate groups, the amount of ions lost after dialysis with DI water should be limited. It has been found that silver ions can be successfully deposited onto the surface of TEMPO-oxidized cellulose with Ag^+/carboxylate molar ratio of about 1:1[10].

To study how the silver ions bonded to and accumulated on the cellulose nanofibers, the work in this chapter investigated the morphology and interactions of cellulose nanofibers with silver ions deposited on the surfaces by solution SAXS, and a stacking model was developed to fit the SAXS pattern.

4.2 Materials and Methods

4.2.1 Materials

TEMALFA-95 (fully bleached sulfite spruce wood pulp with I_α cellulose content of 95%) was provided by Tembec Inc., Canada. 2,2,6,6-tetramethyl-1- piperidinyloxy (TEMPO), sodium hypochlorite (NaClO), sodium bromide (NaBr) and silver nitrate ($AgNO_3$) were purchased from Sigma-Aldrich. All samples were used as purchased, without further purification.

4.2.2 Preparation of Cellulose Nanofibers

Dried TEMALFA-95 pulps (1 g) were first broken down into small pieces and then soaked in water (about 30 mL) overnight. Both sodium bromide (0.1 g) and TEMPO agent (0.02

g) were dissolved in the suspension. A desired amount of sodium hypochlorite solution (12 mmol per gram of cellulose) was subsequently added to initiate the oxidization process, where the reaction was carried out under mechanical stirring in a sealed bottle for 24 hours. The pH value of the suspension was kept between 10.0 and 11.0 during the reaction (monitored with a pH meter) by addition of sodium hydroxide aqueous solution (1 mol/L). The oxidized cellulose fibrous samples were collected by centrifuging the reaction mixture at ~2350 g, followed by washing with deionized water for several times until the pH value reached ~8. Afterward, all fibrous samples were dispersed in 100 mL of water and disintegrated with a homogenizer (Cole Parmer, VCX-400) at 79% rate (60 Hz, 115 W) for 10 min. The suspension was centrifuged again at ~4700 g for 30 min, where the supernatant containing finely dispersed cellulose nanofibers was collected for X-ray measurements. The concentration of the cellulose nanofiber suspension was determined by using a total organic carbon (TOC) analyzer.

4.2.3 Determination of Degree of Oxidation

The ratio between the amount of oxidized and the total hydroxymethyl groups in oxidized cellulose was determined by using the conductometric titration method[11]. Briefly, 0.1 mol/L of hydrochloric acid aqueous solution were dropped to 24 mL of cellulose nanostrip suspension at a concentration of 0.05 wt% until the pH reached to 2.8. The suspension was titrated with 0.005 mol/L NaOH solution with stirring using a magnetic stirrer at the stirring rate of 450 rpm. The conductivity of the suspension was monitored using a conductivity meter throughout the titration process. The titration performance was terminated when the pH reached 10.7. The curve of conductivity versus volume of NaOH solution used was plotted, and the volume of NaOH aqueous solutions used to neutralize the carboxyl groups, V, was determined from the curve. The amount of oxidized hydroxymethyl groups was calculated by multiplying V with the

concentration, *C*, of the NaOH solution, while the amount of cellulose was directly measured from the TOC analyzer.

4.2.4 Preparation of Silver Ion Decorated Cellulose Nanofibers

Silver nitrate ($AgNO_3$) aqueous solution at concentration 0.1 mmol/mL was first prepared for this process. Subsequently, 240 μL of $AgNO_3$ solution was added to 30 mL TEMALFA-95 cellulose nanofiber suspension at concentration of 0.08 wt% and with DO of 16.3%. The molar ratio between Ag^+ ions and carboxylate groups was about 1:1. The mixture was kept under mechanical stirring in a sealed dark bottle for 6 hours. Afterwards, the mixture was dialyzed with dialysis tubing (MWCO 10000 DA) using DI water in a dark room to remove the excessive Ag^+ ions,

4.2.5 Synchrotron Solution SAXS/WAXD

Simultaneous SAXS/WAXD measurements of cellulose nanostrip suspensions were carried out at Beamline X9 of the National Synchrotron Light Source (NSLS), Brookhaven National Laboratory (BNL), USA. Two TEMALFA-95 cellulose nanofiber suspensions at concentration of 0.08 wt% before and after the silver ion adsorption were used for the investigation. In a scanning process, 20 μL suspension was pumped into a glass capillary (diameter of 1 mm) sealed across the vacuum path. The sample was allowed to flow continuously through the capillary during data collection in order to minimize radiation damage[12]. The X-ray wavelength at Beamline X9 was 0.0918 nm. A PILATUS 300 K detector located 3.2 m away from the sample was used to collect the SAXS data. A custom-designed Photonic Science CCD detector, 463 mm from the sample, took the 2D WAXD patterns. For each sample, three 30-second scans were taken. The average of these three scans was used as the scattering pattern of the sample. A silver behenate standard was used to calibrate the parameters

of the scattering geometry (i.e. beam center and sample-to-detector distance). Preliminary data processing was done with a Python-based package developed at the X9 Beamline to convert the two-dimensional (2D) images into one-dimensional (1D) scattering profiles, block off dead pixels and pixels behind the beam-stop, merge SAXS and WAXD scans, and subtract the buffer and capillary background from the scattering profile. In this study, only the profile in small-angle region ($s < 1$ nm^{-1}) was simulated, and the analysis of the wide-angle part was not involved here. The model development and model fitting of the SAXS data was performed using the softwate *Mathematica*[13].

4.3 Model Development for Solution SAXS Analysis

As described in previous chapters, the scattered intensity distribution is related to the electron density distribution in the investigated system. For the cellulose nanofibers with silver ions anchored on the surfaces, since Ag has much larger atomic weight comparing with C, O and H, the elements composing of the cellulose and water matrix, the scattered intensity should be dominated by the distribution of silver ions instead of cellulose nanofibers in the current system.

Comparing the SAXS patterns of samples with and without silver ion adsorption (Figure 4.1), we found that for the silver ion adsorbed sample, a distinct broad peak emerged at $s \sim 0.4$ nm^{-1} ($s = 2\sin\theta/\lambda$), while there was no such peak present in the patterns of the control samples. The peak at $s \sim 0.4$ nm^{-1} indicated that there was short-range order in the suspension, and the corresponding mean center-to-center spacing was about 2.5 nm. Based on the previous SAXS analysis of cellulose nanofibers in Chapter 2, the TEMALFA-95 cellulose nanofibers were ribbon-like with near rectangular cross-sections, and the average thickness and width were about 3.3 nm and 8.7 nm, respectively. Given this information, it is reasonable to suggest that the silver ions mainly anchored to the top and bottom surfaces of the ribbon shaped nanofibers, and since

one silver ion may bond with two or three carboxylate groups[10], the small peak at ~ 0.4 nm^{-1} could be attributed to the stacking of several nanofibers with silver ions between the top surface of one nanofiber and the bottom surfaces of another.

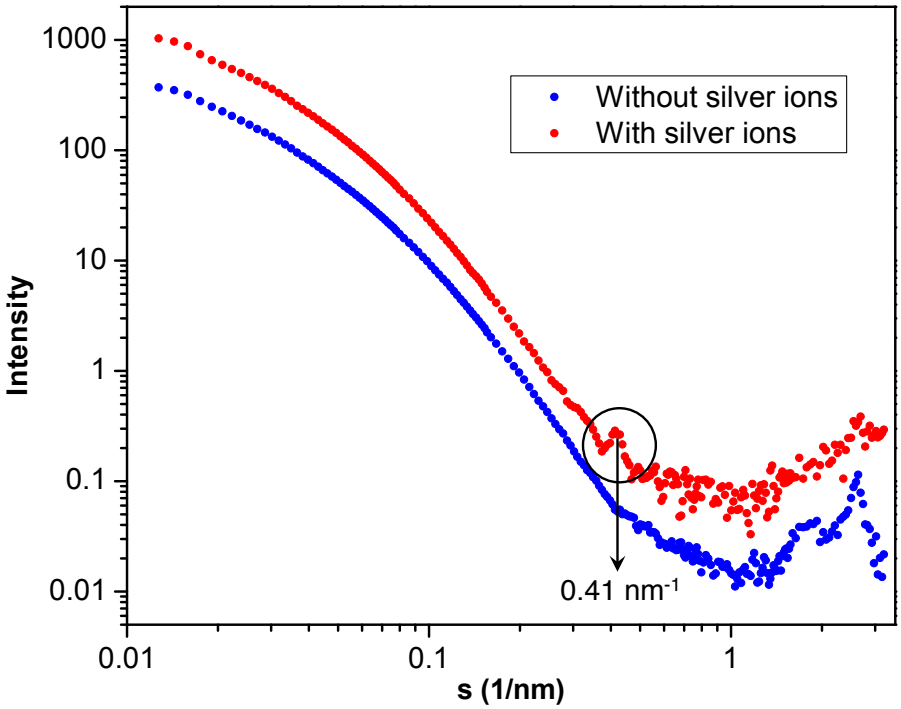

Figure 4.1 Comparison of simultaneous SAXS/WAXD patterns from TEMAlFA-95 nanofiber suspensions at concentration of 0.08 wt% with and without silver ions attached, respectively. The curves were manually shifted vertically for visual clarity. The peak marked with the circle locates at $s = 0.41$ nm^{-1}.

Based on the "1D paracrystalline" model introduced in Chapter 3, a simplified "1D paracrystalline" model with a finite stack height was developed that is suitable to analyze the scattering results. Compared to the "1D paracrystalline" with integral calculation involved in the model, the simplified model has a much higher computing efficiency because of the analytical solution.

Specifically, in this system, cellulose nanofibers stack up with silver ions adsorbed as bridging molecules between the top and bottom surfaces of nanofibers. In this scenario, we assume that n layers of silver ions are parallel placed at n points distributed in a line with inter-

position distance r, which is polydisperse with average a_0 and standard deviation σ_a, and the height of the stack is finite. As explained in the "1D paracrystalline" model, for such a system with n lattice points that are polydisperse and having an exponential distribution with average n_0, the structure factor can be expressed as:

$$S(s) = -1 + 2\mathrm{Re}\left[\frac{1}{1 - h(s)\exp\left(-\frac{2}{n_0}\right)}\right] = -1 + 2\mathrm{Re}\left[\frac{1}{1 - \exp\left(-2\pi i a_0 s - 2\pi^2\sigma_a^2 s^2 - \frac{2}{n_0}\right)}\right] \quad \text{Eq. 4.1}$$

The curve of Equation 4.1 consists of two parts: the low-s region (s ~ 0.01-0.15 nm^{-1}) and the high-s region (s ~ 0.15-0.2 nm^{-1}). Physically, the low-s region intensity mainly comes from the scattering of large structures. In this system, the large structures are the stacks composed of several nanofibers, and the stacks function as large particles in the aqueous suspension. Mathematically, the low-s region curve comes from the initial part of the convolution between a near-Shah function with polydisperse distances between two neighboring poles and a rectangular function. The near-Shah function represents the position of the lattice points and the rectangular function represents the silver planes placed on the lattice points. Since the shape of the convolution result resembles a Lorentzian function, the low-s region curve can be separated from the whole scattering curve (Equation 4.1) using the following expression:

$$S_1(s) = \frac{n_0}{1 + \pi^2 n_0^2 a_0^2 s^2} \quad \text{Eq. 4.2}$$

where n_0 is the average number of silver-ion planes in each stack and a_0 is the average distance between each silver planes. Then the high-s part (Equation 4.3) of the curve is the remaining part with Equation 4.2 subtracted from Equation 4.1, as shown in Figure 4.2.

$$S_2(s) = -1 + 2\mathrm{Re}\left[\frac{1}{1 - \exp\left(-2\pi i a_0 s - 2\pi^2\sigma_a^2 s^2 - \frac{2}{n_0}\right)}\right] - \frac{n_0}{1 + \pi^2 n_0^2 a_0^2 s^2} \quad \text{Eq. 4.3}$$

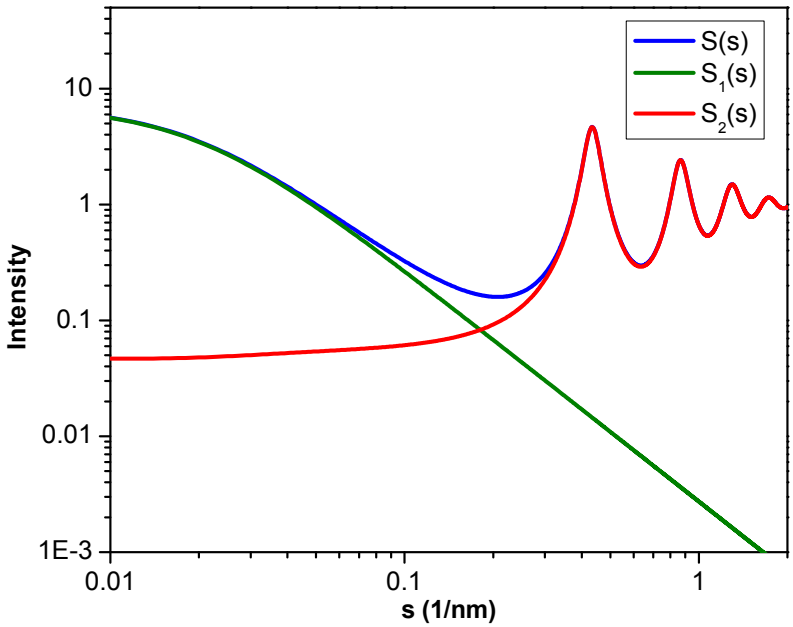

Figure 4.2 Comparison of the whole structure factor curve ($S(s)$), Lorentzian curve ($S_1(s)$) and the remaining part ($S_2(s)$). All the three curves are plotted with parameters $n_0 = 7$, $a_0 = 2.3$ nm and $\sigma_a = 0.2$ nm.

With regard to the form factor of the silver-ion plane, we can use the one previously developed for the nanostrips as described in section 3.3.1:

$$F^2(s) = \frac{L}{2s}\exp(-2\pi d^2 s^2)\left(b\frac{\sin(\pi bs)}{\pi bs}\right)^2 \qquad \text{Eq. 4.4}$$

where b is the width of the silver-ion plane, d is the integral width of the Gaussian distribution of the electron density across the thickness of silver-ion plane, and L is the length of the silver-ion plane. Multiplying the form factor with $S_1(s)$ and $S_2(s)$, respectively, and averaging the intensity over all possible orientations in the cross-section plane, we get:

$$I_1(s) = \frac{L}{2s}\exp(-2\pi d^2 s^2)\int_0^{\pi/2}\frac{3b^2}{3+\pi^2 b^2 s^2\sin^2\psi}\frac{n_0}{1+\pi^2 n_0^2 a_0^2 s^2\cos^2\psi}d\psi \qquad \text{Eq. 4.5}$$

$$I_2(s) = \frac{L}{2s}\exp(-2\pi d^2 s^2)\int_0^{\pi/2}\frac{3b^2}{3+\pi^2 b^2 s^2\sin^2\psi}\left(-\frac{n_0}{1+\pi^2 n_0^2 a_0^2 s^2\cos^2\psi}-1+2\,\mathrm{Re}\left[\frac{1}{1-\exp\left(-2\pi i a_0 s\cos\psi-2\pi^2\sigma_a^2 s^2\cos^2\psi-\frac{2}{n_0}\right)}\right]\right)d\psi$$

Eq. 4.6

The analytical solution of Equation 4.5 is:

$$I_1(s) = \frac{L}{2s}\exp(-2\pi d^2 s^2)\frac{\dfrac{b^4 n_0}{\sqrt{1+\frac{1}{3}b^2\pi^2 s^2}} + \dfrac{3a_0^2 b^2 n_0^3}{\sqrt{1+a_0^2 n_0^2 \pi^2 s^2}}}{3a_0^2 n_0^2 + b^2(1+a_0^2 n_0^2 \pi^2 s^2)} \qquad \text{Eq. 4.7}$$

Since Equation 4.6 calculates the high-s region intensity, where the azimuthal angle Ψ is small, it is assumed that $\cos\Psi \approx 1$ and $\sin\Psi \approx$ t in Equation 4.6. With this assumption, we can derive the analytical solution for Eq. 4.6 as follows:

$$I_2(s) = \exp(-2\pi d^2 s^2)\frac{\sqrt{3}bL}{2\pi s^2}\left[-\frac{n}{1+a^2 n^2 \pi^2 s^2} - 1 + 2\,\mathrm{Re}\left[\frac{1}{1-\exp\left(2\pi i a s - 2\pi^2\sigma^2 s^2 - \frac{2}{n}\right)}\right]\right] \qquad \text{Eq. 4.8}$$

Eventually the total scattering intensity of the whole system is given by:

$$I(s) = I_1(s) + I_2(s) \qquad \text{Eq. 4.9}$$

Equations 4.7, 4.8 and 4.9 are plotted in Figure 4.3.

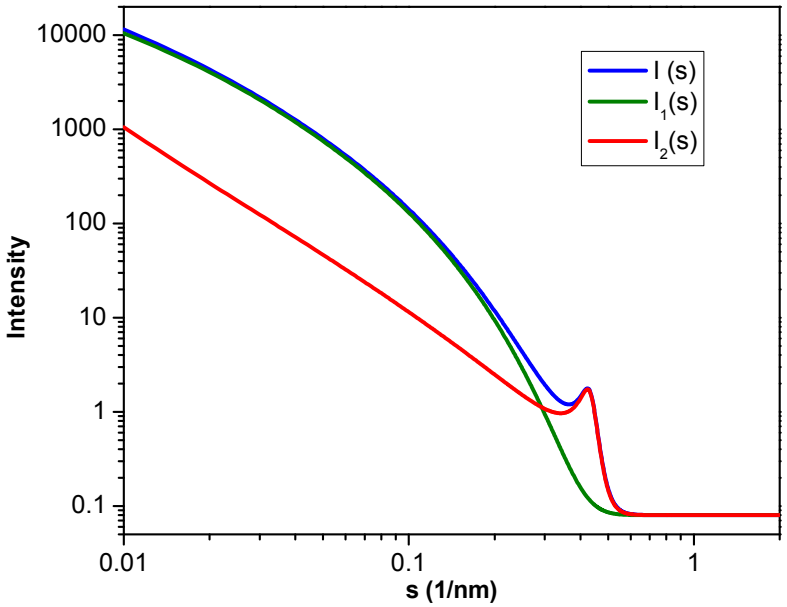

Figure 4.3 Comparison of the whole intensity curve ($I(s)$), low-s intensity curve ($I_1(s)$) and the high-s intensity curve ($I_2(s)$). All the three curves are plotted with parameters $n_0 = 7$, $a_0 = 2.3$ nm, $\sigma_a = 0.2$ nm, $b = 4.1$ nm, and $d = 1.75$ nm.

4.4 Results and Discussion

The experimental SAXS data from silver ion decorated TEMALFA-95 cellulose nanofibers was analyzed by model fitting using the simplified "1D paracrystalline" model. As shown in Figure 4.4, the model with n_0 = 7, a_0 = 2.3 nm, σ_a = 0.2 nm, b = 4.1 nm, and d = 1.75 nm can fit the experimental data with satisfying agreement. These parameters indicated that there were 7 silver-ion layers in each stack on average, corresponding to 6 nanofibers stacking together, and since it followed an exponential distribution, most stacks would have less than 7 layers, as shown in the probability density curve of the exponential distribution (the Figure 4.4 inset).

The average inter-layer distance was 2.3 nm with a small standard deviation of 0.2 nm, implying that the cellulose nanofibers between two adjacent silver-ion layers in the stack had a relatively uniform thickness. This inter-layer average distance was smaller than 3.3 nm, which was the size-weighted average thickness of TEMALFA-95 cellulose nanofibers without silver-ion decoration. The possible reason could be that compared to thicker nanofibers, the thinner nanofibers preferred to stack up to form a multi-layer aggregate. For thicker nanofibers, although silver ions could possibly deposit onto the top and bottom surfaces of nanofibers and might therefore cause weak broad bump at a lower s position, we did not take this into consideration to avoid overfitting caused by having too many parameters.

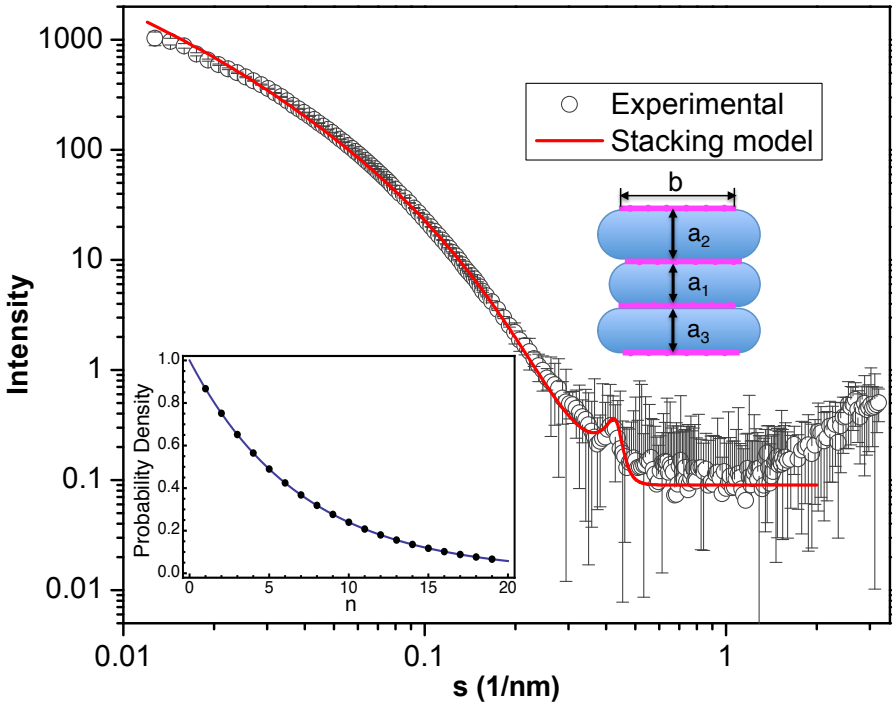

Figure 4.3 Experimental SAXS pattern of silver-ion decorated cellulose nanofibers and the fitting result of the simplified "1D paracrystalline" model $n_0 = 7$, $a_0 = 2.3$ nm, $\sigma_a = 0.2$ nm, $b = 4.1$ nm, and $d = 1.75$ nm. The sketch in the upper-right corner shows the cross-section view of the layered structure of a stack. The pink lines represent the silver ion planes and the blue rectangles represent the cellulose nanofibers; the inset in the bottom-left corner shows the exponential distribution curve of the number of silver-ion planes in each stack.

From the model fitting, the width of the silver-ion plane was determined to be 4.1 nm, which was much smaller than the average width of the cellulose nanofibers (8.7 nm) without silver-ion adsorption. This might be because the distribution of silver ions were mainly on the surface of nanofibers, i.e., silver ions preferred to accumulate to the middle of the surfaces rather than the edges. The small width of silver-ion planes might also be caused by the fashion that the nanofibers stacked up, i.e., the center of the nanofiber cross-sections were arranged in a zig-zag way instead of in a line.

The parameter d in the model referred to the integral width of a Gaussian distribution, which described the electron density distribution across the thickness of the silver-ion planes. This assumption was made based on the fact that although we called it a "plane", it was

impossible for the silver ions strictly standing on a plane as the molecules on the surfaces of nanofibers were pretty disordered. This indicated that there should be a thickness of the plane, and therefore to some extent, *d* could be considered as the thickness of the plane. Alternatively, since the interface between the silver-ion plane and its matrix was not sharp, *d* could be considered as the thickness of the blurry border between the plane and it matrix, which were cellulose nanofibers in this case.

4.5 Conclusions

Since the TEMPO-mediated oxidation introduced large amount of carboxylate groups onto the surfaces of cellulose nanofibers, silver ions can easily deposit onto the nanofiber surfaces as the counter ions of carboxylate groups by ion exchanging with the original sodium ions. The adsorption of silver ions caused the stacking of cellulose nanofibers with silver ions functioning as bridges. The inner structure of the stacks was investigated by solution SAXS technique, and a simplified "1D paracrystalline" model was developed to fit the SAXS data. From the model fitting, it was determined that the number of silver-ion layers in the stacks followed an exponential distribution with an average of 7. The average inter-layer distances was 2.3 nm, which was smaller than the average thickness of cellulose nanofibers, indicating that it was easier for thinner nanofibers to stack up compared to thick nanofibers. The width of silver-ion planes determined from the simplified "1D paracrystalline" model was 4.1 nm, much smaller than the average width of nanofibers, which might be caused by the non-uniform distribution of silver ions on the surfaces of nanofibers.

References

(1) Li, Q. L.; Mahendra, S.; Lyon, D. Y.; Brunet, L.; Liga, M. V.; Li, D.; Alvarez, P. J. J. *Water Res* **2008**, *42*, 4591.

(2) Banerjee, I.; Pangule, R. C.; Kane, R. S. *Adv Mater* **2011**, *23*, 690.

(3) El-Rafie, M. H.; Mohamed, A. A.; Shaheen, T. I.; Hebeish, A. *Carbohyd Polym* **2010**, *80*, 779.

(4) Dastjerdi, R.; Montazer, M.; Shahsavan, S. *Colloid Surface A* **2009**, *345*, 202.

(5) Sambhy, V.; MacBride, M. M.; Peterson, B. R.; Sen, A. *J Am Chem Soc* **2006**, *128*, 9798.

(6) Damm, C.; Munstedt, H. *Appl Phys a-Mater* **2008**, *91*, 479.

(7) Agarwal, A.; Weis, T. L.; Schurr, M. J.; Faith, N. G.; Czuprynski, C. J.; McAnulty, J. F.; Murphy, C. J.; Abbott, N. L. *Biomaterials* **2010**, *31*, 680.

(8) He, J. H.; Kunitake, T.; Nakao, A. *Chem Mater* **2003**, *15*, 4401.

(9) Barud, H. S.; Regiani, T.; Marques, R. F. C.; Lustri, W. R.; Messaddeq, Y.; Ribeiro, S. J. L. *J Nanomater* **2011**.

(10) Saito, T.; Isogai, A. *Carbohyd Polym* **2005**, *61*, 183.

(11) Habibi, Y.; Chanzy, H.; Vignon, M. R. *Cellulose* **2006**, *13*, 679.

(12) Allaire, M.; Yang, L. *J Synchrotron Radiat* **2011**, *18*, 41.

(13) Wolfram Research, I. *Mathematica*; Version 8.0 ed.; Wolfram Research, Inc.: Champaign, Illinois, 2010.

Chapter 5 Characterization of Jute Cellulose Fibers with Preferred Orientation

5.1 Introduction

Jute fibers are a type of vegetable fibers with high tensile strength and low extensibility, and they are extracted from the stem and outer skin of *Corchorus* plant. Compared to wood fibers, jute fibers have higher cellulose content (45-71%) and crystallinity[1-3]. The cellulose crystals in the elongated cell walls of jute fibers grow parallel or nearly parallel to the fiber axis with high degree of preferred orientation, forming the cylindrical rotational symmetry, which is also called "fiber symmetry"[4]. The degree of preferred orientation is an important parameter to estimate the mechanical properties of polymers, and usually it can be quantitatively determined through the 2D X-ray diffraction technique.

Unlike the pattern of an isotropic system (i.e. powder system), the 2D diffraction of a system with fiber symmetry shows an anisotropic pattern, with arc-shaped peaks distributed at different polar angles (Figure 5.1). The radial intensity distribution of an arc is dominated by the crystal size along a certain direction, and the angular intensity distribution is related to the degree of preferred orientation of the crystals. Although the crystal dimensions could be analyzed by using traditional Lorentzian or Gaussian peak profile analysis similar to the line profile analysis as introduced in Chapter 1, the degree of preferred orientation usually could not be determined by simply measuring the angular intensity distributions[4]. In this case, the 2D whole pattern simulation with a proper Orientation Distribution Function (ODF) is useful to analyze the fiber system. By adopting this method, the scattering intensity dependence on both the scattering vector s and polar angle φ can be taken into consideration simultaneously, which makes it

possible to calculate the degree of preferred orientation, the crystal sizes as well as to discriminate diffraction peaks contributed from different crystal phases[5].

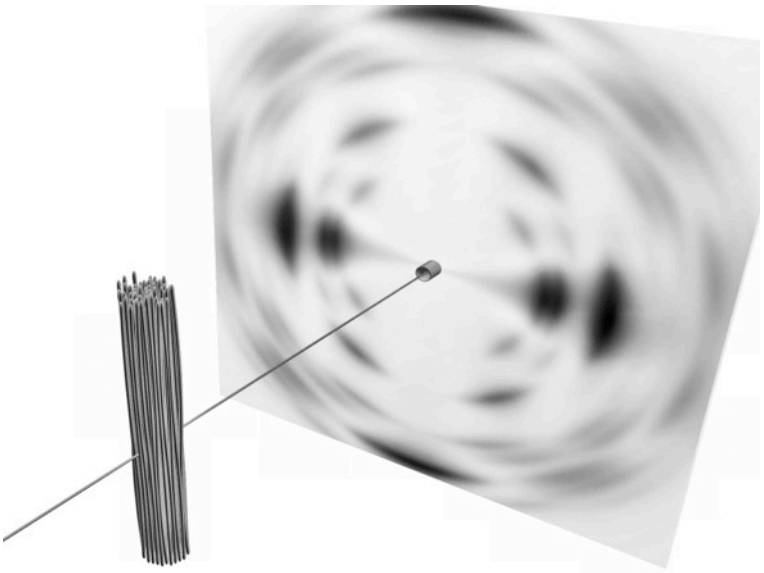

Figure 5.1 Schematic diagram of the diffraction experiment of a sample with "fiber symmetry".

In this chapter, the degree of preferred orientation of cellulose crystals in jute fibers was investigated with the 2D whole pattern simulation method, and all the calculations and simulations in this chapter were performed with *Mathematica*[6].

5.2 Materials and Methods

Vacuum dried raw jute fibers were provided by the Redbud Textile Tech. Inc., Jiangsu, China.

WAXD measurement of jute fibers was carried out at Beamline X27C in the NSLS. A bundle of jute fibers with length of about 10 cm were vertically fixed on the sample holder, and the sample-to-detector distance is 102.9 mm. The X-ray wavelength was set at 0.1371 nm. MAR-CCD detector manufactured by the Fuji Company was used to collect the 2D image, and the image acquisition time was 30 seconds. Aluminum oxide standard was used to do the calibration. Air background scattering was subtracted with absorption effect considered.

5.3 Theoretical Fundamentals of 2D Diffraction Simulation

In real space, the crystalline lattice can be denoted using three vectors ***a***, ***b***, and ***c***, which are conventionally assigned to the three coordinates of the unit cell, and therefore the position of the *j*-th atom, $\boldsymbol{x_j}$, in the lattice can be expressed as:

$$\mathbf{x_j} = p_j\mathbf{a} + q_j\mathbf{b} + r_j\mathbf{c} \qquad \text{Eq. 5.1}$$

where p_j, q_j *and* r_j are the fractional coordinates in ***a***, ***b***, and ***c*** directions. Each lattice plane (*hkl*) in the real place corresponds to a node (*hkl*) in the reciprocal space. The position of the (*hkl*) node, $\boldsymbol{s_{hkl}}$, can be written as:

$$\mathbf{s_{hkl}} = h\mathbf{a}^* + k\mathbf{b}^* + l\mathbf{c}^* \qquad \text{Eq. 5.2}$$

in which ***a****, ***b**** and ***c**** are the vectors in reciprocal space, corresponding to the ***a***, ***b***, and ***c*** directions, respectively. The absolute value of $\boldsymbol{s_{hkl}}$ is $s=2\sin\theta/\lambda$, as described in previous chapters.

The scattering intensity contributed from the diffraction of (*hkl*) planes, I_{hkl}, is proportional to the square of structure factor's modulus F_{hkl}, which is given as:

$$I_{hkl}(s) \propto \left|F_{hkl}(s)\right|^2 \qquad \text{Eq. 5.3}$$

$$F_{hkl} = \sum_{j=1}^{n} f_j \exp(-i2\pi\mathbf{s_{hkl}}\cdot\mathbf{x_j}) = \sum_{j=1}^{n} f_j \exp[-i2\pi(p_j h + q_j k + r_j l)] \qquad \text{Eq. 5.4}$$

where f_j is the atomic form factor, which is dependent on the atomic numbers. The unit cell information of cellulose I_α and I_β is listed in Table 1.1.

The powder-averaged intensity (I_{ave}) is the total intensity diluted over the spherical surface with radius of s_{hkl}, which is expressed as:

$$I_{ave}(s) = \frac{1}{4\pi s_{\mathrm{hkl}}^{\,2}} I_{hkl}(s) \qquad \text{Eq. 5.5}$$

In the 3D reciprocal space, any position can be described in another set of coordinates, namely spherical coordinate system, which is determined by the polar angle (ϕ), azimuthal angle (ψ) and the absolute value of the scattering vector (s), as shown in Figure 5.2.

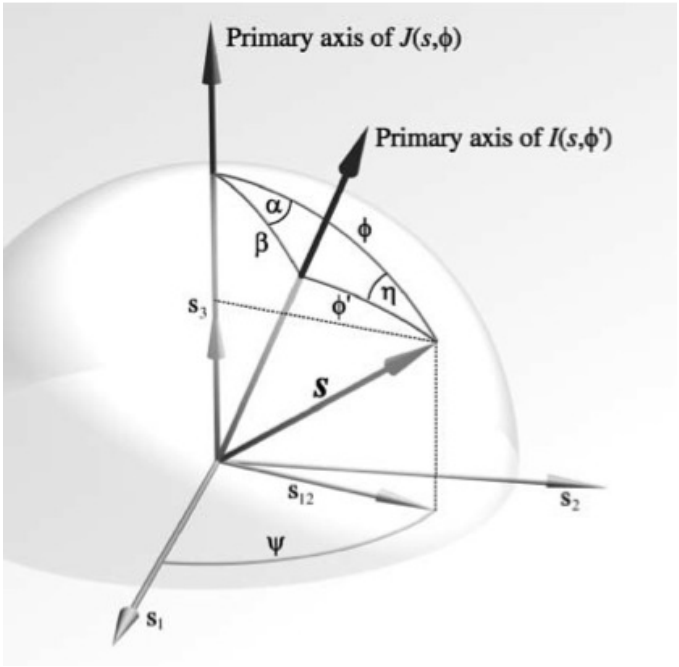

Figure 5.2 Illustration of spherical coordinate system and trigonometric relationship for fiber symmetry[4]

In our simulation, it is assumed that the intensity is only dependent on ϕ and s, which means that the intensity keeps unchanged at any ψ angle as long as the ϕ and s are fixed. Based on this assumption, the simulated intensity I_{sim} of the cellulose fiber system can be written as:

$$I_{sim}(s,\phi) = I_{ave}(s) \cdot F(\phi,\phi_{hkl}) \qquad \text{Eq. 5.6}$$

where ϕ_{hkl} is the polar angle of given (hkl) plane, and the function $F(\phi,\phi_{hkl})$ describes how intensity distributes over polar angle[5] and is given as:

$$F(\phi,\phi_{hkl}) = \frac{1}{\pi}\int_0^{\pi} g(\beta)d\eta \qquad \text{Eq. 5.7}$$

In Equation 5.7, $g(\beta)$ is called orientation distribution function (ODF) describing the distribution of orientation angles β, which is the angle between the fiber axis and individual crystalline units. In this simulation, the Onsager distribution, as shown below, was adopted[4]:

$$g(\beta) = \frac{p\cosh(p\cos\beta)}{\sinh(p)} \qquad \text{Eq. 5.8}$$

in which p is a parameter determining the degree of the orientation angle distribution. As a result, the function $F(\phi, \phi_{hkl})$ can be written as:

$$F(\phi, \phi_{hkl}) = \frac{p}{\sinh(p)}\cosh(p\cos\phi\cos\phi_{hkl})I_0(p\sin\phi\sin\phi_{hkl}) \qquad \text{Eq. 5.9}$$

where I_0 is the modified Bessel function of the first kind of order zero.

5.4 Results and Discussion

In this study, the 2D diffraction pattern of raw jute fibers was simulated using Equation 5.6, assuming that the fiber axis was parallel to the ***c*** axis of the unit cell. The peak width in the radial direction was simulated using a Lorentz distribution, and the amorphous halo on the pattern was fitted with a Gaussian distribution. Both cellulose I_α and I_β were adopted to simulate the pattern with the ratio of I_α over I_β as a parameter of the simulation. The comparison between the simulated 2D pattern and the Fraser corrected experimental pattern is shown in Figure 5.3.

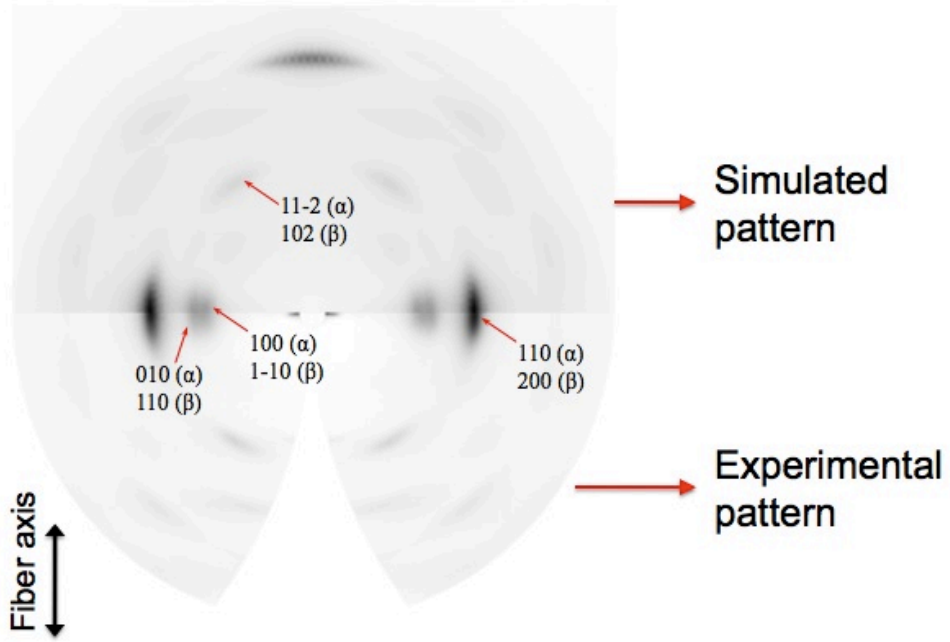

Figure 5.3 2D simulation of jute fiber diffraction pattern (top) and the experimental WAXD pattern (bottom)

In 2D patterns, the peak intensity is demonstrated by the darkness of the gray color, in which case it is not convenient to make intuitive comparison of peak intensities between the experimental and simulated patterns. To solve this problem, the 3D patterns of were plotted with the intensity embodied in height. The comparison of 3D experimental and simulated patterns is shown in Figure 5.4.

In the simulation, the parameter p = 59 and the contents ratio of I_α to I_β was 6:4. Compared to the parameter p, in polymer field, the term Hermans' orientation parameter $\langle P_2 \rangle$ is more often used to describe the degree of preferred orientation. When $\langle P_2 \rangle = 1$, it means all the crystals share the same preferred orientation, which is parallel with the ***c*** direction; when $\langle P_2 \rangle = 0$, the crystals are randomly distributed without any preferred orientation; when $\langle P_2 \rangle = -1/2$, all the crystals share the same preferred orientation, which is perpendicular to the ***c*** direction. The parameter p can be converted into $\langle P_2 \rangle$ by:

$$\langle P_2 \rangle = 1 - \frac{3[\coth(p) - 1/p]}{p} \qquad \text{Eq. 5.10}$$

Therefore for the jute fibers, substituting p = 59 into Equation 5.10, we got the Hermans' orientation parameter $<P_2>$ of the cellulose crystals was 0.95, indicating a well parallel chain-packing system.

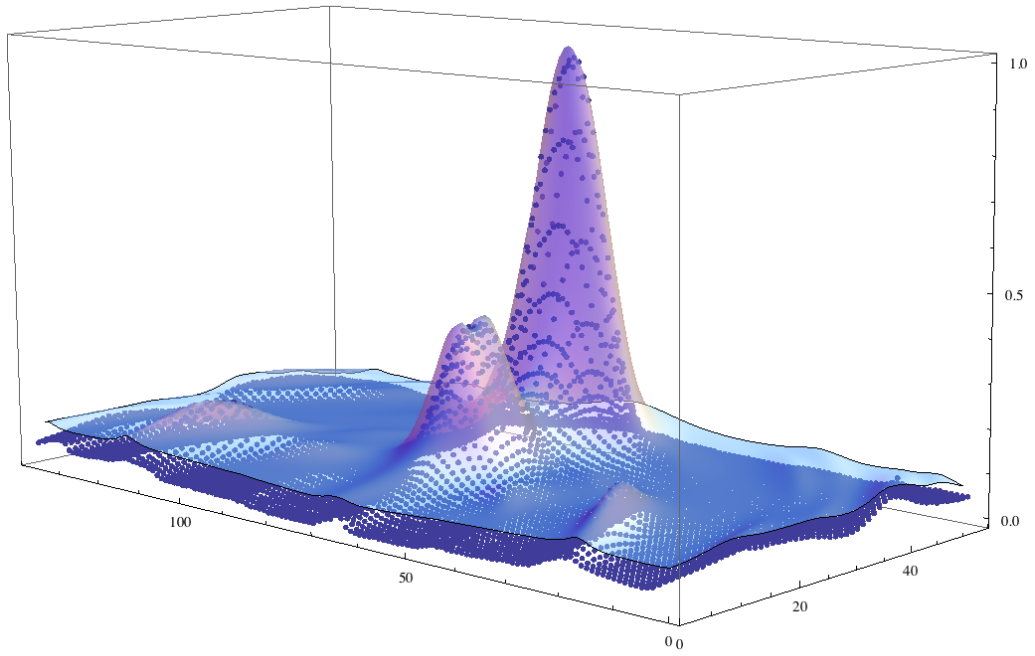

Figure 5.4 3D patterns of experimental data (dots) and simulated profile (continuous layer)

5.5 Conclusions

Cellulose crystals in jute fibers have high degree of preferred orientation. To quantitatively measure the degree of preferred orientation, 2D whole pattern simulation was performed to simulate the experimental diffraction pattern of dried jute fibers. From the simulation, it was determined that the cellulose in jute fibers consisted of both cellulose I_α and I_β phases with contents ratio of 6:4, and the Hermans' orientation parameter $<P_2>$ was calculated to be 0.95, suggesting a nearly uniform orientation of the cellulose crystals.

References

(1) Li, X.; Tabil, L. G.; Panigrahi, S. *J Polym Environ* **2007**, *15*, 25.

(2) Jahan, M. S.; Saeed, A.; He, Z. B.; Ni, Y. H. *Cellulose* **2011**, *18*, 451.

(3) Cao, X. W.; Ding, B.; Yu, J. Y.; Al-Deyab, S. S. *Carbohyd Polym* **2012**, *90*, 1075.

(4) Burger, C.; Hsiao, B. S.; Chu, B. *Polym Rev* **2010**, *50*, 91.

(5) Mao, Y. M.; Burger, C.; Zuo, F.; Hsiao, B. S.; Mehta, A.; Mitchell, C.; Tsou, A. H. *Macromolecules* **2011**, *44*, 558.

(6) Wolfram Research, I. *Mathematica*; Version 8.0 ed.; Wolfram Research, Inc.: Champaign, Illinois, 2010.

Chapter 6 Comparison of SAXS Models Developed in This Work

In this work, three SAXS models, including the polydisperse ribbon model (Chapter 2), the monodisperse nanostrip model (Chapter 3) and the "1D-paracrystalline" model (Chapter 3), were developed to solve different types of fiber-shape structures. The analogies and differences of the models as well as the possible applications will be elaborated in this chapter.

6.1 Assumptions

In all three models, the ribbons or nanostrips were assumed to be infinitely long, as the lengths over couple of hundreds nanometers far exceeded the size range (0.5−100 nm) that SAXS could normally investigate. With this assumption, the fiber lengths would only contribute a factor of 1/s to the intensity distribution function, while the variation of length value would not change the shape of the curve. Therefore for the three models, only the cross-sectional dimensions were used as parameters to simulate the scattering intensity curves.

In addition, for the solution SAXS experiments of TEMPO-oxidized nanofibers/nanostrips, it was assumed that there were large enough amount of negative charges on the surfaces of nanofibers/nanostrips to facilitate their dispersion in aqueous suspension without precipitation. Also the concentration of the suspensions for SAXS tests were relatively low (< 1 wt%), although with the fiber length, the concentration should far exceed the overlap concentration. Nevertheless, for both the ribbon model and the nanostrip model, it was assumed that the inter-fiber interaction was relatively weak so that the structure factor could be considered to be 1, and only the form factor related to the shape and dimensions of individual cross sections of particles was used for the intensity calculation. For the "1D-paracrystalline" model, there existed the scenario that several nanostrips could be stacked up to form a bigger structure. Then,

the inter-fiber interaction could no longer be neglected for the nanostrips inside of the stacks, but it was assumed that the interactions between individual stacks could be ignored.

6.2 Simplifications

While performing model fitting, if there existed numerical integrals in the model, usually the computational efficiency would be low. To obtain the analytical solutions of the integrals, several mathematical simplifications were made during the development of the ribbon model, the nanostrip model and the simplified "1D-paracrystalline" model.

For the polydisperse ribbon model, the first simplification was made with the purpose of extracting the factor of $\left[\frac{\sin(\pi sa)}{\pi sa}\right]^2$ out of the integral by getting rid of $\cos\psi$ in Equation 2.9. The assumption for this simplification was that the thickness *a* of the rectangular cross-section should be much less than the width *b*, beyond which the simplification would be invalid. The second simplification was simply a mathematical substitution of a hypergeomatric function for the integral part in Equation 2.10 without assumption. Therefore, when using this simplified ribbon model, it should be kept in mind that the value of parameter *a* should be strictly less than the value of parameter *b*; otherwise the parameter values would not be meaningful.

In the nanostrip model, for the sake of efficient calculation, it was assumed that the electron density across the thickness of the nanostrips followed a Gaussian distribution, the Fourier transform of which would still be a Gaussian distribution (Equation 3.2). In reality, the electron density distribution across the thickness of a single layer of cellulose molecules might not be exactly a Gaussian distribution. However, considering that the adoption of other distribution functions would cause complicated Fourier transform with daunting calculation

complexity, the assumption of a Gaussian distribution would be a very efficient way to solve the problem without deviating too much from reality.

From the "1D-paracrystalline" model introduced in Chapter 3 to the simplified "1D-paracrystalline" model described in Chapter 4, in order to get an analytical solution, the structure factor $S(s)$ (Equation 4.1) was separated into two parts (i.e. $S_1(s)$ and $S_2(s)$), simulating the front part (low-s region) and the tail part (high-s region) of the experimental curve, respectively. The $S_1(s)$ part was a Lorentzian function, which led to an analytical solution to the integral in Equation 4.5; for the $S_2(s)$ part in the high-s region, it was assumed that the azimuthal angle Ψ was small, and the simplification of $\cos\Psi \approx 1$ and $\sin\Psi \approx$ t was made in Equation 4.6. With the analytical solution, the calculation efficiency of the simplified "1D-paracrystalline" model was significantly higher than that of the original "1D-paracrystalline" model. However, it should be noted that with large n value (n was the number of layers in each stack), the two curves almost overlapped with each other, but the discrepancy of the initial part of the two curves would become more obvious with the n value getting smaller, in which case the simplified model should be used with caution.

6.3 Applications

With the adoption of analytical expressions instead of numerical integrals, the simplified models (i.e. the ribbon model, the nanostrip model and the simplified "1D-paracrystalline" model) showed highly enhanced computing efficiency. With the understanding of assumptions and limitations, those models can be very helpful for the SAXS analysis of similar systems.

The ribbon model can be used for the cylinder system with high aspect ratio and near rectangular cross-sections, with thickness being smaller than the width. It could be used either for the monodisperse system with Equation 2.11 or the polydisperse system of Gamma

distribution with Equation 2.25. The nanostrip model is applicable to the ribbon system with high aspect ratio and very thin thicknesses (< 1 nm), and it can also be used as the form factor of the building unit in a more complicated model (e.g. stacking model). The original/simplified "1D-paracrystalline" model can be used to simulate the stacking structures with finite stack height, and the building block of the stack should be nanostrip-like ribbons with large aspect ratio and sub-nanometer thickness.

Chapter 7 Conclusions and Future Work

7.1 Conclusions

Cellulose is one of the most abundant biopolymers on earth. The wide applications of cellulose nanofibers/microfibrils extracted from biomass have attracted growing attention from both academic and industrial fields. Despite the fact that the chemical constitution of cellulose was revealed more than one hundred years ago, the morphology and physical structures of cellulose microfibrils (nascent crystals), nanofibers, etc. are only beginning to be understood. With the assistance of X-ray scattering techniques and other characterization methods, the morphology and structures of cellulose nanofibers/microfibrils were investigated in this work.

In Chapter 2, the solution small-angle X-ray scattering (SAXS) method was used to investigate the size and size distribution of cellulose nanofibers isolated from dried pulps. By performing model fittings to the experimental data using mainly a simplified ribbon model, it was found that the nanofibers prepared from the maritime pine wood pulp (Biofloc-96) possessed a ribbon shape with the size-weighted average thickness and width of 3.2 nm and 12.7 nm, respectively, and the width information was supported by the width values measured from TEM images.

By investigating the effects of NaClO/cellulose ratio, reaction time and homogenization time on the morphology and DO of cellulose nanofibers, it was found that higher NaClO/cellulose ratio or longer reaction time tended to reduce the average widths of nanofibers but expand the size distribution of the thicknesses. The longer homogenization time attributed to smaller and more uniform sizes of nanofibers. The DO could reach a maximum of 16.3% at a NaClO/cellulose ratio of 5 mmol/g. During the oxidation process, the DO could reach its maximum value within 1 hour, after which the DO of nanofibers fluctuated within a small range.

This phenomenon might be caused by the exfoliation of the oxidized outermost layer molecules on the side surfaces of nanofibers during oxidation.

In Chapter 3, cellulose nanostrips with width of ~4 nm and thickness of ~0.5 nm were extracted from the raw spruce wood powder. The SAXS simulation confirmed that cellulose microfibril fractions after the TEMPO-mediated oxidation and successive mechanical homogenization formed nanostrips in an aqueous suspension (0.077 wt%), while the nanostrips turned to stack up to form a multi-layer structure at higher concentration (0.15 wt%). The TEM images verified the widths and the AFM measurements confirmed the thicknesses information of nanostrips. The WAXD analysis suggested that the delamination of microfibrils occurred along the $(1\,\bar{1}0)$ plane during the mechanical homogenization, which was consistent with the hypothesis of cellulose biosynthesis in plant cell walls. The high DO of cellulose nanostrips implied that not only the surface molecules but also a part of the molecules in the inner chains was also oxidized. The solid-state ^{13}C NMR analysis indicated that possible oxidation of the inner chains occurred in the harsh oxidation process, with the delamination of microfibrils being mainly occurred in the homogenization process.

In Chapter 4, the stacking of cellulose nanofibers caused by the adsorption of silver ions on the surfaces was investigated by solution SAXS. Through model fitting with a "1D-paracrystalline" model, it was determined that the number of silver-ion layers in the stacks followed an exponential distribution with an average value of 7. The average inter-layer distances was 2.3 nm, which was smaller than the average thickness of cellulose nanofibers, implying that thinner nanofibers tended to stack up more easily than thick nanofibers. The width of silver-ion planes determined from the model fitting was 4.1 nm, much smaller than the

average width of nanofibers (8.7 nm), which might be caused by the non-uniform distribution of silver ions on the surfaces of nanofibers.

In Chapter 5, the degree of preferred orientation of cellulose crystals in jute fibers was analyzed by 2D X-ray diffraction. From the whole pattern simulation, it was determined that the cellulose in jute fibers consisted of both cellulose I_α and I_β phases with contents ratio of 6:4, and the Hermans' orientation parameter $\langle P_2 \rangle$ was calculated to be 0.95, suggesting a nearly uniform orientation of the cellulose crystals.

In Chapter 6, the assumptions, simplifications and applications of the three SAXS models (i.e. ribbon model, nanostrip model and "1D-paracrystalline" model) developed in this work were elaborated, and the matters needing attention during the application of the models were also discussed.

7.2 Future Work

As illustrated in Chapter 3, the TEMPO-oxidized cellulose nanostrips prepared through the delamination of cellulose microfibrils are monolayers of gulan chains, and the degree of oxidation (DO) can reach 50%. The large specific surface area and the high density of carboxylate groups grant this material great potential in both direct application in efficient viruses or heavy metal adsorption and further surface modification, such as chemical grafting of other radicals onto the nanostrip surfaces.

However, currently the main problem that might hinder the application of this material is the aggregation of nanostrips at 'high' concentration. As we previously hypothesized, when the TEMPO-mediated oxidation was performed during the preparation of the nanostrips, the oxidants could penetrate into the microfibrils through the cracks created by the dissolution of

hemicellulose between glucan chain layers, however, the depth of the penetration was small, and therefore only the chains at the two ends of each layer were oxidized, while the middle chains of the layer were not oxidized. Then the attractive hydrogen bonding between the un-oxidized chains could cause aggregation of the nanostrips. As described in Chapter 3, when the nanostrip suspension was concentrated from 0.077 wt% to 0.15 wt% by water evaporation, the nanostrips aggregated to form stacking structures, which reduced the specific surface areas of the nanofibril system. In this case, it is important to develop a method that prevents the aggregation of nanostrips in the aqueous suspension.

One possible way to prevent the aggregation of nanostrips is to re-perform the TEMPO-mediated oxidation to the nanostirp system, which would further increase the amount of negatively charged carboxylate groups and facilitate the dispersion of nanostrips in aqueous suspension. However, this re-oxidation should be mild, because the nanostrips are single layers of cellulose molecular chains associated by van der Waals forces, and a harsh oxidation condition might break the nanostrips up into individual molecular chains. Therefore, the experimental parameters of the oxidation, including the ratio between cellulose and NaClO, the reaction time and the stirring rate, should be investigated to optimize the re-oxidation process. Hopefully after the re-oxidation and purification by dialysis, the morphology of the nanostrips is retained while the DO is highly increased, and the repulsive electrostatic forces would prevent the aggregation of nanostrips even at high concentration.

List of References

Agarwal, A.; Weis, T. L.; Schurr, M. J.; Faith, N. G.; Czuprynski, C. J.; McAnulty, J. F.; Murphy, C. J.; Abbott, N. L. *Biomaterials* **2010**, *31*, 680.

Akaike, H. *Ieee T Automat Contr* **1974**, *Ac19*, 716.

Allaire, M.; Yang, L. *J Synchrotron Radiat* **2011**, *18*, 41.

Araki, J.; Wada, M.; Kuga, S. *Langmuir* **2001**, *17*, 21.

Azeredo, H. M. C.; Mattoso, L. H. C.; Avena-Bustillos, R. J.; Ceotto, G.; Munford, M. L.; Wood, D.; McHugh, T. H. *J Food Sci* **2010**, *75*, N1.

Banerjee, I.; Pangule, R. C.; Kane, R. S. *Adv Mater* **2011**, *23*, 690.

Barud, H. S.; Regiani, T.; Marques, R. F. C.; Lustri, W. R.; Messaddeq, Y.; Ribeiro, S. J. L. *J Nanomater* **2011**, *2011*, 1.

Beck-Candanedo, S.; Roman, M.; Gray, D. G. *Biomacromolecules* **2005**, *6*, 1048.

Biermann, C. J. *Essentials of pulping and papermaking*; Academic Press, **1993**.

Bondeson, D.; Mathew, A.; Oksman, K. *Cellulose* **2006**, *13*, 171.

Braun, B.; Dorgan, J. R.; Chandler, J. P. *Biomacromolecules* **2008**, *9*, 1255.

Bucko, T.; Tunega, D.; Angyan, J. G.; Hafner, J. *J Phys Chem A* **2011**, *115*, 10097.

Burger, C.; Hsiao, B. S.; Chu, B. *Polym Rev* **2010**, *50*, 91.

Campbell, N. A. *Biology*; 4th ed.; Benjamin Cummings: NY, **1996**.

Cao, X. W.; Ding, B.; Yu, J. Y.; Al-Deyab, S. S. *Carbohyd Polym* **2012**, *90*, 1075.

Chabannes, M.; Ruel, K.; Yoshinaga, A.; Chabbert, B.; Jauneau, A.; Joseleau, J. P.; Boudet, A. M. *Plant J* **2001**, *28*, 271.

Colvin, J. R. *J Cell Biol* **1963**, *17*, 105.

Cosgrove, D. J. Nature reviews. Molecular cell biology 2005, 6, 850.

Cousins, S. K.; Brown, R. M. *Polymer* **1995**, *36*, 3885.

Damm, C.; Munstedt, H. *Appl Phys A-Mater* **2008**, *91*, 479.

Dastjerdi, R.; Montazer, M.; Shahsavan, S. *Colloid Surface A* **2009**, *345*, 202.

Delmer, D. P. *Annu Rev Plant Phys* **1999**, *50*, 245.

Dong, X. M.; Revol, J. F.; Gray, D. G. *Cellulose* **1998**, *5*, 19.

El-Rafie, M. H.; Mohamed, A. A.; Shaheen, T. I.; Hebeish, A. *Carbohyd Polym* **2010**, *80*, 779.

Entcheva, E.; Bien, H.; Yin, L. H.; Chung, C. Y.; Farrell, M.; Kostov, Y. *Biomaterials* **2004**, *25*, 5753.

Fernandes, A. N.; Thomas, L. H.; Altaner, C. M.; Callow, P.; Forsyth, V. T.; Apperley, D. C.; Kennedy, C. J.; Jarvis, M. C. *P Natl Acad Sci USA* **2011**, *108*, E1195.

Fink, H. P.; Hofmann, D.; Philipp, B. *Cellulose* **1995**, *2*, 51.

Fukuzumi, H.; Saito, T.; Wata, T.; Kumamoto, Y.; Isogai, A. *Biomacromolecules* **2009**, *10*, 162.

Gibbons, J. H. *Technologies for reducing dioxin in the manufacture of bleached wood pulp*; DIANE Publishing: Washington, DC, **1989**.

Grunert, M.; Winter, W. T. *J Polym Environ* **2002**, *10*, 27.

Guinier, A.; Fournet, D. *Small-angle Scattering of X-rays*; Jone Wiley & Sons, Inc.: New York, NY, **1955**.

Ha, M. A.; Apperley, D. C.; Jarvis, M. C. *Plant Physiol* **1997**, *115*, 593.

Habibi, Y.; Chanzy, H.; Vignon, M. R. *Cellulose* **2006**, *13*, 679.

Habibi, Y.; Goffin, A. L.; Schiltz, N.; Duquesne, E.; Dubois, P.; Dufresne, A. *J Mater Chem* **2008**, *18*, 5002.

Habibi, Y.; Lucia, L. A.; Rojas, O. *J. Chem Rev* **2010**, *110*, 3479.

Habibi, Y.; Mahrouz, M.; Vignon, M. R. *Food Chem* **2009**, *115*, 423.

Hayashi, T. *Annu Rev Plant Phys* **1989**, *40*, 139.

He, J. H.; Kunitake, T.; Nakao, A. *Chem Mater* **2003**, *15*, 4401.

Helbert, W.; Nishiyama, Y.; Okano, T.; Sugiyama, J. *J Struct Biol* **1998**, *124*, 42.

Horikawa, Y.; Itoh, T.; Sugiyama, J. *Cellulose* **2006**, *13*, 309.

Hult, E. L.; Larsson, P. T.; Iversen, T. *Cellulose* **2000**, *7*, 35.

Ioelovich, M.; Leykin, A. *Bioresources* **2008**, *3*, 170.

Isogai, A.; Saito, T.; Fukuzumi, H. *Nanoscale* **2011**, *3*, 71.

Iwamoto, S.; Nakagaito, A. N.; Yano, H. *Appl Phys A-Mater* **2007**, *89*, 461.

Jahan, M. S.; Saeed, A.; He, Z. B.; Ni, Y. H. *Cellulose* **2011**, *18*, 451.

Jakob, H. F.; Fratzl, P.; Tschegg, S. E. *J Struct Biol* **1994**, *113*, 13.

Kapoor, K.; Lahiri, D.; Rao, S. V. R.; Sanyal, T.; Kashyap, B. P. B *Mater Sci* **2004**, *27*, 59.

Kato, Y.; Matsuo, R.; Isogai, A. *Carbohyd Polym* **2003**, *51*, 69.

Khan, R. A.; Salmieri, S.; Dussault, D.; Uribe-Calderon, J.; Kamal, M. R.; Safrany, A.; Lacroix, M. *J Agr Food Chem* **2010**, *58*, 7878.

Klein, R. In *Neutrons, X-Rays and Light*; Zemb, T., Lindner, P., Eds.; Elsevier Science: Amsterdam, **2002**.

Klemm, D.; Heublein, B.; Fink, H. P.; Bohn, A. *Angew Chem Int Edit* **2005**, *44*, 3358.

Kuga, S.; Brown, R. M. *Polym Commun* **1987**, *28*, 311.

Kumar, R.; Hu, F.; Hubbell, C. A.; Ragauskas, A. J.; Wyman, C. E. *Bioresource Technol* **2013**, *130*, 372.

Leitner, J.; Hinterstoisser, B.; Wastyn, M.; Keckes, J.; Gindl, W. *Cellulose* **2007**, *14*, 419.

Leppanen, K.; Andersson, S.; Torkkeli, M.; Knaapila, M.; Kotelnikova, N.; Serimaa, R. *Cellulose* **2009**, *16*, 999.

Li, Q. L.; Mahendra, S.; Lyon, D. Y.; Brunet, L.; Liga, M. V.; Li, D.; Alvarez, P. J. *J. Water Res* **2008**, *42*, 4591.

Li, Q. Q.; Renneckar, S. *Biomacromolecules* **2011**, *12*, 650.

Li, X.; Tabil, L. G.; Panigrahi, S. *J Polym Environ* **2007**, *15*, 25.

Ma, H. Y.; Burger, C.; Hsiao, B. S.; Chu, B. *Biomacromolecules* **2011**, *12*, 970.

Maciel, G. E.; Odonnell, D. J.; Ackerman, J. J. H.; Hawkins, B. H.; Bartuska, V. J. *Makromol Chem* **1981**, *182*, 2297.

Malainine, M. E.; Mahrouz, M.; Dufresne, A. *Compos Sci Technol* **2005**, *65*, 1520.

Mao, Y. M.; Burger, C.; Zuo, F.; Hsiao, B. S.; Mehta, A.; Mitchell, C.; Tsou, A. H. *Macromolecules* **2011**, *44*, 558.

Montanari, S.; Rountani, M.; Heux, L.; Vignon, M. R. *Macromolecules* **2005**, *38*, 1665.

Moon, R. J.; Martini, A.; Nairn, J.; Simonsen, J.; Youngblood, *J. Chem Soc Rev* **2011**, *40*, 3941.

Mwaikambo, L. Y. *Bioresources* **2009**, *4*, 566.

Nishiyama, Y. *J Wood Sci* **2009**, *55*, 241.

Nishiyama, Y.; Johnson, G. P.; French, A. D.; Forsyth, V. T.; Langan, P. *Biomacromolecules* **2008**, *9*, 3133.

Nishiyama, Y.; Langan, P.; Chanzy, H. *J Am Chem Soc* **2002**, *124*, 9074.

Nishiyama, Y.; Sugiyama, J.; Chanzy, H.; Langan, P. *J Am Chem Soc* **2003**, *125*, 14300.

Okita, Y.; Saito, T.; Isogai, A. *Holzforschung* **2009**, *63*, 529.

Okita, Y.; Saito, T.; Isogai, A. *Biomacromolecules* **2010**, *11*, 1696.

OSullivan, A. C. *Cellulose* **1997**, *4*, 173.

Paakko, M.; Ankerfors, M.; Kosonen, H.; Nykanen, A.; Ahola, S.; Osterberg, M.; Ruokolainen, J.; Laine, J.; Larsson, P. T.; Ikkala, O.; Lindstrom, T. *Biomacromolecules* **2007**, *8*, 1934.

Pandey, J. K.; Lee, J. W.; Chu, W. S.; Kim, C. S.; Ahn, S. H. *Macromol Res* **2008**, *16*, 396.

Pedersen, J. S. *Adv Colloid Interfac* **1997**, *70*, 171.

Pedersen, J. S. In *Neutrons, X-Rays and Light*; Zemb, T., Lindner, P., Eds.; Elsevier Science: Amsterdam, **2002**.

Pokhrel, D.; Viraraghavan, T. *Sci Total Environ* **2004**, *333*, 37.

Porod, G. In *Small Angel X-ray Scattering*; Glatter, O., Kratky, O., Eds.; Academic Press Inc.: London, UK, **1982**, p 32.

Saito, T.; Hirota, M.; Tamura, N.; Kimura, S.; Fukuzumi, H.; Heux, L.; Isogai, A. *Biomacromolecules* **2009**, *10*, 1992.

Saito, T.; Isogai, A. *Carbohyd Polym* **2005**, *61*, 183.

Saito, T.; Kimura, S.; Nishiyama, Y.; Isogai, A. *Biomacromolecules* **2007**, *8*, 2485.

Saito, T.; Kuramae, R.; Wohlert, J.; Berglund, L. A.; Isogai, A. *Biomacromolecules* **2013**, *14*, 248.

Saito, T.; Nishiyama, Y.; Putaux, J. L.; Vignon, M.; Isogai, A. *Biomacromolecules* **2006**, *7*, 1687.

Saito, T.; Shibata, I.; Isogai, A.; Suguri, N.; Sumikawa, N. *Carbohyd Polym* **2005**, *61*, 414.

Sambhy, V.; MacBride, M. M.; Peterson, B. R.; Sen, A. *J Am Chem Soc* **2006**, *128*, 9798.

Samir, M. A. S. A.; Alloin, F.; Dufresne, A. *Biomacromolecules* **2005**, *6*, 612.

Sarkar, A.; Mukherjee, P.; Barat, P. *Z Kristallogr* **2007**, 543.

Sawyer, L. C.; Grubb, D. T.; Meyers, G. F. *Polymer Microscopy*; 3rd ed.; Springer Science+Business Media, LLC.: New York, NY, **2008**.

Saxena, I. M.; Brown, R. M. *Ann Bot-London* **2005**, *96*, 9.

Scardi, P.; Leoni, M.; Delhez, R. *J Appl Crystallogr* **2004**, *37*, 381.

Sevillano, G.; Rodriguezpuyol, M.; Martos, R.; Duque, I.; Lamas, S.; Diezmarques, M. L.; Lucio, J.; Rodriguezpuyol, D. Nephrol *Dial Transpl* **1990**, *5*, 497.

Siro, I.; Plackett, D. *Cellulose* **2010**, *17*, 459.

Sjostrom, E. *Wood Chemistry, Fundamentals and Applications*; 2nd ed.; Academic Press: San Diego, **1993**.

Su, Y.; Burger, C.; Hsiao, B. S.; Chu, B. *J Appl Crystallogr* **2014**, *47*, 788.

Sugiyama, J.; Chanzy, H.; Revol, J. F. *Planta* **1994**, *193*, 260.

Sugiyama, J.; Harada, H.; Fujiyoshi, Y.; Uyeda, N. *Planta* **1985**, *166*, 161.

Sugiyama, J.; Vuong, R.; Chanzy, H. *Macromolecules* **1991**, *24*, 4168.

Suzuki, H.; Kamiyama, T. *J Wood Sci* **2004**, *50*, 351.

Svergun, D. I.; Koch, M. H. J. *Rep Prog Phys* **2003**, *66*, 1735.

Taniguchi, T.; Okamura, K. *Polym Int* **1998**, *47*, 291.

Terech, P.; Chazeau, L.; Cavaille, J. Y. *Macromolecules* **1999**, *32*, 1872.

van den Berg, O.; Capadona, J. R.; Weder, C. *Biomacromolecules* **2007**, *8*, 1353.

Vietor, R. J.; Newman, R. H.; Ha, M. A.; Apperley, D. C.; Jarvis, M. C. *Plant J* **2002**, *30*, 721.

Wang, B.; Sain, M. *Compos Sci Technol* **2007**, *67*, 2521.

Whitney, S. E. C.; Brigham, J. E.; Darke, A. H.; Reid, J. S. G.; Gidley, M. J. *Plant J* **1995**, *8*, 491.

Wickholm, K.; Larsson, P. T.; Iversen, T. *Carbohyd Res* **1998**, *312*, 123.

Wolfram Research, I. *Mathematica*; Version 8.0 ed.; Wolfram Research, Inc.: Champaign, Illinois, **2010**.

Yang, Q. L.; Wu, C. N.; Saito, T.; Isogai, A. *Carbohyd Polym* **2014**, *100*, 179.

Zhang, T. J.; Wang, W.; Zhang, D. Y.; Zhang, X. X.; Ma, Y. R.; Zhou, Y. L.; Qi, L. M. *Adv Funct Mater* **2010**, *20*, 1152.

Zugenmaier, *P. Prog Polym Sci* **2001**, *26*, 1341.

Zuo, X.; Grishaev, A. *Solution Small Angle X-ray Scattering: Basic Principles and Experimental Aspects*, **2009**.